REPORT DOCUMENTATION PAGE

AFRL-SR-AR-TR-04-
0145

1. AGENCY USE ONLY *(Leave blank)*	**2. REPORT DATE** March 1, 2004	**3. REPORT TYPE AND DATES COVERED** Final Technical Report (1Nov 97 - 31 Oct 00)

4. TITLE AND SUBTITLE
Transport in Plasma Thrusters Using Complex Propellants

5. FUNDING NUMBERS
F49620-98-1-0085
2308/AX
61102F

6. AUTHOR(S)
Peter J. Turchi

7. PERFORMING ORGANIZATION NAME(S) AND ADDRESS(ES)
The Ohio State University
Aerospace Engineering and Aviation Dept
Columbus, OH 43210

8. PERFORMING ORGANIZATION REPORT NUMBER

9. SPONSORING/MONITORING AGENCY NAME(S) AND ADDRESS(ES)
AFOSR/NA
4015 Wilson Blvd., Room 713
Arlington, VA 22230-1954
Program Manager: Dr. Mitat Birkan

10. SPONSORING/MONITORING AGENCY REPORT NUMBER

11. SUPPLEMENTARY NOTES

12a. DISTRIBUTION AVAILABILITY STATEMENT
APPROVED FOR PUBLIC RELEASE, DISTRIBUTION IS UNLIMITED

12b. DISTRIBUTION CODE

13. ABSTRACT *(Maximum 200 words)*

Theoretical modeling of ablation-fed, pulsed plasma thrusters (PPTs) with the MACH2 code has shown that after repeated pulsed operation, the total expelled mass is due to ablation during the discharge and solid decomposition that persists long after the pulse. The latter mass does not considerably contribute to the impulse-bit thus degrading thruster performance. For the rectangular PPT geometry, optimizing current waveforms in combination with channel widths are presented, that utilize all decomposed mass, electromagnetically. These waveforms are characterized by short rise times (< 1 microsec) and prolonged decays (> 25 microsec). Simplified modeling based on steady-state, one-dimensional flow reveals that the mass flow rate varies linearly with the square of the magnetic field and that the downstream flow speed is driven towards the Alfven wave speed when the magnetic pressure is much greater than the gasdynamic pressure. The model has been confirmed by MACH2. The mass flow requirement for such magnetosonic flow in turn, determines the surface temperature of the solid.

20040311 065

14. SUBJECT TERMS

15. NUMBER OF PAGES	80
16. PRICE CODE	

17. SECURITY CLASSIFICATION OF REPORT	**18. SECURITY CLASSIFICATION OF THIS PAGE**	**19. SECURITY CLASSIFICATION OF ABSTRACT**	**20. LIMITATION OF ABSTRACT**
U	U	U	

BEST AVAILABLE COPY

RECEIVED MAR 04 2004

TRANSPORT IN PLASMA THRUSTERS USING COMPLEX PROPELLANTS

FINAL REPORT
(Possible second - independenrt - report submission)

under
Air Force Office of Scientific Research
Grant No. F49620-98-1-0085
OSU RF #735087

***

Start Date: November 1, 1997
End Date: October 31, 2000

Report prepareded by:
Thomas M.York
Professor of Aeronautical and Astronautical Engineering

for
Peter J. Turchi, (PI)
Professor (resigned position 10/31/99)

March 1, 2004
Aerospace Engineering and Aviation Department
The Ohio State University
Columbus, Ohio 43210

SUMMARY OF ACTIVITIES

This report is a reconstruction of a Final Report for the work carried out under this Grant. While the Grant period ran until 10/31/2000, all funds were expended by 10/31/1999, during which period Peter Turchi was the PI and he was a Professor of Aeronautical and Astronautical Engineering at The Ohio State University.

As appointed (Administrative) PI after this period, Prof. York had contacted Dr. Turchi regarding the preparation of a Final Report. Dr. Turchi directed that a Final Report be prepared by Dr. Pavlos Mikellides, a Senior Reserach Engineer on the project, but who also had resigned his position at Ohio State. All relevant contract documents were forwarded (on 10/6/2000, FAX cover sheet follows) to Dr. Mikellides, and he verbally agreed to submit a Final Report. If a Final Report was prepared by Dr. Mikellides, there was no copy forwarded to Prof. York or the Research-Foundation at Ohio State, so the report which follows here will be different should a copy of any earlier report surface.

ABSTRACT

Theoretical modeling of ablation-fed, pulsed plasma thrusters (PPTs) with the MACH2 code has shown that after repeated pulsed operation, the total expelled mass is due to ablation during the discharge and solid decomposition that persists long after the pulse. The latter mass does not considerably contribute to the impulse-bit thus degrading thruster performance. For the rectangular PPT geometry, optimizing current waveforms in combination with channel widths are presented, that utilize all decomposed mass, electromagnetically. These waveforms are characterized by short rise times (<1 μsec) and prolonged decays (>25 μsec). Simplified modeling based on steady-state, one-dimensional flow reveals that the mass flow rate varies linearly with the square of the magnetic field and that the downstream flow speed is driven towards the Alfven wave speed when the magnetic pressure is much greater than the gasdynamic pressure. The model has been confirmed by MACH2. The mass flow requirement for such magnetosonic flow in turn, determines the surface temperature of the solid.

Numerical simulations of coaxial geometries show that, compared with the rectangular, annular and linear pinch configurations, only an arrangement which operates an inverse-pinch discharge offers the convenience of axisymmetry for better correlation between theory and experiment, and operation at relatively high magnetic fields with

DOCUMENTATION OF RESEARCH RESULTS

On the following pages, the cover page and Abstract of a Ph. D. thesis that was completed under the support of this Grant are presented.

Yiangos Mikellides	Ph. D. Thesis	1999
Hani Kamhawi,	Ph. D. Thesis (Dec.)	2002
Christopher Schmahl	Ph. D. Thesis	2000

Following the thesis material, a series of research papers presented at technical conferences are presented. These comprise the bulk of the product of this research They are as follows:

AIAA -98-3662	Schmahl, I. Mikellides, Turchi, P. Mikellides
AIAA -98-3804	Kamhawi, Turchi
AIAA -98-3807	Turchi, I. Mikellides, P. Mikellides, Schmahl
IEPC - 99-211	I. Mikellides, Turchi
IEPC - 99-205	Umeki, Tuechi
AIAA -99-2301	Turchi, I. Mikellides, P. Mikellides, Kamhawi

PERSONNEL EXPENDITURES-
(Without Fringe and Overhead)

Staff and Student Support

Individual	**Position**	**Expend.(approx.)**	**Degree**
P. Turchi	PI	$12 K	
P. Mikellides	Sr. Res. Engr.	$ 8 K	
I. Mikellides	GRA	$ 18 K.	PhD
H. Kamhawi	GRA	$ 15.5 K	PhD
C. Schmahl	GRA	$ 23.2 K	PhD

With added Overhead and Fringe (Non students) , Total for salaries was: $118K

THEORETICAL MODELING AND OPTIMIZATION OF ABLATION-FED PULSED PLASMA THRUSTERS

DISSERTATION

Presented in Partial Fulfillment of the Requirements for the Degree Doctor of Philosophy
in the Graduate School of The Ohio State University

by

Yiangos George Mikellides, B.S.A.A.E, M.S.A.A.E.

*****

The Ohio State University

1999

Dissertation Committee:

Prof. Peter J. Turchi, Adviser

Prof. Thomas M. York

Prof. Michael G. Dunn

Approved by

Adviser
Graduate Program of
Aerospace Engineering

propellant temperatures below the decomposition limit. Design guidelines for an inverse pinch thruster are provided. The inverse-pinch discharge produced by a non-reversing, waveform that rises to 18 kAmps in 0.625 μsec and decays in 6 μsec, in a 1cm-(propellant) radius thruster, is found to prevent solid decomposition while still providing ablated mass for accelaration. At these lower magnetic field levels (~0.4 T, maximum) it is found that thermal effects are driving the surface temperature of the solid, during the latter times of current decay.

EXPERIMENTAL AND THEORETICAL INVESTIGATION OF PULSED PLASMA THRUSTERS

DISSERTATION

Presented in Partial Fullfillment of the Requirements for
the Degree Doctor of Philosophy in the Graduate
School of The Ohio State University

By

Hani Kamhawi, M.S.

******

The Ohio State University
2002

Dissertation Committee:

Professor Thomas M. York, Adviser

Professor Peter J. Turchi

Professor Michael Dunn

Approved by

____

Adviser

Aeronautical and Astronautical
Engineering Graduate Program

ABSTRACT

An extensive experimental and theoretical effort was carried out to investigate and explore various design modifications to improve pulsed plasma thruster (PPT) performance in the energy range between 5 J and 60 J. Experimentally, a benchmark PPT was fabricated utilizing off-the-shelf components, and its performance evaluated and found to be comparable to previous flight type PPTs. A thermal management study to determine and elucidate energy loss mechanisms occurring in PPTs was conducted. It was determined that Teflon surface temperatures in excess of 370 °K were attained during steady state thruster operation after the current pulse has ended contributing to the "late time ablation" of Teflon molecules.

An inductively-driven plasma-actuated PPT was designed, and fabricated, to evaluate and investigate the effect of changing the discharge current waveform on PPT performance since the inductively-driven PPT results in better matching of the circuit parameters and provides extended electromagnetic acceleration times. A 1 μH inductor was used but resulted in reduced discharge current peaks and reduced Teflon ablation; this resulted in low thrust efficiency. In addition, the

crowbar electrode placement contributed to the thrust degradation of the thruster since it resulted in a lateral JXB force that was not directed along the thrust axis.

Coaxial inverse-pinch PPT configurations were designed, fabricated, and tested in an attempt to achieve efficient mass utilization. Axisymmetric discharge current operation for a coaxial inverse-pinch PPT was successfully achieved. Experimental and MACH2 predicted enclosed current contours agreed well for 20 J and 30 J thruster operation. Comparisons between the experimentally and theoretically determined ablation rates indicated good agreement for the 20 J but not for the 30 J thruster operation. For 20 J thruster operation, the temperature of the Teflon propellant surface never exceeded 673 °K, thus indicating that no late time ablation was occurring in the solid. For the 30 J thruster operation the theoretically calculated ablation rate magnitude was only 40% of the experimentally measured value. Investigation of the temperature profile in the Teflon solid at peak surface temperature indicated that the temperature in the Teflon solid exceeded 673 °K; this resulted in additional mass ablation after the current pulse has ended. Analysis of the temperature profile found that to account for the difference between the experimental and theoretical ablation rates, Teflon decomposition occurs for Teflon temperatures approximately above 705 °K. Coaxial inverse-pinch PPT efficiency of 6% was achieved at a specific impulse of 2240 s for 20 J thruster operation. Comparisons between the experimentally measured and MACH2 predicted T_e and n_e temporal profiles in the thruster plume for 20 J thruster operation showed good quantitative and qualitative agreement. Analysis of the energy deposition in the coaxial inverse-pinch PPT using the MACH2 code found that frozen flow losses account for the majority of the initial thruster energy.

THERMOCHEMICAL AND TRANSPORT PROCESSES IN PULSED PLASMA MICROTHRUSTERS: A TWO-TEMPERATURE ANALYSIS

DISSERTATION

Presented in Partial Fulfillment of the Requirements for
the Degree Doctor of Philosophy in the Graduate
School of The Ohio State University

By

Christopher S. Schmahl, M.S.

* * * * *

The Ohio State University
2002

Dissertation Committee:

Professor Michael Dunn, Adviser

Professor Peter Turchi

Professor Jim Scott

Approved by

Michael G. Dunn

Adviser

Department of Aeronautical and
Astronautical Engineering

ABSTRACT

The pulsed plasma thruster (PPT) is a device which has been in use for decades as a spacecraft propulsion system. Traditionally the fuel used is a polymer such as polytetrafluoroethylene (PTFE) also known as Teflon, or polyvinyl chloride (PVC). Teflon is used as fuel for the majority of cases and it is the material studied in this research. The use of this polymer fuel, which results in very complex flow chemistry, mixed with the complexity of the arc physics, which may lead to severe thermal nonequilibrium, makes the thruster very difficult to analyze both theoretically and computationally. The primary goal of this research is to provide accurate thermochemical and transport properties of PTFE suitable for use in the flow regimes experienced in the PPT to aid in the theoretical and computational modeling of these complex thrusters.

A preliminary analysis is performed to judge the equilibrium state and flow characteristics of a typical thruster. The results give a range of Knudsen numbers of 10^{-3} to 10^{-1} indicating noncontinuum effects may be important in some operating regions. An examination of the ratios of characteristic times for ionization and thermal equilibration to characteristic flow times indicate that the thruster may progress through varying degrees of LTE. The ratio for ionization reactions varies from 10^{-3} to 10^{-6} and for thermal equilibration varies from 10^{-5} to 10^{-3} indicating that the thruster is, for the most part, in chemical equilibrium but may have an electron temperature that is elevated above the heavy particle temperature - a two-temperature LTE situation.

The chemical composition, thermodynamic, and transport properties of gaseous Teflon are calculated using a two-temperature LTE analysis in which the electron temperature may be significantly different than the heavy particle temperature. The results obtained here represent a significant improvement over the previously used equation-of-state, even for the single-temperature LTE case. The results for the transport properties show that the viscosity, thermal conductivity, and electrical conductivity may exhibit severe non-monotonic behavior.

AIAA-98-3662

DEVELOPMENT OF EQUATION-OF-STATE AND TRANSPORT PROPERTIES FOR MOLECULAR PLASMAS IN PULSED PLASMA THRUSTERS PART II: A TWO-TEMPERATURE EQUATION OF STATE FOR TEFLON

C.S. Schmahl, P.J. Turchi, P.G. Mikellides,
and I.G. Mikellides
The Ohio State University
Columbus, Ohio

34th AIAA/ASME/SAE/ASEE
Joint Propulsion Conference & Exhibit
July 13-15, 1998 / Cleveland, OH

DEVELOPMENT OF EQUATION-OF-STATE AND TRANSPORT PROPERTIES FOR MOLECULAR PLASMAS IN PULSED PLASMA THRUSTERS PART II: A TWO-TEMPERATURE EQUATION OF STATE FOR TEFLON

C. S. Schmahl, P. J. Turchi, P. G. Mikellides,
I. G. Mikellides
The Ohio State University
Columbus, Ohio
USA

ABSTRACT

The equation of state for gas phase polytetrafluoroethylene (PTFE) is calculated with a two-temperature LTE formulation. Twenty-five chemical species are included in the analysis. Sample calculations are performed for pressures from 0.001 atm to 1.0 atm and for temperature ranges of 0.1 ev to 4 ev for both heavy particle and electron temperatures. The preliminary results using the Mach2 MHD simulation program show large discrepancies between the calculated equation of state and that in the LANL SESAME tables used by Mach2. The results clearly show the importance of including complex molecular plasma effects in the simulation of the pulses plasma thrusters and related devices.

INTRODUCTION

Knowledge of the chemical, thermodynamic, and transport properties of a gas is required in almost any gas dynamic analysis. Accurate thermochemical and transport properties become particularly important in high-temperature applications such as the pulsed plasma thruster. In this paper, we shall concentrate on calculating the equation of state of a gas mixture. This is the necessary first step for determining the transport properties of a gas.

Very little information exists on the thermochemical properties of PTFE and its chemical constituents, especially in the plasma state. This is unfortunate for high-temperature thermochemical and transport data is needed for such devices as pulsed plasma thrusters (PPT), ablative re-entry heat shields, electronic components, plasma etching systems, and upper atmosphere modeling. Nonequilibrium properties are particularly important when studying electric discharges near Teflon surfaces and other nonequilibrium flows.

DEVELOPMENT OF MODEL FOR TEFLON PLASMA COMPOSITION

There are three primary thermochemical states possible for a gas. A calorically perfect gas has specific heats that are constant, and the enthalpy and internal energy are only functions of temperature. A thermally-perfect gas, in which variable vibrational and electronic excitation are taken into account, has specific heats, enthalpy, and internal energy that are all functions of temperature. If the conditions are right for chemical reactions to occur, then we can treat the gas as an equilibrium chemically-reacting gas for which properties area all functions of temperature and pressure. Even this can be generalized by stating that the reacting gas is in local thermodynamic equilibrium (LTE). This means that a local Boltzmann distribution exists at each point in the flow at the local temperature. We will extend this statement further for the case of a two temperature LTE gas modeled here. In this paper we calculate the chemical composition of the vapor phase Teflon.

In a previous paper[1], we detailed the calculation of the chemical composition of tetrafluoroethylene (C_2F_4). The analysis will included vibrational and electronic excitation, dissociation, first molecular ionization, and first through fourth monatomic ionization.

For a polyatomic base gas, C_2F_4 in our case, with the possibility of undergoing full dissociation, singular molecular ionization, and up to fourth monatomic ionization, we first assume there are twenty-five possible chemical species, which are C_2F_4, C_2F_2, CF_2, CF_2^+, CF_3, CF_3^+, CF_4, C_2, CF, CF^+, F_2, F_2^+, C^Z (Z=-1,4), F^Z (Z=-1,4), and$^-$ e 's. For a gas containing twenty-five chemical species, which is composed of three elements (C, F, e^-), we are required to have twenty-two (25-3=22) independent chemical reaction equations (laws of mass action). The reactions considered here are

$$CF_2 \rightarrow CF + F \qquad (1)$$

$$CF \rightarrow C + F \qquad (2)$$

$$F_2 \rightarrow 2F \qquad (3)$$

$$CF_2 \rightarrow CF_2^+ + e^- \qquad (4)$$

$$CF \rightarrow CF^+ + e^- \qquad (5)$$

$$C^{Z-1} \rightarrow C^Z + e^- \Big|_{Z=0}^{4} \qquad (6)$$

$$C_2F_4 \rightarrow 2\,CF_2 \qquad (7)$$

$$F_2 \rightarrow F_2^+ + e^- \qquad (8)$$

$$F^{Z-1} \rightarrow F^Z + e^- \Big|_{Z=0}^{4} \qquad (9)$$

$$C_2F_4 \rightarrow C_2F_2 + F_2 \qquad (10)$$

$$C_2F_4 \rightarrow CF_3 + CF \qquad (11)$$

$$C_2F_4 \rightarrow CF_4 + C \qquad (12)$$

$$C_2 \rightarrow 2C \qquad (13)$$

In actuality, there are other possible reactions that could yield the same chemical species. But, for an equilibrium calculation, the reactions chosen are arbitrary as long as they are linearly independent and account for all possible species.

Writing these reactions in terms of equilibrium relations for the partial pressures, we have

$$K_{p,j}(T) = \prod_i p_i^{\nu_i} \qquad (14)$$

where the $K_{p,j}$ are the equilibrium constants for the reaction (j) at the equilibrium temperature T, in terms of the partial pressures. Using the appropriate formulations, they may also be put in terms of concentrations, K_c, or number densities, K_N. It is important to note in the above equations that the equilibrium constants are written as functions of temperature only, as most authors point out. However, they may be functions of two or more state variables depending on whether such things as thermal non-equilibrium assumptions or electronic partition function cutoff is taken into account.[2]

In addition to twelve independent equations relating the twenty-five unknown partial pressures, we need three more equations to solve for the gas composition. The three chosen are; conservation of nuclei, Dalton's Law, and charge neutrality.

To solve the system of equations, we only need values for the equilibrium constants which may be calculated from equilibrium statistical mechanics. In terms of partition functions Q_i, the law of mass action for a general system is

$$K_N(T) = \prod N_i^{\nu_i} = e^{\frac{-\Delta\varepsilon_0}{kT}} \prod Q_i^{\nu_i} \qquad (15)$$

where ν_i is the stoichiometric mole number for species (I), that is, the coefficients in the balanced chemical equation, $\Delta\varepsilon_0$ is the reaction energy (change in zero-point energy) and Q_i is the total partition function for species (I). Thus, for a given reaction and thermodynamic state, the only unknowns in Eq. (23) are the Q_i's.

Note that Eqn. (15) contains only one temperature. For the two temperature case considered in this research we make the assumption that the heavy-particle gas composed of neutrals and ions, has a Maxwellian distribution in velocities and a Boltzmann distribution in energies at a heavy-particle temperature , T. The electron gas, composed of both free and bound electrons is in equilibrium with an electron temperature T_e defined by their Maxwellian velocity distribution. Thus, we have defined a two-temperature LTE situation. Quantum mechanics gives us theoretical values for the quantized energies of a particle, at least for the translational, rotational, and vibrational modes.[3] Along with the assertion that particle energy is simply the sum of the modal energies, that is, the internal energies are uncoupled, which is a consequence of the more fundamental assumption of a separable Hamiltonian, the partition function is expressed as the product of the modal partitions Q_j, where

$$Q = \prod Q_j \qquad (16)$$

with j extending over all modes. For each case the total vibrational partition function is taken as the product of the partition function for each of the vibrational degrees of freedom . As stated earlier, we have assumed uncoupled energy modes. That is, we assume that the energy exchange between energy modes is small. As a result each energy mode which is equilibrium at its temperature, in our case either T or T_e, is statistically independent from all others. Thus for our multi-temperature system we can write

$$Q = \prod Q_i(T_i) \qquad (17)$$

where T_i is the equilibrium temperature of the mode.

Note that the Boltzmann factor, $e^{-\beta\epsilon j}$, in the above equations for the partition functions is written as derived in the standard one-temperature system case. That is, where $\beta = 1/kT$. It has been known for a long time that certain molecules have the tendency to have their vibrational modes to be a strong function of electron temperature, that is $T_v = T_e$ instead of T. Atmospheric gasses, especially nitrogen are well known for this property[4,5]. This phenomena is thought to be largely due to the propensity of the molecule for vibrational resonance. Since we are dealing with a gas mixture containing twelve molecular species a more formal examination of the situation is required to support our assumptions. We define a parameter η which quantifies the fractional energy exchange between thermal systems, in our case it is the fractional energy exchange between systems at the equilibrium electron temperature, ie. the electron gas, and other internal modes. From the results derived in Appendix 1 we find that our Lagrange multiplier β becomes

$$\beta = \frac{\eta T_H + (1 - \eta) T_e}{k T_H T_e} \qquad (18)$$

At this point in time, research is being done on how to set the η parameter effectively. Consistent with the assumptions made thus far we have for the interaction of free electrons and bound electrons $\eta = 1$ thus $\beta = 1/kT_e$ for Q_e. And for the interaction of free electrons and the translational, rotational, and vibrational modes $\eta = 0$ thus $\beta = 1/kT_h$ for the partition functions for these modes.

The equations given in the previous section to calculate the equilibrium composition in terms of partial pressures, given T , T_e and P, provide a closed set of twenty-five coupled nonlinear algebraic equations for which there is no analytic solution and numerical methods must be used. Figure 1 displays the single temperature chemical composition for a pressure of one atmosphere, clearly showing that many molecular species may exist in the PTFE chemical composition, especially for temperatures below 5000 K. Figures 2 through 4 indicate that thermal nonequilibrium can have a large effect on the chemical composition.

CALCULATION OF THE THERMODYNAMIC PROPERTIES

For a given temperature and pressure, the complete gas composition is calculated using the techniques in the previous section. Often, however, it is necessary to have the thermodynamic properties of the gas. In this research, the calculated thermodynamic properties are specific enthalpy (h), specific internal energy (e). The specific heats (c_p and c_v), and consequently the ratio of specific heats (γ), were not calculated for there is some ambiguity as to the definition of specific heat for a multi-temperature system and they are rarely used in high-temperature calculations anyway.

On a microscopic scale, a particle (atom or molecule) may possess energy due to its translational, rotational, vibrational, and electronic modes. This is expressed as

$$e_i = e_i^{trans} + e_i^{rot} + e_i^{vib} + e_i^{el} \qquad (19)$$

where e is the total specific internal energy. Note that e is actually the total specific sensible internal energy and is measured above the zero point ($e = e - e_{0,i}$ where $e_{0,i}$ is the summation of the zero point energies for the individual modes of translation, vibration, and electronic. The rotational mode has no zero point energy. In terms of partition functions, the energy and enthalpy for a one temperature system is expressed as[6]

$$e = RT^2\left(\frac{\partial \ln Q}{\partial T}\right)_v \qquad (20)$$

$$h = RT + RT^2\left(\frac{\partial \ln Q}{\partial T}\right)_v \qquad (21)$$

with the relation

$$h = e + Pv \qquad (22)$$

holding for any type of gas, whether calorically perfect, thermally perfect, or chemically reacting. The expressions for the modal partition functions explained earlier. For a multi-temperature system, composed of n subsystems each in equilibrium at their own temperature T_n, as long as the subsystems are statistically independent then the fundamental thermodynamic relations may be applied to each temperature subsystem separately[7], thus we write Eqs. (20) and (21) as

$$e = RT_n^2\left(\frac{\partial \ln Q_n(T_n)}{\partial T_n}\right)_v \qquad (23)$$

$$h = RT_n + RT_n^2\left(\frac{\partial \ln Q_n(T_n)}{\partial T_n}\right)_v \qquad (24)$$

For a mixture of N species, the total mixture sensible internal energy is

$$e = \sum_{i=1}^{N} c_i e_i \qquad (25)$$

where c_i is the mass fraction of species I, given by

$$c_i = \frac{m_i}{m} = \frac{\rho_i}{\rho} \qquad (26)$$

Similarly, the specific enthalpy for a mixture of N species is given by

$$h = \sum_{i=1}^{N} c_i h_i \qquad (27)$$

$$h_i = e_i + R_i T + \left(\Delta h_f\right)_i^0 \qquad (28)$$

The internal energy and chemical enthalpy at each required temperature and pressure is calculated using Eqs. (23)-(28).The solution procedure required a previous call to the equilibrium composition subroutine to input the partial pressures and mixture molecular mass. The electronic derivatives appearing in Eq. (23) are calculated using a 4th-order four-point Richardson extrapolation with ΔT = .01K. The derivatives were taken with a frozen principal quantum number cutoff. This was done for ease of calculation and to avoid the problem other authors[18] experienced with large computational derivatives being obtained if the temperature and pressure state corresponded to a partition function jump due to the addition or subtraction of another electronic level.

COUPLING OF EQUATION OF STATE TO MACH2 CODE

For equation of state properties the Mach2[9] code is designed to utilize the LANL SESAME[10] tables translated through a subroutine package called EOSPACK[11]. The equation of state properties are divided into three main tables: total , ion, and electron eos. Each table consists of three sub-tables: pressure and energy as functions of density and temperature, and temperature as functions of density and specific thermal energy. For a two-temperature calculation, the EOSPAC utility will estimate the ion contributions and subtract from the total to obtain the electron contribution. For a single temperature calculation all necessary data can be obtained from the total eos table. It is reasoned that this scheme is sufficient to model both single and multi-temperature monatomic gasses and single temperature polyatomic gasses. But unfortunately is insufficient to model multi temperature polyatomic gasses for there is no way of preserving the molecular internal energy. To treat this problem a multi-dimensional curve fitting procedure to model the total multi-temperature equation of state is under development. Accompanying this are the necessary modifications to Mach2 to bypass the need for EOSPAC. Thus, the comparisons made here are for a range of values as a function of electron temperature at constant density and heavy particle temperature. Thus for comparison we specify T_e and T_i and the density for which we calculate the ion and electron energies and pressures from the thermochemical code. These results are fed to Mach2 at the same density for which the code returns values for the temperatures and pressures. In theory, comparison of the two results should give a scale of importance of the two-temperature molecular calculation. At high temperatures the results should nearly coincide. To make the new equation of state compatible with Mach2 the internal energies are put in terms of the total internal energy, that is, the energies include the zero point energies, which in this case are approximated to be the zero point formation enthalpies such as in Eq. 28. For an accurate comparison to SESAME values the zero point energies are shifted up by 7.3504 MJ/kg to coincide with SESAME values. Also, the electronic contribution to the internal energy is grouped in with the electron energy. Figures 5 through 7 show the calculated mixture ion and electron energies and pressures for a density of 0.4 kg/m^3 at a heavy particle temperature of 0.1 eV. Note the strong fluctuation present in the ion contributions due to molecular chemical reactions.

COMPARISON OF NEW TEFLON MODEL WITH SESAME MODEL

To test the two-temperature equation of state with that of SESAME an initial calculation is performed for a density of 0.4 kg/m^3 and a heavy particle temperature of 0.1 eV. Calculation are performed for four different values of electron temperatures: 0.1, 0.2, 0.5, and 1.0 eV. The electron and ion energies obtained from the two-temperature molecular model are given to Mach2 which returns the values of temperature and pressure that SESAME predicts. The results of this calculation, shown in Fig. 9, clearly indicate large differences in the predicted temperatures and pressures. To check if agreement is obtained when few or no molecules are present an isothermal calculation is performed at temperatures of 1, 2, 3, and 4 eV at a pressure of 1/1000 atm. The results, shown in Fig. 10, indicate an interesting phenomena. The ratio of temperatures and pressures obtained by Mach2 using the SESAME equation of state for Teflon is approximately equal to a constant, 2.3. Indeed the two equations of state do not agree when it is predicted that they should. The results obtained through Mach2 and EOSPAC using SESAME return values approximately 2.3 times higher than that calculated here. Another point that should be made is that 2.3 is very close to 2.303 or the natural logarithm of 10, which is the temperature increment that seems used in the SESAME table for Teflon. A comparison of the results of Kovitya[12] for the enthalpy is shown in Fig . 11. In the range of 5,000 to 30,000 K the percent differences range from about 20 to 30 %, Kovitya's values being the larger. Differences are to be expected for the calculations were performed differently and the properties above 6000 K are obtained in a very approximate way. This suggests that the true values should lie close to the results obtained here. Further investigation of this discrepancy must be performed before a definitive statement of the error source is made. Even with this difference present it can be seen from Fig. 9 that in the molecular region the results deviate by a much larger factor than this . Which still indicates that the differences obtained between the two calculation are important and thus two-temperature molecular effects must be included for the complete Teflon model.

CONCLUDING REMARKS

A two-temperature molecular equation of state for PTFE has been calculated. Comparison with the LANL SESAME tables indicate that differences are present, the source of which is a matter for further investigation. Independent of this fact, it is also shown that multi-temperature molecular effects on the equation of state may play a critical role in proper modeling of devices such as the pulsed plasma thruster. Future direction of this research include the development of the reactive transport model for Teflon and the procedure for accurate incorporation of multi-temperature equations of state for computational simulations.

APPENDIX 1

For statistically independent subsystems, the energy, entropy and other thermodynamic quantities are still additive. Thus

$$S = \sum S_n \quad and \quad E = \sum E_n \tag{29}$$

Taking the derivatives of the above we get

$$dS = \sum dS_n \ and\ dE = \sum dE_n \tag{30}$$

Using the proper form for the second law for a multi-temperature system[7]

$$dS \geq \sum \frac{\delta Q_n}{T_n} \tag{31}$$

where $\delta Q_n = dE_n + \delta W_n$, and $\delta W_n = p_n dV$. Then we see that

$$(dS)_{N,T,V} \geq \sum \frac{dE_n}{T_n} \tag{32}$$

Now, for brevity, we invoke the relation, without proof that[13,6]

$$S = kN\ln(Q) + k\beta E \tag{33}$$

And due to the fact that the *n* subsystems are statistically independent such that the above equation, which is derived for a system in thermodynamic equilibrium also holds for all separate subsystems then we write[7]

$$S_n = kN \ln(Q_n) + k\beta E_n \tag{34}$$

so that

$$(dS)_{N,T,V} = k\beta dE \tag{35}$$

therefore

$$k\beta \sum dE_n = \sum \frac{dE_n}{T_n} \tag{36}$$

For our two-temperature system

$$\sum dE_n = dE_H + dE_e \tag{37}$$

and

$$\sum \frac{dE_n}{T_n} = \frac{dE_H}{T_H} + \frac{dE_e}{T_e} \tag{38}$$

thus

$$k\beta\left(dE_H + dE_e\right) = \frac{T_e dE_H + T_H dE_e}{T_H T_e} \tag{39}$$

Now we define an "economy" between the heavy particle and electron energies, η, which defines the fractional contribution of each to the total energy in any state. Lets express it as

$$E_e = \eta E \tag{40}$$

and

$$E_H = (1 - \eta) E \tag{41}$$

Then

$$dE_e = \eta dE \tag{42}$$

and

$$dE_H = (1 - \eta) dE \tag{43}$$

which upon substitution into Eq. (39), and the subsequent cancellation of dE yields that.

$$\beta = \frac{\eta T_H + (1 - \eta) T_e}{k T_H T_e} \tag{44}$$

with the limits that if

$$\eta = \begin{cases} 1 & \rightarrow \quad \beta = \dfrac{1}{kT_e} \\ 0 & \rightarrow \quad \beta = \dfrac{1}{kT_H} \end{cases} \tag{45}$$

ACKNOWLEDGMENTS

The support of this work by AFOSR/NA is gratefully appreciated. The authors would like to thank R.E. Peterkin Jr., USAF Phillips Laboratory, Kirtland AFB, NM, The Ohio Supercomputer Center, and NASA.

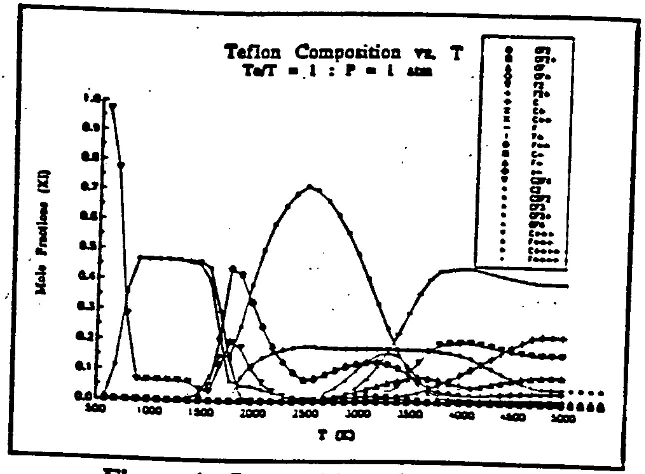

Figure 1. Composition of Teflon for Te/T = 1.0 at 1 atm.

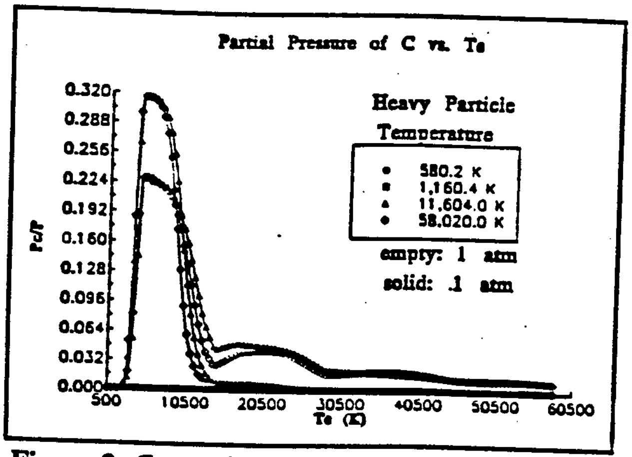

Figure 2. Composition of Teflon for Te/T = 1.0 at 1 atm. Lower temperature range.

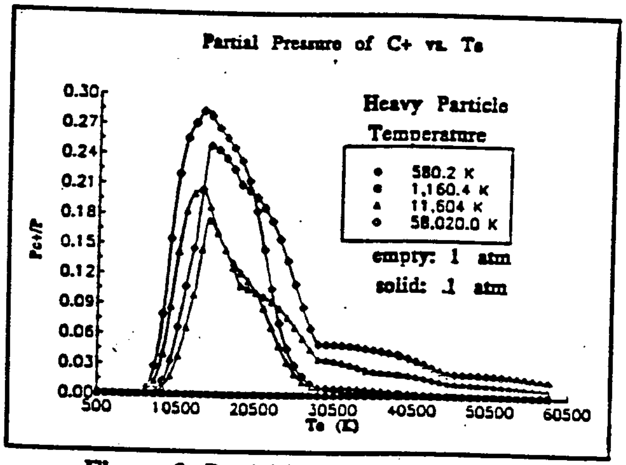

Figure 3. Partial Pressure of C vs. Te.

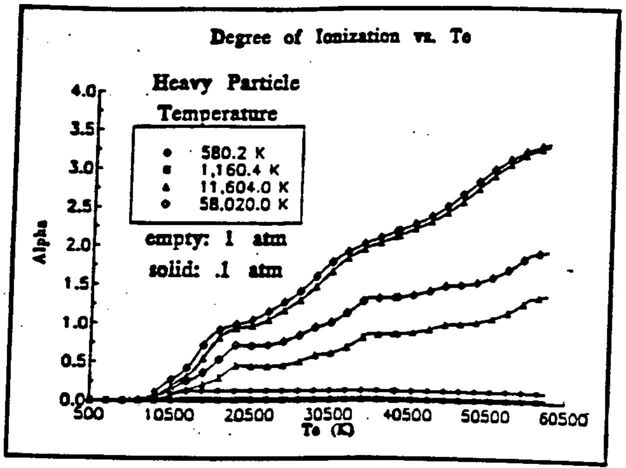

Figure 4. Partial Pressure of C^+ vs. Te.

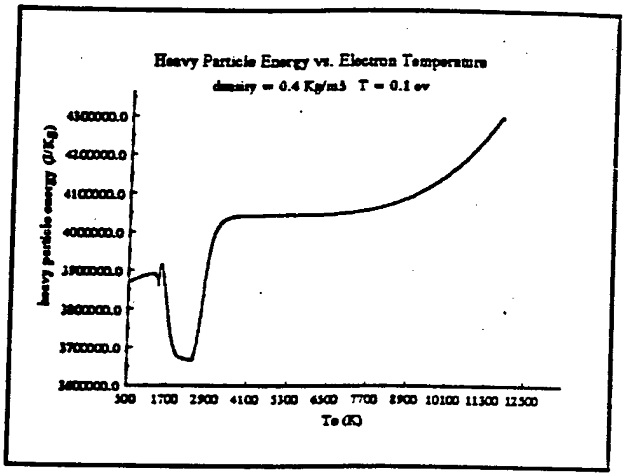

Figure 5. Partial Pressure of F vs. Te.

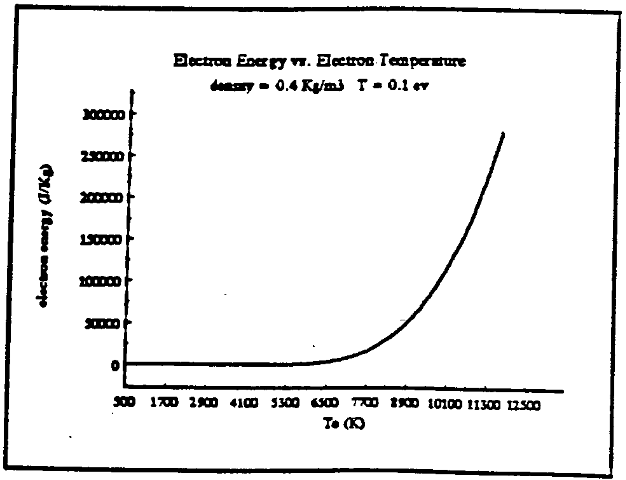

Figure 6. Partial Pressure of F^+ vs. Te.

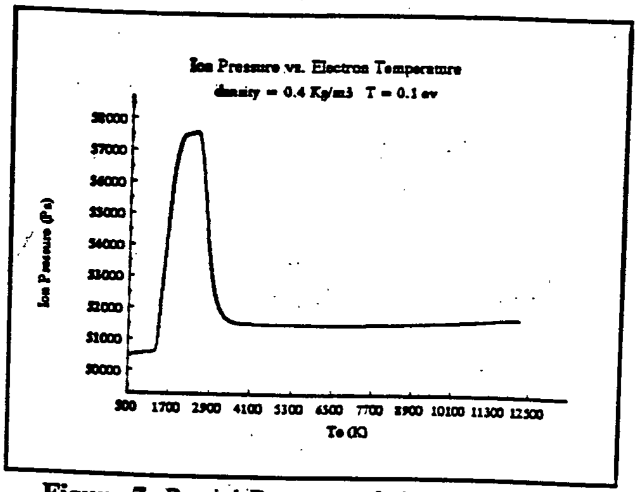

Figure 7. Partial Pressure of electrons vs. Te.

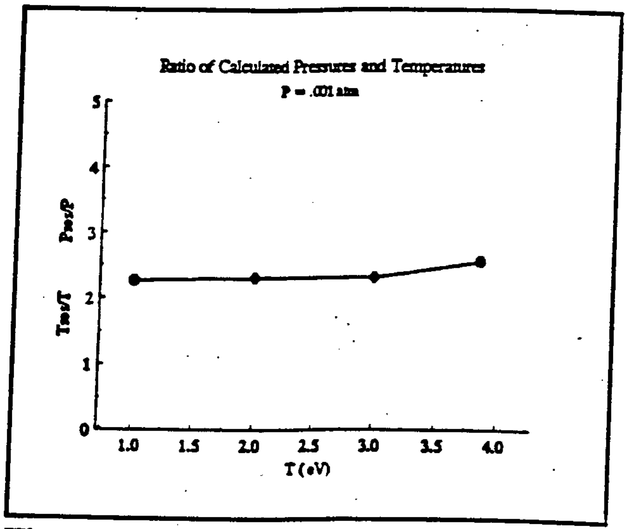

Figure 10. Comparison of high-temperature results with that obtained from Mach2 using SESAME tables for Teflon.

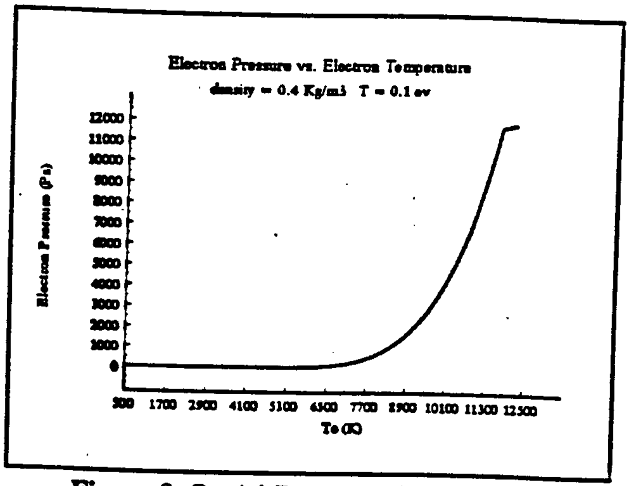

Figure 8. Partial Pressure of CF_2 vs. Te.

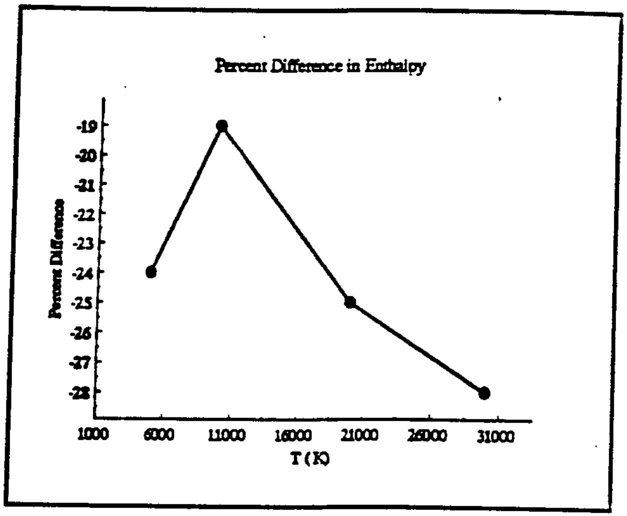

Figure 11. Comparison of calculated enthalpy with that obtained by Kovitya

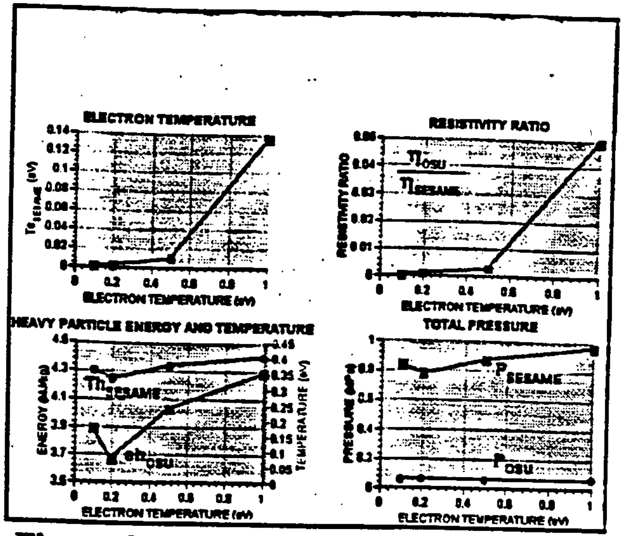

Figure 9. Comparison of eos values in molecular region.

REFERENCES

[1] Schmahl, C.S., P.J. Turchi. 1997. " Development of Equation-of-State and Transport Properties for Molecular Plasmas in Pulsed Plasma Thrusters Part I: A Two-Temperature Equation of State for Teflon." 25th International Electric Propulsion Conference, Aug 24-28, Cleveland, Ohio. IEPC-97-124

[2] Schmahl, Christopher S. A Computational Study of Shocked Flow Heat Transfer with Improved Equation of State and Transport Properties - A Case Study for Nitrogen. Master's Thesis. The Ohio State University. 1996.

[3] Liboff, Richard L. 1992. Introductory Quantum Mechanics, 2nd ed. Addison-Wessley

[4] Rich, J. William, S. O. Macheret, I. V. Adamovich. 1996. " Aerothermodynamics of Vibrationally Nonequilibrium Gases." Exp. Thermal and Fluid Sci. 13:1-10

[5] Dunn, Michael G., personal communication.

[6] Vincenti, Walter G., Charles H. Kruger Jr. 1965. Introduction to Physical Gas Dynamics. New York: Wiley.

[7] van de Sanden, M. C. M., et al. 1989. " Thermodynamic Generalization of the Saha Equation for a Two-Temperature Plasma." Phys. Rev. A. 40.9 Nov: 5273-5276

[8] Drellishak, K.S., C.F. Knopp, A.B. Cambel. 1963. " Partition Functions and Thermodynamic Properties of Argon Plasma." Phys. Fluids. 6.6 Sept: 1280-1288.

[9] Peterkin, Robert E, Jr., et al. Mach2 : A Reference Manual, 5th ed. MRC-ABQ-R-1490

[10] Holian, K. S., ed, "T-4 Handbook of Material Properties Database, Vol Ic: EOS, LA-10160, LANL, Los Alamos , NM, Nov 1984

[11] Cranfill, C. W., "EOSPAC: A Subroutine Package for Accessing the Los Alamos Sesame EOS Library," LA-9728-M, LANL, Aug. 1983

[12] Kovitya, P. 1984." Thermodynamic and Transport Properties of Ablated Vapors of PTFE, Alumina, Perspex, and PVC in the Temperature Range 5000-30,000 K." IEEE Transactions on Plasma Science. PS-12.1 March: 38-42.

[13] Tein, Chang L, J. H. Lienard. 1971. Statistical Thermodynamics. Hemisphere Publishing

AIAA 98-3804

DESIGN, OPERATION, AND INVESTIGATION OF AN INDUCTIVELY-DRIVEN PULSED PLASMA THRUSTER

H. Kamhawi and P.J. Turchi

The Ohio State University
Columbus, Ohio

34th AIAA/ASME/SAE/ASEE Joint Propulsion Conference & Exhibit
July 13-15, 1998 / Cleveland, OH

For permission to copy or republish, contact the American Institute of Aeronautics and Astronautics
1801 Alexander Bell Drive, Suite 500, Reston, VA 20191

DESIGN, OPERATION, AND INVESTIGATION OF AN INDUCTIVELY-DRIVEN PULSED PLASMA THRUSTER

H. Kamhawi and P.J. Turchi

The Ohio State University
Columbus, Ohio USA

ABSTRACT

An inductively-driven Pulsed Plasma Thruster (PPT) has been designed, built, and its performance evaluated. Two configurations were built, the first using two spark plugs to actuate plasma flow in PPT1 and for the crow-barring of the inductive store; for the second configuration only one spark plug was used and the crow-barring of the inductive store was actuated by the plasma flow from PPT1. For the second configuration, voltage and current waveforms, mass loss, and impulse-bit data were obtained for energy levels ranging from 20 J to 60 J. Tests were performed for two values of inductive store inductances and for interelectrode gaps of 1.91 cm and 2.54 cm. Experimental current and voltage waveforms show substantial reductions in current and voltage reversals for crow-barred operation. Specific Impulse and thrust efficiency values of 1800 sec and 5%; respectively, are obtained.

INTRODUCTION

The Pulsed Plasma Thruster (PPT) has been successfully employed in space for two decades. It has demonstrated satisfactory performance on low average-power satellites, and is a candidate for future missions involving small satellites[3]. The conventional PPT circuit operation is similar to an LRC circuit operation, where the circuit current and voltage oscillate because of a mismatch between the arc discharge impedance and the characteristic impedance of the LRC circuit. Experimental evaluation of the OSU benchmark PPT has shown that specific impulses of 1000 sec are attainable but at thrust efficiencies that are typically less that 10%[1]. Part of this low efficiency is related to this electrical impedance mismatch. In addition, numerical simulations with the MACH2 code indicated that late-time ablation of the Teflon propellant is a main contributor to the PPT low efficiency[2]. This low efficiency allows for the potential for significant improvement in PPT performance through further research.

To improve the efficiency of the PPTs new circuits have been devised and built. Earlier work demonstrated that these new circuit designs allow for better matching between the arc discharge impedance and the characteristic impedance of the LRC circuit, resulting in higher thrust efficiencies[3]. The new circuit designs are presented in Figures 1 and 2. These new circuit arrangements provide reduced voltage reversals on the

[illegible]

capacitor and result in improved capacitor lifetime. This paper describes two thruster configurations, experimental facilities, current and voltage waveforms, mass loss data, average thrust and impulse-bit data for the configurations that were tested. In addition, the experimental results are compared with a quasi-steady state numerical model.

EXPERIMENTAL APPARATUS

Two inductively-driven advanced PPTs were designed and built. Figures 1 and 2 present schematics of configurations 1 and 2; respectively. Figure 3, shows a circuit schematic for the inductively-driven PPT. For both configurations, the design consisted of a single capacitor to store the initial electrical energy, an intermediate inductor, and two PPTs that act as switches. For both configurations, the same 0.64 cm thick ground and hot transmission lines were used. The ground transmission line is 8.89 cm Long and is 36.8 cm wide. The ground transmission line has a 12 cm X 6.67 cm square opening to allow for the insertion of the hot electrode and the insulating plexiglas assembly. The hot transmission line is 26 cm long and 2.54 cm wide. The new circuits are operated by first charging the capacitor to a desired high voltage. PPT1 is then triggered resulting in the capacitor discharging and storing part of its energy in the inductor which is in series with PPT1. The inductive store terminals are insulated from each other using a 2.54 cm long Plexiglas piece as shown in Figures 1 and 2. Shortly after the current in the inductor reaches its peak value, the second PPT is fired discharging the stored inductive energy and performing work on the PPT plasma.

For configuration 1, two Unison spark plugs were used and were triggered by a double ignition circuit that was designed and built by the Power Electronics group at LeRC Electric Propulsion Laboratory. The double ignition circuit was designed to generate two high voltage pulses (up to 5 kv, with a 20 µsec width) that would trigger the Unison spark plugs. The time delay between the two triggering pulses can be varied from 0 to 50 µsec. Before setting the time delay, only PPT1 would be fired in order to determine the time delay required for proper operation. The advanced PPT was operated by first charging the capacitor to the desired voltage, then the spark plug was triggered, then after a specified time delay that was set using the double ignition circuit, the second spark plug was triggered to initiate the crow-baring discharge in PPT2. During the testing of configuration 1, it was noticed that advanced PPT was not always operating in the proper mode and two major problems were observed. The first problem was that the second ignition pulse was triggering PPT2 10 to 20 µsec later than required although the time delay was set correctly; therefore, resulting in an improper discharge of the stored inductive energy. In addition, by not triggering PPT2 at the correct time the voltage on the capacitor was reversing up to 80% of the original charging voltage, thus reducing capacitor lifetime. The second problem encountered was that about 30% of the time PPT2 would trigger before PPT1; therefore bypassing the inductive store and acting as a conventional PPT. Further testing indicated that the two problems were occurring because the breakdown in the interelectrode region for both PPTs was not occurring when the spark plug was triggered. It was observed that breakdowns in the interelectrode regions would occur 5 to 25 μsec after the sparkplug was triggered. These uncontrollable time delays in the breakdown resulted in a 80% failure rate for proper triggering of the advanced PPT.

To eliminate the problem of false triggering, and to simplify and reduce the number of components required for successful advanced PPT operation; configuration 2, presented in Figure 2, was designed and built. In this design, the plasma generated in PPT1 discharge was used to actuate the crow-barring discharge. As shown in Figure 2, one Unison spark plug triggered was used. This modified design included the addition of a crow-bar electrode and transmission line. The crow-bar electrode and transmission line were insulated from the ground electrode and transmission line using Kapton sheet and tape. The U-shaped Boron Nitride (BN) insulating piece prevented the premature breakdown between the crow-bar and ground electrodes. The Unison spark plug whose chassis is grounded was enclosed in a thin-walled Teflon tube to electrically insulate it from the crow-bar electrode.

EXPERIMENTAL FACILITIES

PPT experiments were performed at the Ohio State University Aeronautical and Astronautical Research Laboratory (AARL) and at NASA Lewis Research center (LeRC) Electric propulsion Laboratory. Mass loss tests were performed at NASA LeRC in VACFAC 54[1] which is evacuated using roughing pumps in conjunction with an oil diffusion pump. A 33.3 μf pulse discharge oil-filled Maxwell Laboratories capacitor was used for these experiments.

EXPERIMENTAL RESULTS

Current and voltage waveforms, mass loss data, and impulse-bit data were collected to evaluate the performance of the advanced PPT. Tests were performed with configuration 2 for two different inductive store with inductances L_{s1} and L_{s2} and different PPT1 Teflon interelectrode gaps (1.91 and 2.54 cm); respectively. L_{s1} is a 12 turn toriodal inductor with an I.D. of 6.35 cm and an O.D. of 11.43 cm; its height is 1.27 cm, its made of 10 gauge wire. L_{s2} is a 25.4 cm long 10 Gauge wire. The calculated inductance and resistance for L_{s1} are 1 μH and 3 mΩ; respectively, and are based on the entire cross section of wire used. Whereas, for L_{s2} the calculated inductance and resistance are 0.25 μH and 0.8 mΩ; respectively, and are based on the entire cross section of wire used. For configurations 2a and 2b, the inter-electrode gap was 1.91 cm with inductances L_{s1} and L_{s2}; respectively. For configurations 2c and 2d the inter-electrode gap was 2.54 cm with inductances L_{s1} and L_{s2}; respectively .

Voltage and Current Waveforms

To measure the current in the circuit a Pearson 101 Current Monitor was used in conjunction with a PP001 10X

Lecroy voltage probe. The current monitor has a 5.08 cm. I.D. with an accuracy of 1 %, its output sensitivity is 0.01 volt/amp with a maximum current rating of 50,000 amps. The inductive store wire was passed through the current monitor for current monitoring. The 10x voltage probe was used with the current monitor to reduce the magnitude of the signal read by the Lecroy 9314 oscilloscope. The combination of the Pearson current monitor and the 10x voltage probe resulted in an output sensitivity of 0.001 volt/amp. To measure the capacitor voltage, a coaxial cable was connected to the capacitor output leads and to a BNC output feedthrough, then the P6015A 1000x Tektronix high voltage probe was connected to a BNC-GR-Banana plug adaptor. A Rogowski coil was placed around the capacitor hot output lead to monitor the capacitor's output current. The Rogowski coil has 45 turns of 20 gauge wire wrapped around a toroidal plexiglass piece that has an I.D. of 2.08 cm, O.D. of 3.10 cm, and is 0.53 cm thick. Since the output of the Rogowski coil exceeded the range allowed on the oscilloscope, a 50Ω voltage divider was used to reduce the magnitude of the signal inputted into the oscilloscope. The Rogowski coil output had a calibration factor of $3.3005X10^9$ amp/volt and with an accuracy of 5%. For all configurations voltage, current, and dI/dt waveforms were collected for both an insulated crow-bar electrode and exposed electrode. Results are presented for the 60 J case for configurations 2a, 2b, 2c, and 2d in Figures 4, 5, 6, and 7; respectively.

Current and voltage waveforms were collected for all energy levels. In Figures 4a, 5a, 6a, and 7a current waveforms are presented for PPT operation at 60 J for configurations 2a, 2b, 2c, and 2d; respectively. Each figure presents two waveforms; the first waveform (solid line) shows results for advanced PPT operation with an exposed crow-bar electrode and the second waveform (dashed line) shows results for advanced PPT operation with an insulated crow-bar electrode. By comparing the solid and dashed lines, it is clear that the presence of the crow-bar electrode is allowing the inductive store to discharge its initially stored energy, whereas without the crow-bar electrode the current waveform oscillates and the circuit behaves as a under-damped LRC circuit. Peak currents of 8281, 15625, 8437, and 17031 amps are obtained for crow-bar operation for configurations 2a, 2b, 2c, and 2d; respectively, whereas, peak currents of 9218, 17656, 9218, and 17812 amps are obtained for insulated crow-bar operation. This indicates that PPT2 was actuated before PPT1 current reached its peak. This problem can be solved by increasing length of the insulated area in the crow-bar electrode, thus forcing the plasma to travel for a longer time and resulting in a time delay for crow-barring. Analysis of the under-damped current waveforms allows for the prediction of the circuit R and L values. This is performed by evaluating the waveform period and rate of exponential decay. This was performed for all energy levels for configurations 2c and 2d. For configuration 2c, the circuit inductance and resistance were approximately 1 μH, and 44mΩ; respectively, while for configuration 2d, the circuit inductance and resistance were approximately 0.280 μH, and 30 mΩ; respectively.

In Figures 4b, 5b, 6b, and 7b capacitor voltage waveforms are presented for PPT operation at 60J for configurations 2a, 2b, 2c, and 2d; respectively. Each Figure presents two waveforms; the first waveform (solid line) shows results for advanced PPT operation with an exposed crow-bar electrode and the second waveform (dashed line) shows results for advanced PPT operation with an insulated crow-bar electrode (under-damped). By comparing the solid and dashed lines it is noticed that having the crow-bar electrode reduced the voltage reversal on the capacitor and thus will result in increased capacitor lifetime.

Mass Loss Data:

Mass loss data were obtained for configuration 2 only because it can be operated reliably for thousands of pulses. A Toledo Metler AE 163 balance, with a readability of 0.01 mg, was used to weigh the Teflon and BN pieces prior to and after conducting the mass ablation tests. For all tests , the thruster was fired for approximately 3000 pulses for energy levels of 40 J or less, for higher energy levels the thruster was fired for approximately 1500 pulses; tests were performed at a facility pressure of around $5X10^{-5}$ Torr. For configurations 2a and 2b mass loss data were obtained at energy levels of 20, 40, 50, and 60 J, while for configurations 2c and 2d, mass loss data were obtained for energy levels of 40, 50, and 60 J. Results are presented in Figure 8 with an accuracy of 5%.

Results presented in Figure 8 show that mass loss data for configurations 2c and 2d are higher than those for configurations 2a and 2b, thus indicating that a larger gap results in higher mass loss for a given energy level. Furthermore, mass loss for configurations 2b an 2d are higher than those for configurations 2a and 2c; respectively. This corresponds to the fact that the inductive store inductance for configurations 2b and 2d (L_{s2}) is lower than the inductance for the inductive store (L_{s1}) for configuration 2a and 2c, thus resulting in higher peak currents for configurations 2b and 2d which results is a higher mass loss. The BN mass ablation varied between 0.4 to 1.5 μg for energy levels between 20 and 60J; respectively.

It is important to note that when L_{s1} was in circuit which results in lower peak current for a given energy level, substantial carbonization on Teflon surface occurred. For all cases, the carbonized area was larger for lower energy operation. This surface carbonization indicates that the heat flux to the Teflon surface was not enough to ablate the entire Teflon molecules but was only enough to break some of the bonds in a Teflon molecule.

Impulse-Bit Measurements:

Impulse-bit and average thrust measurements were performed in tank 3 vacuum facility at NASA LeRC. The thrust stand used is a torsional-type capable of measuring thrust of PPTs in single shot or repetitive firing modes[5]. The thrust stand was calibrated using three weights of approximately 25 mg each. Impulse-bit and average thrust data were obtained for the 33.3 μF capacitor for configurations 2a, 2b, 2d, and 2a with an insulated crow-bar electrode; tests were conducted at a facility pressure of less than 2 X 10^{-6} Torr. During all tests, the inductive store current was monitored to assure that the inductive store was properly crow-barred. For configurations 2a and 2b, impulse-bit measurements were made at energy levels of 40, 50, and 60 J. At each energy level 20 single-shot measurements were made then the thruster was run for 5 minutes to collect the average thrust data. For configuration 2a, the crow-bar electrode was insulated and impulse-bit data were collected at energy levels of 40, 50, and 60J. For configuration 2d, impulse-bit data were collected at energy levels of 20, 40, 50, and 60J. At each energy level 10 single-shot measurements were recorded then the thruster was run for 3 minutes to collect average thrust data. Results are presented in Figures 9 with an accuracy of 10%.

Results presented in Figure 9, show that impulse-bit data for configuration 2b are almost 100% higher than those for configuration 2a. This can be explained by noting that the peak currents for configuration 2b are more than double those for configuration 2a, resulting in more ablated mass and higher electromagnetic force contributions. In addition, impulse-bit for configuration 2d are generally higher than those for configuration 2b, although at 40J the discrepancy between them is less than 2% and becomes 11% at 60J. These elevated impulse-bits are mainly due to the increased exposed Teflon area which results in higher ablated mass. Comparing results for configuration 2a with the crow-bar electrode exposed and insulated, shows that impulse-bit values for the insulated crow-bar are generally 60% higher than those for the exposed crow-bar electrode. This is mainly due to additional contribution to the impulse-bit from the current reversal.

Using the mass loss and impulse-bit data the Specific Impulse (I_{sp}) and efficiency (η) of the advanced PPT can be calculated by

$$I_{sp} = \frac{I_{bit}}{m_{loss}} \qquad (1)$$

$$\eta = \frac{I_{bit}^2}{2\ E\ m_{loss}} \qquad (2)$$

Figure 10, presents results for the specific impulse (I_{sp}) for the different configurations and energy levels. There are no trends that can be generalized but it is important to note that for all of the cases considered $_{Is}$ values were greater than 1250 sec. Figure 11, presents efficiency (η) values for the various configurations. It is important to note that for configurations 2b and 2d the thruster efficiency was almost double that of configuration 2a, thus again confirming contributions due elevated PPT currents. In Figures 12 and 13, mass loss and I_{bit} are plotted vs. $\int i^2(t)\, dt$. In both figures, mass and impulse-bit scale linearly with $\int i^2(t)\, dt$. Figures 12 and 13, show that higher PPT peak currents correspond to higher mass loss rates and higher impulse-bits.

THEORETICAL ANALYSIS

The impedance of the arc can be evaluated using an idealized quasi-steady 1-D model in the limit of high magnetic Reynolds number and β approaching zero[6]. Assuming the flow is magnetosonic at channel exit, the flow speed can be calculated and is given by

$$u_1 = \frac{B_0^2}{(3\mu w)} \qquad (3)$$

where B_0 is the stagnation magnetic field and w is mass flow rate. Then by requiring that all dissipation occurs in first conduction region and setting that equal to mass flow rate times absorbed heat and gained kinetic energy, one can solve for the flow rate w and get an expression for u_1

$$u_1 = 2.076 \sqrt{Q} \qquad (4)$$

where Q is the total energy required to ablate, dissociate and ionize a Teflon molecule and is equal to 61.5 eV. Then by knowing u_1 the arc impedance can be calculated and is given by

$$z = 2.076 \sqrt{Q} \left(\frac{h}{W}\right) \frac{\mu}{\sqrt{3}} \qquad (5)$$

where h and W are the arc length and width. For h/W equal of 1 the arc impedance is 16.34 mΩ. A slug code, that solves the circuit's ODE's, was developed at Ohio State University[7]. The code was modified to predict the current waveforms generated by a quasi-steady arc case. The arc impedance and the circuit external resistance are inputted to the code. Results are presented in Figure 14 for operation with L_{s1}. Figures 14 show that the experimental and numerically predicted waveforms agree.

CONCLUDING REMARKS

An inductively-driven PPT has been designed, built, and its performance evaluated. Experimental results indicate that plasma generated from the initial discharge in PPT1 can be used to actuate the crow-barring of the inductive store. At 60 J, peak currents of 8437 and 17031 amps were obtained with inductances L_{s1} and L_{s2}; respectively. $_{Is}$ and η values of 1600 sec and 5% are obtained. To improve the performance of the inductively-driven PPT, Teflon mass ablation has to be increased. This can be accomplished by increasing the current density at the Teflon surface by reducing the Teflon surface width.

ACKNOWLEDGMENTS

The authors gratefully acknowledge the assistance and support of Eric Pencil in obtaining the Impulse-bit data for the advanced PPT. The authors also acknowledge the help and assistance of Luis Pinero and Glenn Bower for their efforts in designing and building the double ignition circuit. The authors acknowledges the assistance of Tomokazu Umeki in preparing this manuscript.

This work was supported by NASA Lewis Research Center, Cleveland, Ohio, under grant NAG3-843.

REFERENCES

1. H. Kamhawi, P.J. Turchi, R.J. Leiweke, and R.M. Myers, " Design and Operation of A Laboratory Bench-Mark PPT", AIAA 96-2732.

2. P.G. Mikellides and P.J. Turchi, " Modeling of Late-time Ablation in a PPT", AIAA 96-2733.

3. P.J. Turchi, R.J. Leiweke, H. Kamhawi, " Design of an Inductively-Driven Pulsed Plasma Thruster",AIAA 96-2731.

4. P.J. Turchi, "Directions for Improving PPT Performance", IEPC 97-038.

5. Haag, T.W., ' Thrust Stand for Pulsed Plasma Thrusters', Rev. Sci. Instrum. 68(5), May 1997.

6. Turchi, P.J., AAE 894 class notes, Spring 1998.

7. R.J. Leiweke, " An advanced plasma Thruster Design Study Using One-Dimensional Slug Modeling", final report for AFSOR summer research program.

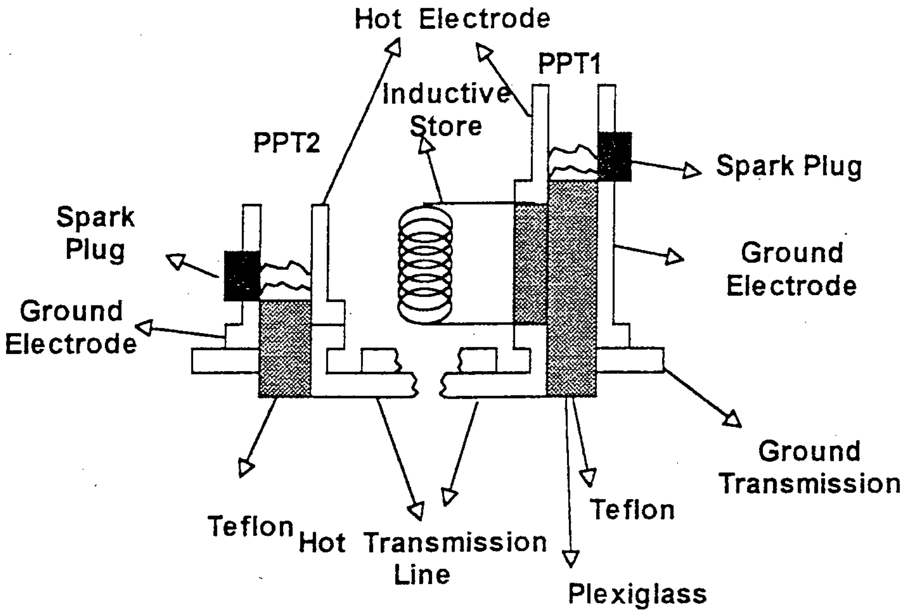

Figure 1: Configuration 1 for the inductively-driven PPT

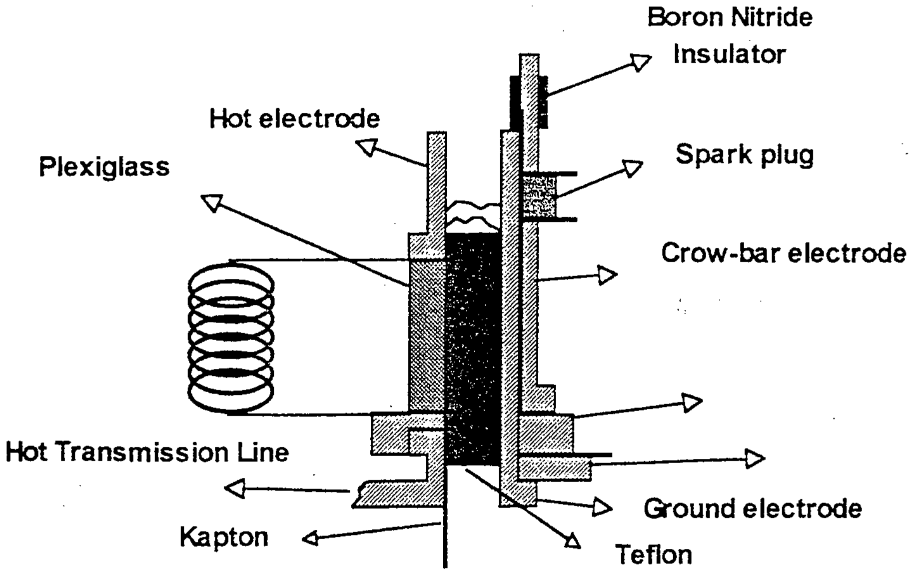

Figure 2: Configuration 2 for the inductively-driven PPT

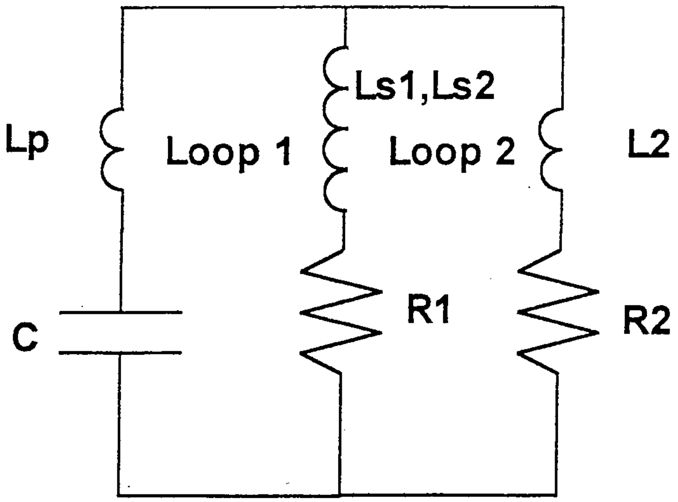

Figure 3: Schematic diagram of the inductively-Driven Pulsed Plasma Thruster.

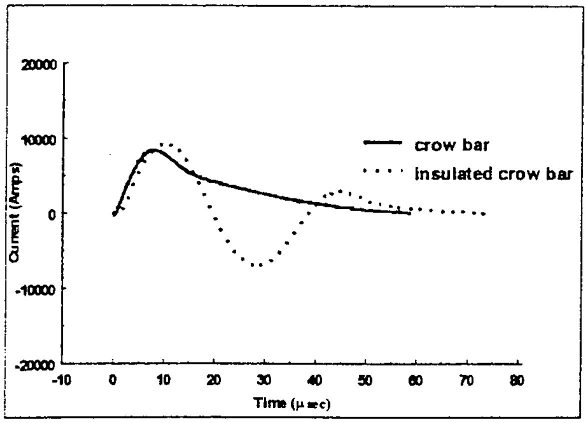

Figure 4a: Current waveforms at 60 J for L_{s1} at 1.91 cm gap.

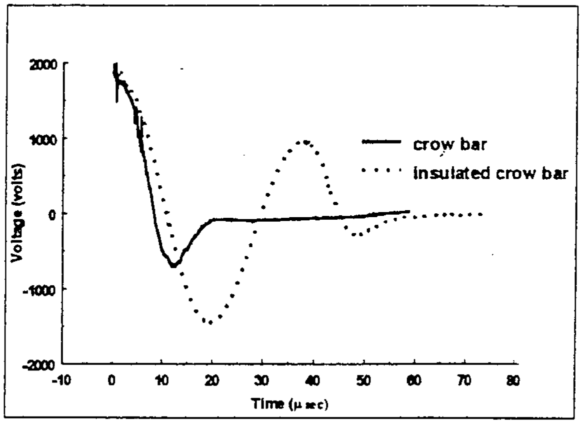

Figure 4b: Voltage waveforms at 60 J for L_{s1} at 1.91 cm gap.

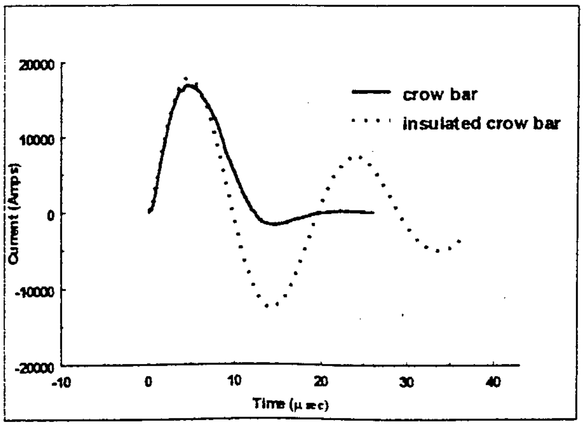

Figure 5a: Current waveforms at 60 J for L_{s2} at 1.91 cm gap.

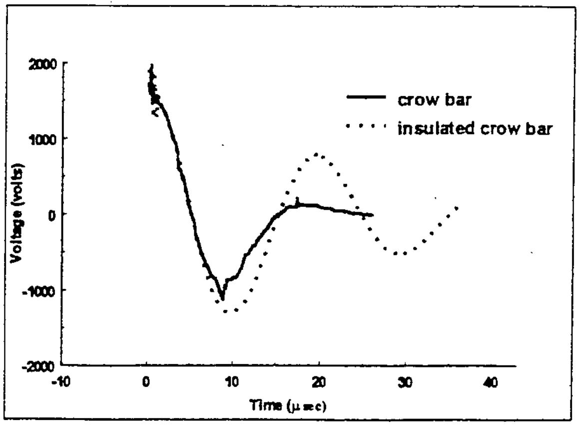

Figure 5b: Voltage waveforms at 60 J for L_{s2} at 1.91 cm gap

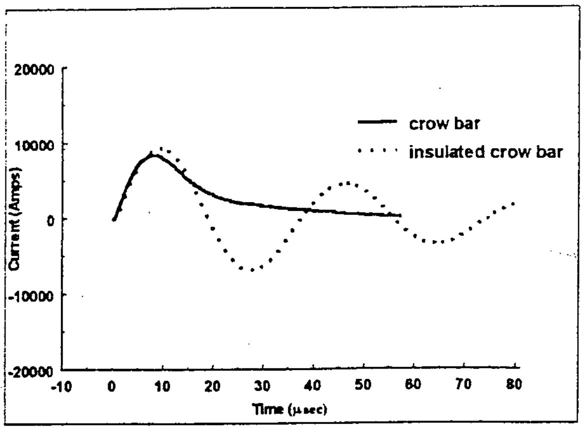

Figure 6a: Current waveforms at 60 J for L_{s1} at 2.54 cm gap.

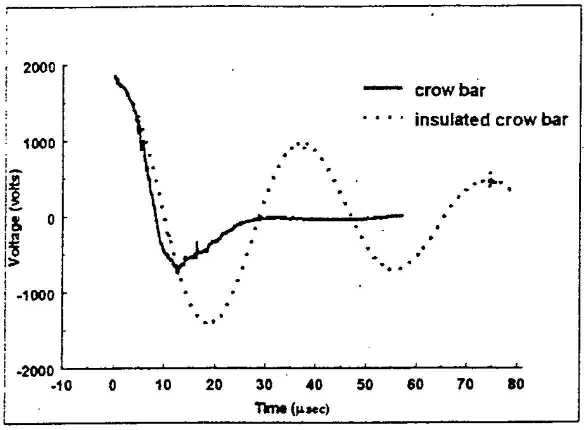

Figure 6b: Voltage waveforms at 60 J for L_{s1} at 2.54 cm gap.

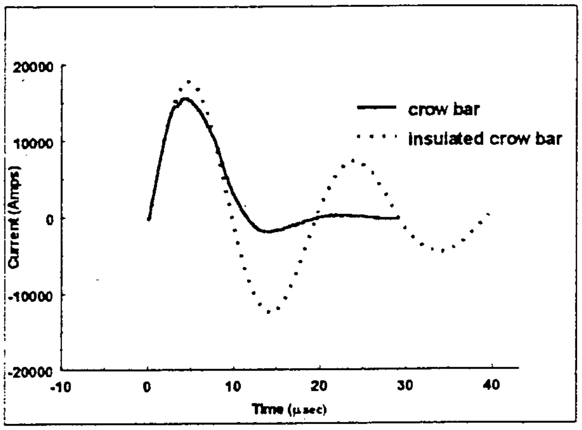

Figure 7a: Current waveforms at 60 J for L_{s2} at 2.54 cm gap.

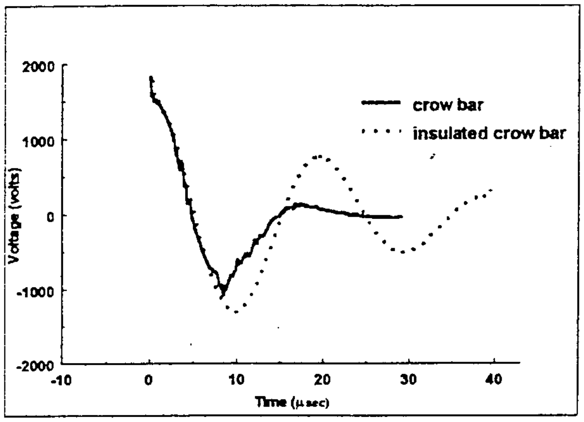

Figure 7b: Voltage waveforms at 60 J for L_{s2} at 2.54 cm gap.

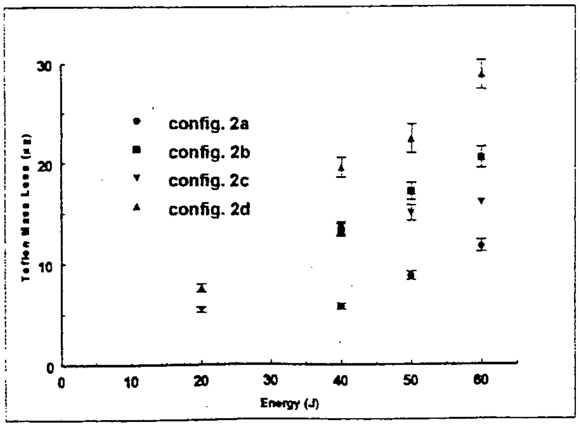

Figure 8: Mass loss data for the different configurations at the different energy levels.

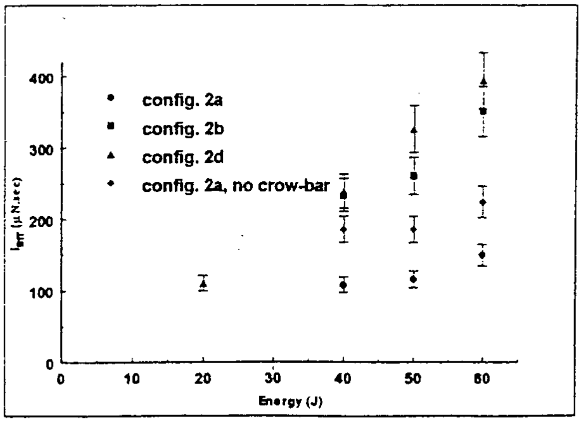

Figure 9: Impulse-bit data for the different configurations at the different energy levels.

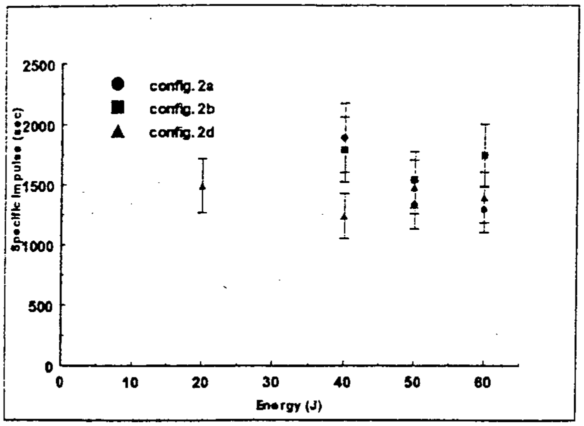

Figure 10: Specific Impulse values for the different configurations at the different energy levels.

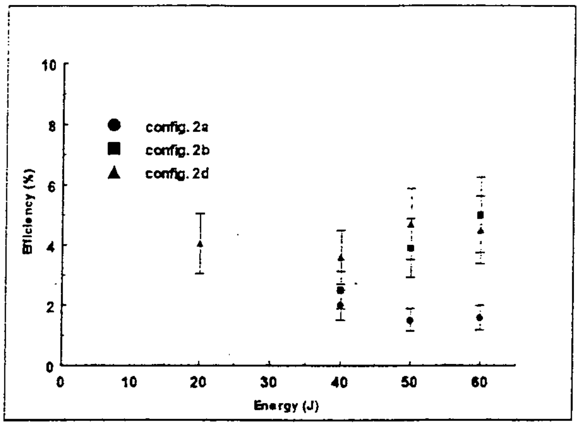

Figure 11: Thrust efficiency values for the different configurations at the different energy levels.

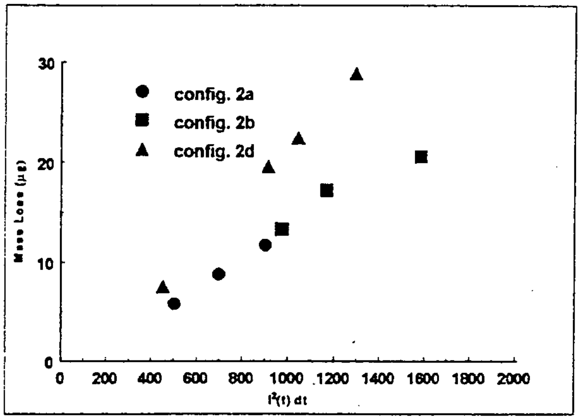

Figure 12: Mass loss vs. $\int i^2(t)\,dt$ for the different configurations at the different energy levels.

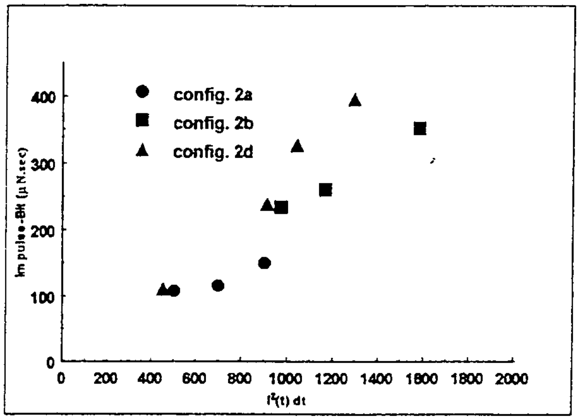

Figure 13: Impulse-bit vs. $\int i^2(t)\,dt$ for the different configurations at the different energy levels

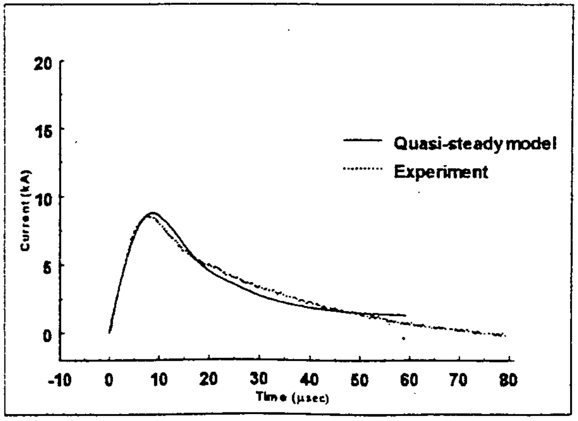

Figure 14:Experimental and numerically predicted current waveforms at 60 J for L_{s1}.

AIAA 98-3807

Theoretical Investigation of Pulsed Plasma Thrusters

P.J. Turchi, I.G. Mikellides, P.G. Mikellides
and C.S. Schmahl

The Ohio State University
Columbus, OH

34th AIAA/ASME/SAE/ASEE
Joint Propulsion Conference & Exhibit
July 13-15, 1998 / Cleveland, OH

Theoretical Investigation
of Pulsed Plasma Thrusters

P.J. Turchi, I.G Mikellides, P.G Mikellides, and C. Schmahl
The Ohio State University
Columbus, OH

Abstract

Numerical simulations of pulsed plasma thrusters with the MACH2 code have shown that the total ablated mass may be composed of ablation, late-time evaporation and liberation of Teflon polymers due to solid decomposition. The latter two contributions do not considerably add to the Impulse-bit thus degrading thruster performance. Calculations within a coaxial geometry have shown that placement of the Teflon bar in relation to the electrodes can significantly improve thrust efficiency. Transport coefficients have been upgraded to include magnetic field effects and a new two-temperature equation-of-state that includes molecular effects shows that it can provide considerable corrections to the equation-of-state model utilized in the aforementioned calculations.

Introduction

The ablation-fed pulsed plasma microthruster (PPT) has been studied empirically for over thirty years. These efforts, in conjunction with attention to engineering development, have led to successful application of PPTs on satellite station-keeping missions. Renewed interest for small satellite needs has prompted further investigation of PPT behavior in order to achieve improved performance and better insight for scaling operation to lower powers and higher exhaust speeds.

The conventional pulsed plasma thruster utilizes an arc discharge across a Teflon surface within a generally simple geometric configuration. Its system simplicity, robustness, and ability to provide small impulse bits and high specific impulse make it an attractive device for the aforementioned missions. During an intense period of experimental investigation and development in the 1960's and 70's however, the PPT had failed to operate consistently at adequate efficiencies. Although some isolated laboratory devices have displayed efficiencies of up to 50%[1,2], the PPT generally operates in the range of 2% to 12%.

One of the primary reasons for the failure to improve efficiency is the lack of complete understanding of the PPT behavior. The lack of appropriate theoretical tools has limited studies to purely empirical insights that are in turn limited by the specific geometries and operating conditions. The luxury of detailed interrogation of pertinent parameters has not here to fore been available.

This paper represents the latest efforts at the Ohio State University that utilize the magnetohydrodynamic code MACH2[3] to simulate pulsed plasma thrusters and provide improved understanding of the physics involved.

Theoretical modeling

The MACH2 code, developed by the Mission Research Corporation, along with a new solid ablation model, developed at The Ohio State University, is utilized to model the physical processes within ablation-fed Teflon pulsed plasma thruster (PPT).

MACH2 solves the time-dependent magnetohydrodynamic (MHD) equations in two dimensions. It is a single fluid, multi-temperature, time-split model that includes several radiation models, real equations of state, (SESAME tables developed and supported by the T-1 Division at Los Alamos National Laboratory), Hall effect, real viscosity effects, several models for anomalous transport, and a multi-ported circuit solver. It provides the capability of plane parallel or cylindrically symmetric simulations within complex geometries, along with an Arbitrary-Lagrangian-Eulerian adaptive mesh. The numerical methods utilized by MACH2 are also state of the art, with a combination of implicit and explicit differencing, and multigrid diffusion schemes for optimization of computational times. It has been applied to a diverse range of plasma problems with great success.

The fundamental notion utilized for the development of the ablation model is that vapor is created at the equilibrium vapor pressure based on the temperature of the solid surface, (Figure 1). This temperature is calculated by accounting for the net heat flux to the surface due to energy transfer from the local plasma (conduction, condensation) versus evaporation of the surface. The net heat flux serves as a boundary condition for a 2-dimensional diffusion equation within a semi-infinite solid. This diffusion solver utilizes a second-order accurate numerical scheme in both space and time with the option of an adaptive grid for better gradient resolution at the ablating surface. The solid surface temperature and thus the vapor temperature, is used to calculate the vapor pressure based on an appropriate Teflon vapor pressure curve.[4] MACH2 computes the velocity at the ablating boundary, as a consequence of the pressure gradient, which in turn defines a mass flow rate that can be integrated over time to provide a value of the ablated mass. Integration of the total pressure at the downstream exhausting boundary provides thrust values which are also time-integrated to yield the impulse bit.

Transport Coefficients

The Generalized Ohm's Law in MACH2 is expressed in terms of the Electric field, as follows:

$$E = E' - v \times B - \frac{\nabla p_e}{e n_e}$$

where **E'** is termed the "effective" Electric field and is the sum of the resistive and Hall contributions to the field, as follows:

$$E' = \eta \cdot J + \eta_o x_e \, \boldsymbol{J} \times \boldsymbol{b}$$

The Hall parameter ($\omega_e \tau_e$), is indicated by x_e and **b** is the unit vector in the direction of the magnetic field.

The formulation of the resistive contribution to the electric field,

$$\eta \cdot J = \eta_\perp J_\perp + \eta_\parallel J_\parallel$$

incorporates the Braginskii equations[1] for the electrical resistivity tensor (see Appendix I), which are expressed in a magnetic field frame of reference.

The strong influence of the magnetic field on the flow of heat, in a two-temperature magnetoplasma is captured in MACH2, by appropriate formulas for the ion and electron thermal conductivities, first derived by Braginskii[1] (see Appendix I). In the absence of the thermoelectric effect or current density, the heat flux vector is given by,

$$\boldsymbol{q} = \boldsymbol{q}_\perp + \boldsymbol{q}_\parallel$$

For the two-temperature plasma each flux vector is expressed as,

$$\textit{Electron fluid:} \quad \boldsymbol{q}^e = -\kappa_\parallel^{\,e} \nabla_\parallel T_e - \kappa_\perp^{\,e} \nabla_\perp T_e$$

$$\textit{Ion fluid:} \quad \boldsymbol{q}^i = -\kappa_\parallel^{\,i} \nabla_\parallel T_i - \kappa_\perp^{\,i} \nabla_\perp T_i$$

Rectangular Geometry Simulations

Simulations of the LES-6[5,6] Pulsed Plasma thruster have been undertaken. The geometry and simulation set-up are shown in Figure 1. The upgraded MACH2 calculations confirm previous insights[7] of the possible magnitudes of late-time evaporation. The solid Teflon's temperature is elevated through the repeated applications of the microsecond pulses. Based on that temperature the propellant has the opportunity to evaporate during pulse intervals. Figure 2 shows the relative magnitude of the ablated mass during pulse time - that can be potentially electromagnetically accelerated - and the total mass loss when late-time evaporation is taken into account. In turn this post-pulse mass loss does not contribute to the Impulse-bit - as implied by the reasonable agreement of the theoretical and experimental Impulse-bit values (Figure 2) - and thus degrades efficiency. Figure 3 shows the dependance of this late-time mass loss on the chosen base temperature from the solid Teflon. These values have been calculated via an extrapolation of the mass loss history as calculated by the ablation model.

The capability of solving the diffusion equation as part of the ablation model provides the 2-dimensional temperature distribution within the solid Teflon as a function of time. Figure 4 shows the intrusion of the heat pulse via the temperature profile in the middle of the height-wise direction at three different times. This allows for further insights into other phase transitions before vaporization.

One of these major transitions is solid decomposition (or "melting") during which the teflon solid decomposes into the long polymer chains. These macroparticles might behave as liquids, but with very high viscosity. This in turn suggests that such groups of polymer chains are quite slow moving and could be introduced in the discharge chamber much later than the current pulse duration. Decomposition typically occurs at 600K (327C)[4]. The temperature distribution at 0.4 μsec (peak current) suggests that a considerable amount of the solid propellant exceeds this value. Specifically, this depth is 0.07 microns which translates to about 45 micrograms of propellant having the opportunity to decompose. The percentage of this value that has the opportunity to be liberated into the discharge chamber is a function of viscosity and heat conduction, which probably governs the rate at which these polymers condense back into the solid.

Coaxial Geometry Simulations

Close comparison of experimental data and theoretical modeling of the PPT in its traditional rectangular configuration is severely hampered by three-dimensional effects. Optical measurements cannot use Abel inversion techniques, and theoretical calculations, even with state-of-the-art computer codes are simply inadequate. This situation has prompted us to focus on PPTs in coaxial geometry, in hopes of avoiding the complexities of 3-d effects.

The 2-dimensional, axisymmetric code, MACH2, has been used to carry out simulations of a cylindrical geometry with dimensions and energy levels similar to those of the LES-6 thruster, as indicated in Figure 5.

Results indicate proper capturing of the coaxial thruster's overall electromagnetic behavior as indicated by Figure 6 and Figures 9-12. The monotonic variation of impulse bit with magnetic pressure is also captured in Comparisons with results from previous simulations on the LES-6 thruster[2], indicate (~54%) higher peak currents with (~28%) lower rise times associated with the coaxial PPT, which can be attributed to the lower effective impedance as material is accelerated at lower speeds. The impulse bit for the case of a full Teflon piece across the electrode gap is found to be 16 μN-sec. This is 51% lower than the value calculated in simulations of the rectangular configuration (of the same inner electrode gap). The expected ratio (based on peak currents) indicates:

$$\frac{I_{bit,\,rec}}{I_{bit,\,coax}} \propto \frac{4\pi[h/2d]}{[\ln(Ra/Rc)+3/4]}\,\frac{J_{peak,\,rec}^{2}}{J_{peak,coax}^{2}} = 1.5$$

The anode to cathode radius ratio, Ra/Rc, for the coaxial geometry is 7 and the height to width ratio, h/d, for the LES-6 thruster was 3. The total mass exhausted is found to be 36% higher in the coaxial configuration.

Performance Improvements

One of the potential advantages of a coaxial PPT configuration, as found in this effort, is the proportionality of the current density in the discharge, with the inverse of the radial position, r. When combined with a suitable placement of a shorter Teflon piece at the inner electrode gap, the expected ~1/r^2 variation of the heat flux at the surface of the solid propellant, offers the opportunity of regulating the ablated mass. It should be noted that such a variation is not available in the rectangular arrangement, as seen in Figure 7.The thrust efficiency however, exhibits minimal improvements (8 to 10%) due to the fact that absorption of elevated heat fluxes (near the cathode), by a narrower solid, results in temperatures much higher than the ablation limit and therefore the release of mass from the surface continues, for periods longer than those associated with the current pulse.

Considerable improvements are found when the propellant outer radius is at the anode position and in particular, when the gap to propellant area ratio is between 1-1.3. Such an arrangement minimizes wasteful release of propellant mass, due to high heat fluxes near the cathode and couples the complicated processes of ablation and electromagnetic acceleration most efficiently. The abrupt drop of efficiency for gap to electrode area ratios higher than 1.5 is attributed to reasons similar to those for the case of small outer to inner radius propellant pieces near the cathode.

Concluding Remarks

MACH2 simulations of the LES-6 rectangular PPT have shown that there could be two major mass-loss contributions that degrade performance. Late time evaporation and solid Teflon decomposition may be a major portion of the total mass that does not contribute to the impulse bit.

Numerical analysis on a coaxial, pulsed plasma microthruster has shown significant performance improvements with increasing gap to propellant area ratio and with the Teflon piece adjoining the anode. Thrust efficiency was found to be as high as 30% when the propellant area, exposed to the discharge, was 3/4 of the electrode gap area. These findings require further theoretical investigation and experimental verification.

A new Teflon equation-of-state has been developed at Ohio State University. It is based on a two-temperature (electron and heavy-particle), local thermodynamic equilibrium of 25 different species. While this formulation agrees well with others in regions of common parameter values, it disagrees significantly with the results from SESAME (used in conjunction with its related routine 'eospac'). These discrepancies may interfere with detailed analyses that have been performed to date. It is possible, however, that much of the behavior of the PPT is governed by overarching principles. For example, the mass flow may be controlled by a magnetosonic condition downstream of the discharge. Temperature gradients and plasma conditions near the Teflon surface would then adjust to satisfy a choking condition, regardless of the detailed physics and chemistry of the local plasma composition.

References

1. Guman, W. and Palumbo, D.J., "Effects of Propellant and Electrode Geometry on Pulsed Ablative Plasma Thruster Performance," AIAA 75-409, 11th Electric Propulsion Conference, New Orleans, LA, 1975.

2. Myers, R.M., "Electromagnetic Propulsion for Spacecraft," AIAA 93-1086, Aerospace Design Conference, Irvine, CA, 1993.

3. Peterkin, R.E. Jr., Giancola, A.J., Frese, M.H. and Buff, J., "MACH2: A Reference Manual-Fourth Edition," Mission Research Corporation, 1989.

4. Wentink, T., Jr., "High Temperature Behavior of Teflon," AVCO-EVERETT Research Laboratory, Contract No. AF 04(647)-278, July 1959.

5. Vondra, R.J., Thomassen, K. and Solbes, A., "Analysis of Solid Teflon Pulsed Plasma Thruster", *Journal of Spacecraft and Rockets,* Vol. 7, No 12, Dec. 1970, pp. 1402-1406.

6. Solbes, A. and Vondra, R.J., "Performance Study of a Solid Fuel-Pulsed Electric Microthruster," *Journal of Spacecraft and Rockets,* Vol. 10, No 6, June 1973, pp 406-410.

7. Mikellides, P.G. and Turchi P.J. "Modeling of Late-time Ablation in Pulsed Plasma Thrusters", AIAA-

8. Braginskii, S. I. (1965). *Reviews of Plasma Physics*, Vol. 1, pp. 205-311 (ed. M. A. Leontovich). Consultants Bureau, New York.

9. Turchi, P.J., "Directions for Improving PPT Performance," IEPC Paper 97-038. ***Proceedings of the 25th International Electric Propulsion Conference***. Electric Rocket Propulsion Society, 1998. Volume 1.

APPENDIX I

The formulae for resistivity and thermal conductivity, implemented in this effort, were first derived by S.I. Braginskii (1965) and are based on approximate solutions of the two-component Fokker-Planck equations. They are given below as follows:

Resistivity.

$$\eta_{\parallel} = \eta_o \alpha_o \qquad \eta_{\perp} = \eta_o \left[1 - \frac{\bar{\alpha}_1 x_e^{\,2} + \bar{\alpha}_o}{x_e^{\,4} + \delta_1 x_e^{\,2} + \delta_0} \right]$$

$$\eta_o \equiv \frac{m_e}{e^2 n_e \tau_e}$$

Electron-fluid Thermal Conductivity.

$$\kappa_{\parallel}^{\,e} = \kappa_0^{\,e} \gamma_0 \qquad \kappa_{\perp}^{\,e} = \kappa_0^{\,e} \frac{\gamma'_1 x_e^{\,2} + \gamma'_0}{x_e^{\,4} + \delta_1 x_e^{\,2} + \delta_0}$$

$$\kappa_0^{\,e} \equiv \frac{k}{m_e} p_e \tau_e$$

Ion-fluid Thermal Conductivity.

$$\kappa_{\parallel}{}^{i} = \kappa_0{}^{i} 3.91 \qquad \kappa_{\perp}{}^{i} = \kappa_0{}^{i} \frac{2x_i^2 + 2.65}{x_i^4 + 2.7x_i^2 + 0.677}$$

$$\kappa_0{}^{i} \equiv \frac{k}{m_i} p_i \tau_i$$

In all equations above, τ_e and τ_i are the electron and ion collision times, respectively. All polynomial coefficients can be found in Reference 8.

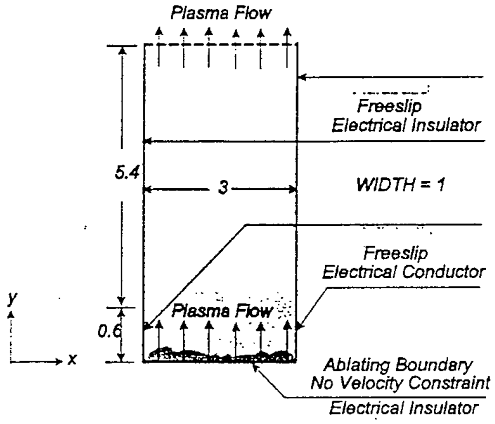

Figure 1. The MACH2 modeling of the LES-6 geometry. Dimensions in cm.

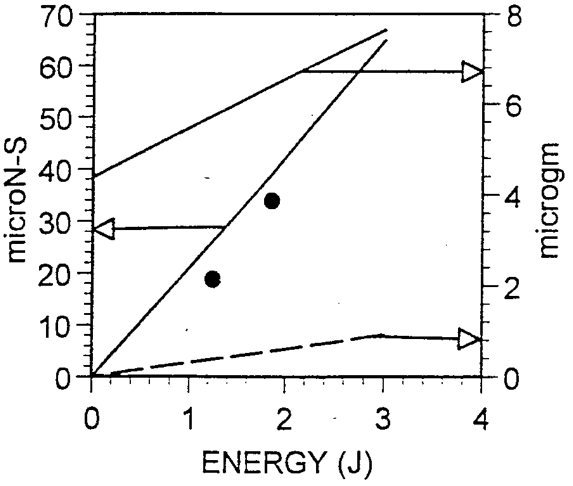

Figure 2. MACH2 calculated Impulse-bit (solid line) is compared to LES-6 experimental data (solid symbols). Calculation of the ablated mass (dashed line) is compared to the mass loss that includes late-time evaporation (solid line).

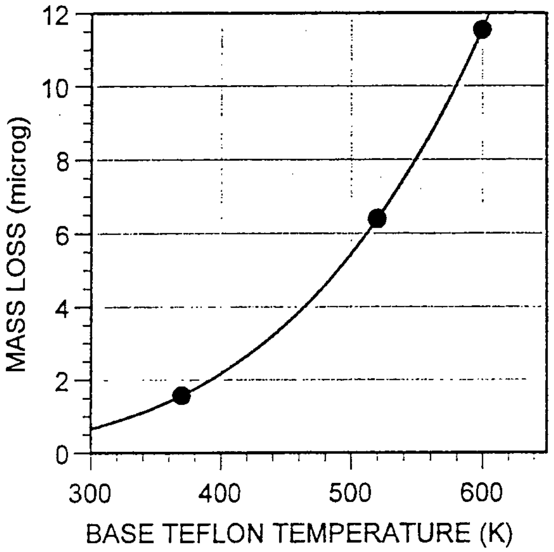

Figure 3. MACH2 calculated mass loss due to ablation and late-time evaporation as a function of propellant base temperature.

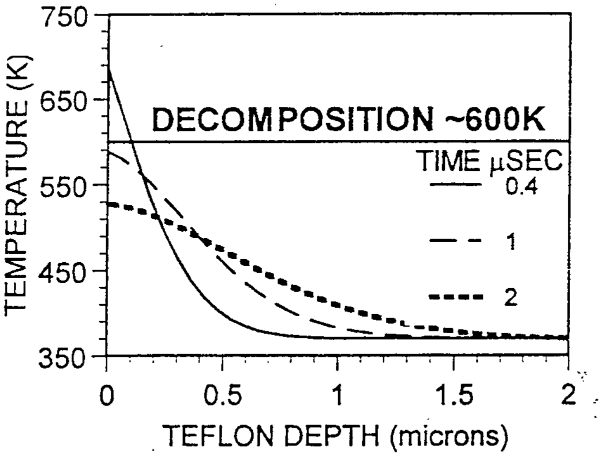

Figure 4. Solid propellant temperature profiles at different times during the LES-6 pulse duration.

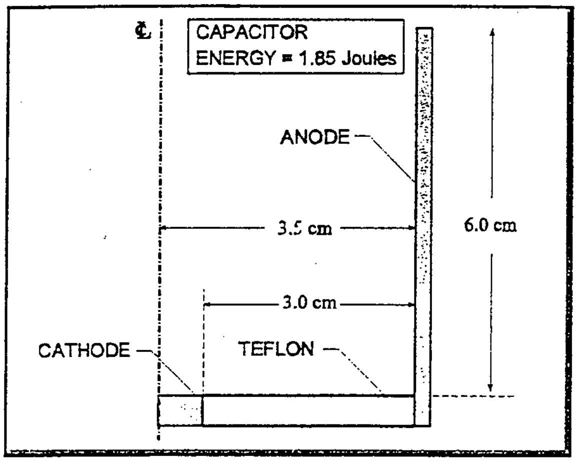

Figure 5. Arrangement used in simulations of a coaxial PPT.

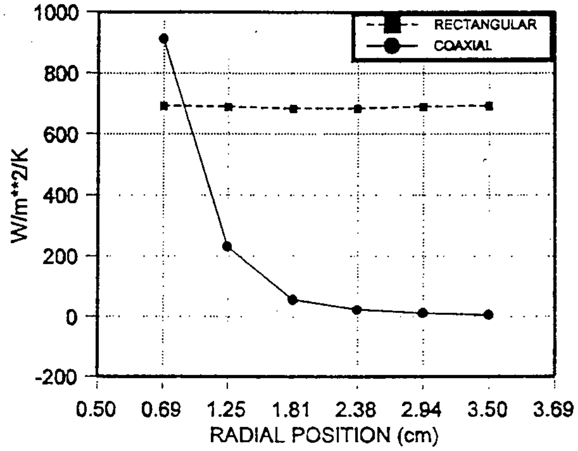

Figure 7. Heat flux into the Teflon surface for the coaxial and rectangular geometries, as calculated by MACH2.

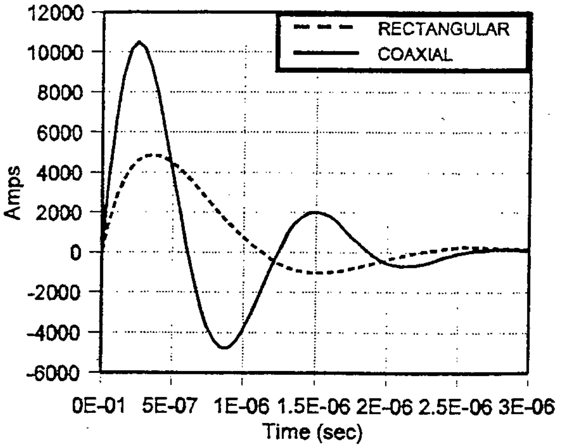

Figure 6. Current pulses for the coaxial and rectangular geometries, as calculated by MACH2.

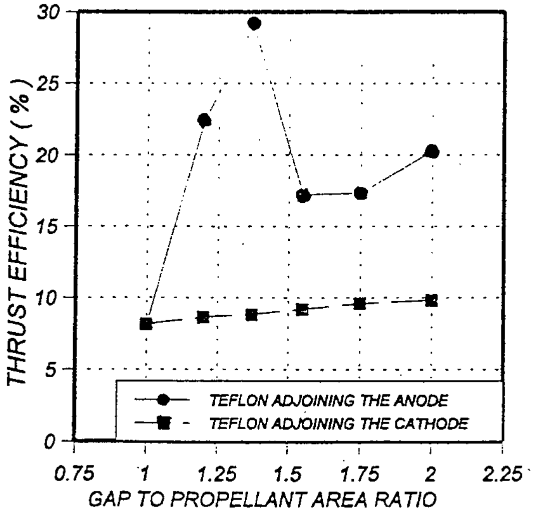

Figure 8. Performance dependence of the coaxial PPT on gap to propellant area ratio.

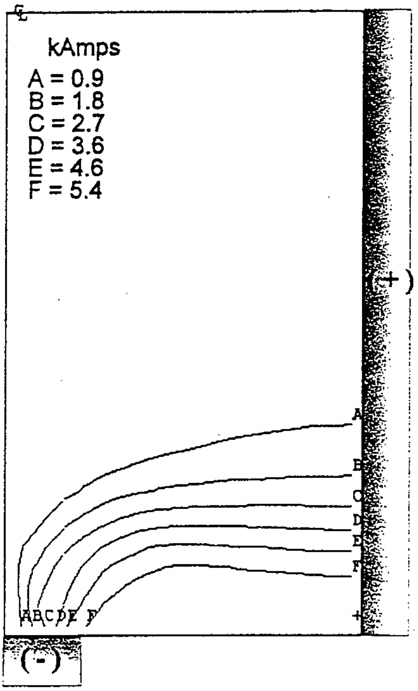

Figure 9. Current contours, time = 0.45 microsecs.

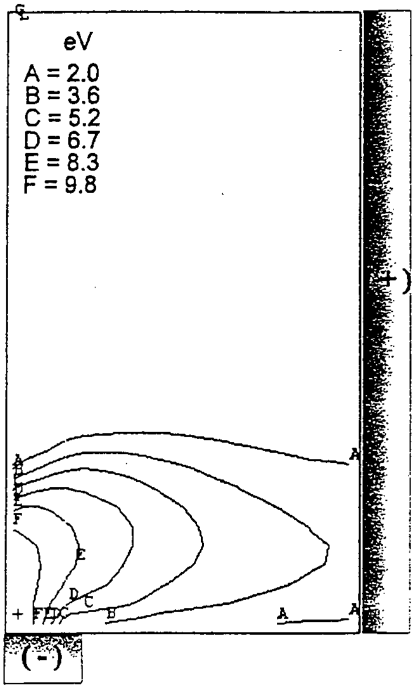

Figure 11. Temperature contours, time = 0.45 microsecs.

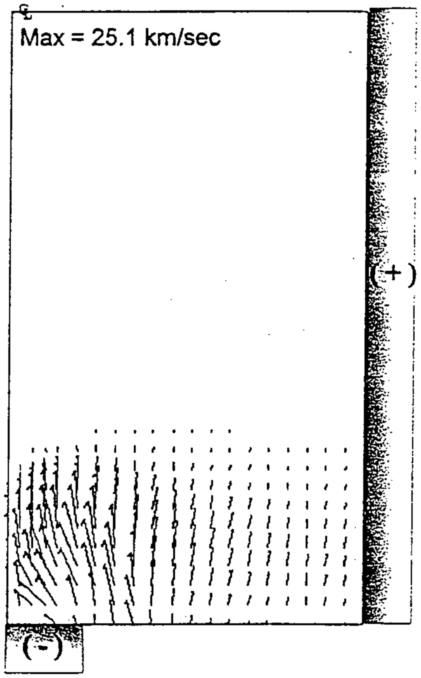

Figure 10. Velocity vectors, time = 0.45 microsecs.

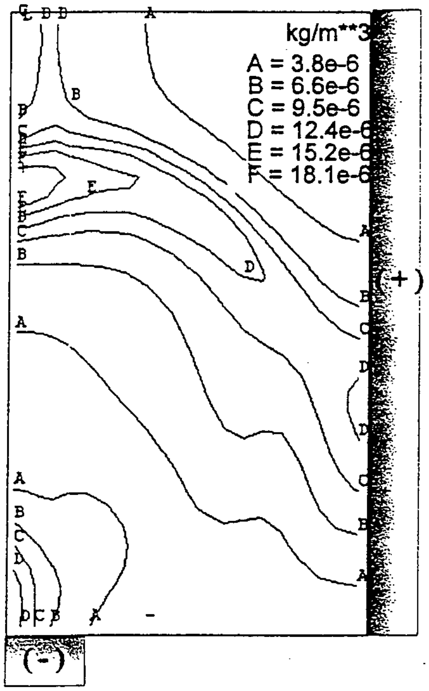

Figure 12. Density contours, time = 1.8 microsecs

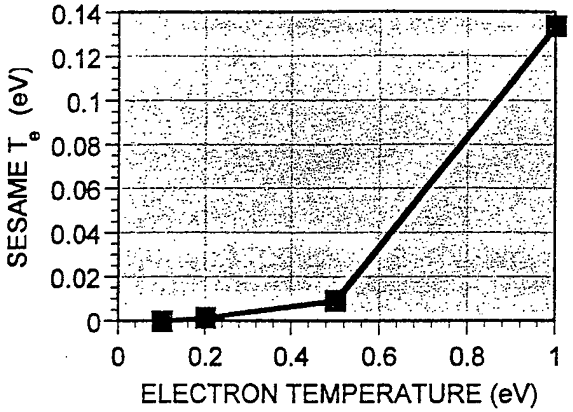

Figure 14. SESAME/EOSPAC predicted electron temperature as compared to the OSU-EOS electron temperature at the same energy densities.

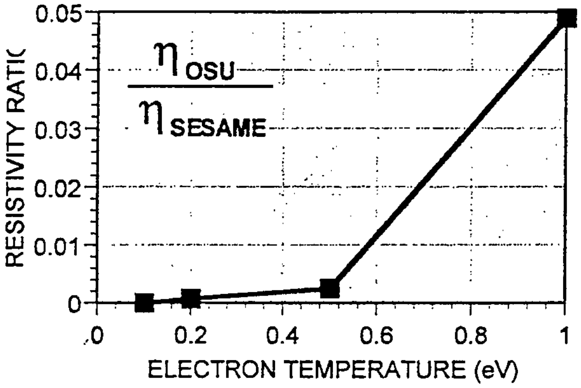

Figure 15. Resistivity ratio as predicted by the two EOS models as a function of electron temperature.

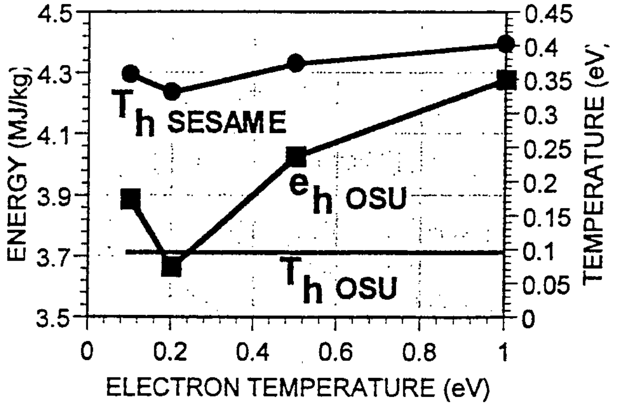

Figure 16. Heavy particle specific internal energy and temperature comparisons of the two EOS models.

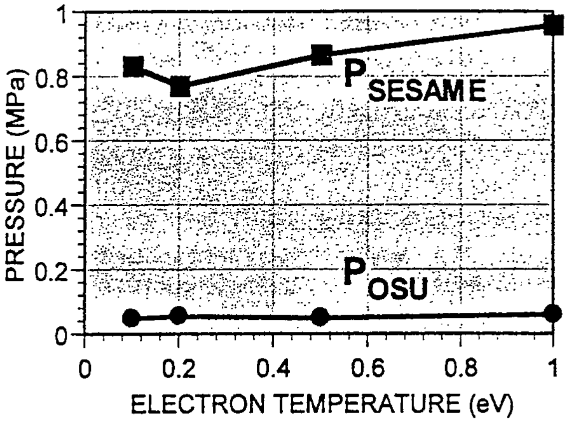

Figure 13. Total pressure comparisons of the two EOS models as a function of electron temperature.

IEPC 99-211

Optimization of Pulsed Plasma Thrusters in Rectangular and Coaxial Geometries

I.G. Mikellides and P.J. Turchi
The Ohio State University
Columbus, Ohio

26th International Electric Propulsion Conference
October 17-21, 1999, Kitakyushu, Japan

OPTIMIZATION OF PULSED PLASMA THRUSTERS IN RECTANGULAR AND COAXIAL GEOMETRIES

I.G. Mikellides and P.J. Turchi
The Ohio State University
Columbus, Ohio USA

ABSTRACT

Theoretical modeling of PPT behavior in rectangular and coaxial configurations has led to new insights that permit optimization of performance for microsatellite needs. It is found that the total expelled mass is due to ablation during the discharge and solid decomposition that persists long after the pulse. This latter mass does not considerably contribute to the impulse-bit and thus degrades thruster performance. For the rectangular PPT geometry, numerical simulations provide the optimizing combinations of current waveforms and channel widths that utilize all decomposed mass electromagnetically. Idealized analytical modeling shows that the mass flow rate varies linearly with the square of the magnetic field and that the downstream flow speed becomes magnetosonic, in the limit of low beta. Comparison with numerical results confirms these findings and further reveals that the downstream flow is predominately doubly ionized. The mass flow requirement for such magnetosonic flow in turn, determines the surface temperature of the solid propellant. In coaxial arrangements, numerical modeling indicates that in comparison to rectangular, annular and linear pinch geometries, only an arrangement that operates an inverse-pinch discharge offers the convenience of axisymmetry, and operation at energy levels anticipated for microsatellite propulsion with propellant temperatures never exceeding the decomposition limit.

INTRODUCTION

Simplicity, robustness and ability to operate in pulses at low average power have allowed selection of pulsed plasma microthrusters (PPTs)[1] for microsatellite applications, even though their thrust efficiency have historically been very poor. The lack of appropriate theoretical tools during the early investigation of these devices did not offer the opportunity for interrogating all pertinent parameters during pulsed operation thus inhibiting efforts to improve thruster performance. ②

The PPT, while simple in its embodiment, incorporates considerable complexity, as suggested by Fig. 1. An arc discharge heats a solid propellant and provides a gradient of magnetic pressure that accelerates the ablated material. The diffusion of heat from the discharge into the propellant slab causes decomposition of material, a portion of which is accelerated electromagnetically to high speeds (> 10 km/s) while the remaining decomposed mass travels at much lower speeds (< 1 km/s) and contributes minimally to the thrust. By identifying and quantifying such mechanisms, optimization of thruster performance may be achieved.

MODELING IN RECTANGULAR GEOMETRY

Numerical simulations and optimizing waveforms. The unsteady, 2½-dimensional, magnetohydrodynamic code, MACH2[2] has been successfully employed to model PPTs[3,4]. For example, results from simulating the LES-6[1] thruster captured well the experimental magnitude and trends of the impulse-bit. Further modeling showed that the computed mass of ablated propellant (all of which participated in electromagnetic acceleration in these calculations), is much less than the experimental value for mass loss per shot (~10 μg at a stored energy of 1.85 J).

The discrepancy in mass loss may result from two processes: late-time evaporation (between discharges) and solid decomposition. The first depends largely on the base temperature of the propellant slab which, if elevated, may result in a substantial amount of late mass loss[3]. Thermocouple measurements in experiments[5] at 40 J/pulse and a repetition rate of 1Hz, indicate a base temperature of 370K. At this lower temperature value, evaporation between pulses contributes a negligible fraction to the total mass loss. The second process becomes evident upon closer interrogation of the computed temperature profile within the solid. It is observed that a significant portion of the propellant has been heated above the decomposition limit or the so-called "melting" point of Teflon (Fig. 2), normally taken as 600K[6]. At this value, Teflon begins to soften as it transforms into a "slurry" of high density vapor and solid particles (rather than a true homogeneous, liquid state). In the PPT, the exact conditions and amount of products released during this phase transition are uncertain. For example, the depth of solid propellant above 600K implies an amount that greatly exceeds the experimentally measured mass loss at the 1.85J level (see Fig. 3). For consistency of evaluation of the effects

---

of propellant heating, we have therefore chosen a value of decomposition temperature of 673K in order to agree with the mass loss in the LES-6.

The qualitative profiles depicted in Fig. 4 suggest that sufficiently long pulse times will assure participation of all the available decomposed mass in the electromagnetic acceleration process. Fig. 4 (left) depicts a situation where a steady-state discharge is sustained along the constant-area channel. For constant current, the mass of material required to sustain the steady-state position of the discharge increases linearly with time. The heat flux from the plasma diffuses into the solid to a depth that increases linearly with the square root of time. The fraction of mass within this depth that is above the decomposition temperature, has the opportunity to decompose without the benefit of electromagnetic acceleration, if the current is terminated before the curves intersect. The results from the LES-6 simulations indicate that the traditional oscillatory waveform operates at pulse times that are much shorter than needed for efficient utilization of all decomposed mass (see Fig. 3).

Numerical estimates using ideal, constant-current waveforms indicate that pulse times must exceed a few hundred microseconds to achieve optimum propellant utilization[7]. Conventional circuitry aboard power-limited microspacecrafts will not permit such pulse times. Use of inductive energy-storage circuitry[8] can provide discharge durations of 10-50 μsecs at initial capacitor energies of 50J or less. With such circuitry, it is possible to generate a current pulse that is not constant, and for which the depth of material needed by the discharge would eventually converge with that created by the diffusion of heat into the solid (see Fig. 4, right), resulting in better propellant utilization.

For initial optimization surveys with MACH2, inductive-circuit waveforms have been simulated by typical LC current rises, followed by L/R decays. Combinations of two current waveforms and two widths of thruster channel (Fig. 5) provide four different values of the magnetic field at the surface, B_o. The optimization is displayed in Fig. 6, in terms of a ratio of depths for the two processes of electromagnetic acceleration and solid decomposition. This depth ratio indicates the proportion of total decomposed mass to that used for electromagnetic acceleration and thus decrease of this ratio toward unity implies efficient mass utilization.

Idealized Model. In order to isolate the determinant parameters during mass evolution in a PPT, an idealized model may be formulated by assuming quasi-steady flow in a one-dimensional, MHD channel. In the limits of high magnetic Reynolds number and low beta, magnetohydrodynamic flow into a field-free vacuum implies the existence of a magnetosonic condition in the channel,

$$u^* = V_A^* \equiv \frac{B^*}{\sqrt{\mu \rho^*}} \qquad (1)$$

where, u denotes the flow speed and V_A, is the local value of the Alfven wave speed. In equation (1) above, ρ is the mass density, B is the magnetic field and starred quantities refer to magnetosonic values. For a discharge current J, and rectangular channel width d, the magnetic field at the propellant surface is,

$$B_o = \frac{\mu J}{d} \qquad (2)$$

Upon integration of the conservation equations, from the surface to the magnetosonic point we obtain,

$$w \equiv \rho^* u^* \qquad (3)$$

$w \cdot \dot{m}/A$

$$w u^* = \frac{B_o^2 - B^{*2}}{2\mu} \qquad (4)$$

$$w h_o + \frac{E B_o}{\mu} = w\left(h^* + \frac{u^{*2}}{2}\right) + \frac{E B^*}{\mu} \qquad (5)$$

where E, is the electric field (assumed to be constant), and h, denotes the specific enthalpy.

Substitution of equations (1) and (3) into (4) gives the proportionality between the magnetic fields at the surface and magnetosonic locations as,

$$B^* = \frac{B_o}{\sqrt{3}} \qquad (6)$$

and combined with equations (3) and (5) yields the magnetosonic flow speed,

$$u^* = \sqrt{\frac{\Delta h}{\sqrt{3} - 1.5}}\ ; \qquad \Delta h \equiv h^* - h_o \qquad (7)$$

If the specific energy needed for ionization dominates the change in flow enthalpy, Δh, then u^* tends to remain fixed and proportional to the Alfven critical speed,

$$u_{cru} = \sqrt{2 \Delta h} \qquad (8)$$

At fixed u*, the magnetic pressure difference from the propellant surface to the location of the magnetosonic point, $(B_o^2 - B^{*2})/2\mu$, defines the mass flow rate per unit area, w (equation 4). The current and channel width thus prescribe the mass flow per unit area at the propellant surface that must be provided by ablation.

Adjacent to the propellant surface, the mass flow rate per unit area is limited by a choking condition, based on the usual (thermal) sound speed. For a heated, calorically perfect flow, with a stagnation pressure

$c_p, c_v = const$

proportional to the equilibrium vapor pressure of the propellant, this condition only depends on the surface temperature[7], T_s. The surface temperature, in turn, scales the temperature profile in the solid propellant.

By prescribing ideal current waveforms in MACH2 (similar to that shown in Fig. 4, left) the principal elements of the model may be checked. Three test cases of current amplitude J=4, 5 and 7 kAmps, and a channel width of d=1cm were attempted. Computed evolution of pertinent variables showed that indeed steady-state operation is achieved within three microseconds[9], (a few times the current rise time used here). Fig. 7 verifies that the magnetosonic condition is attained in all three test cases near the thruster exit. For further comparisons, these test simulations are extended to higher J/d values and results are shown in Fig. 8 and Table 1. Assuming a singly ionized plasma at the magnetosonic point, equations (7) and (8) give the magnetosonic speed as approximately one half the value computed by MACH2. Conversely, equation (4) predicts the mass flow rate per unit area to be approximately twice as high the value determined by MACH2 The discrepancy is due to a higher degree of ionization at the magnetosonic location as suggested by Fig. 8 and the last two columns of Table 1. Assuming doubly ionized plasma, the analytical values are all within 8% of the corresponding values from MACH2. The value of Δh, as determined by MACH2 includes all molecular modes of energy (including dissociation) and is also used for comparison. The agreement with the analytical model verifies the linear dependance of the mass flow on B_o^2 and further confirms that the gas is approximately doubly ionized at the magnetosonic location. The magnetosonic speed predicted by MACH2 and the analytical model (~35 km/sec) correlates well with values of doubly ionized particle speeds measured in the plume of various PPTs.

(2)

This is actually a result of MACH2 in 1 pt. i.e. it happens @ a point 0.6 cm away from the prop surface (total length is 1 cm)

MODELING IN COAXIAL GEOMETRY

Close comparison of experimental data and theoretical modeling of the PPT in its traditional rectangular configuration is severely hampered by three-dimensional effects. Optical measurements cannot use Abel inversion techniques, and theoretical calculations, even with state-of-the-art computer codes are simply inadequate. We are therefore prompted to focus on PPTs in coaxial geometry.

(2)

Annular and linear pinch configurations. Two coaxial PPT configurations are depicted in Figures 9 and 10. Both were simulated by MACH2 using a prescribed current pulse with a maximum magnetic field of about 10T based on a fast rising, slowly decaying waveform that peaked at 50 kAmps. Pulse decay time, exposed propellant area and peak current were varied during these simulations, in order to quantify their effect on the utilization of mass during the acceleration process[7].

In the annular configuration of Fig. 9 it is found that improvements in the mass ratio are possible with prolonged pulses but in a manner that is inversely proportional to the square root of the pulse decay time. For a typical waveform of 30 μsec pulse time, with the amount of decomposed mass still approximately two orders of magnitude higher than the amount accelerated (Fig. 11), it is apparent that only millisecond pulses can eliminate the wasteful release of mass due to propellant decomposition. Such times are not attainable by power source requirements typical for microsatellite applications. In contrast to the rectangular PPT, the principal difficulty with a coaxial PPT in this simple annular arrangement is the decrease in magnetic field with radius over the propellant surface. As the propellant is utilized efficiently by the optimizing magnetic field near the center conductor, the propellant at larger radii is not used properly.

In an attempt to eliminate the added complexities of magnetic field variation with radius, a linear pinch geometry (Fig. 10) has also been pursued, under conditions similar to those implemented in the annular geometry. As illustrated by the typical case in Fig. 11, the linear pinch configuration offers significant improvement over its annular counterpart but the amount of decomposed mass is still almost ten times higher than the amount accelerated electromagnetically. The impediment here is the decrease in area available for current conduction due to a required reduction in radius for microsatellite applications. The consequence is a rapid increase of resistive heating within the discharge chamber that results in elevated propellant temperatures and increased depths of propellant available for decomposition. Under such conditions, the linear pinch is characterized by a low magnetic Reynolds number, high-beta flow and operates more like an electrothermal thruster. Similarly to the annular configuration, increasing pulse decay times and maximum magnetic field both reduce the mass ratio but in a manner that is not feasible for microsatellite applications. An increased propellant length to radius results in a higher mass ratio due to the elevated temperatures of the stagnant plasma near the cathode.

(2)

Inverse pinch configuration. The restrictions associated with the two previous configurations lead to the inverse pinch geometry in Fig. 12. Here, current flow between the electrodes creates an electromagnetic force on the plasma that is directed radially outward; the magnetic field remains uniform along the ablating boundary. The plasma is unconfined (contrary to the linear pinch) as it expands freely to a downstream magnetosonic condition, under the influence of the magnetic pressure gradient. A radially inward force $B^2/\mu r$, the so-called magnetic tension, tends to offset the radial expansion.

As a consequence, the mass flow per unit area in this arrangement is found about two orders of magnitude lower than in the rectangular geometry and the surface temperature is more than one hundred degrees lower (Fig. 13). This suggests that contrary to all previous geometries studied here, only the inverse pinch configuration offers the convenience of axisymmetry for better correlating experiment and theory, and the opportunity for operation at relatively high magnetic fields with solid-propellant temperatures below the effective decomposition limit.

In an effort to provide preliminary design guidelines an assessment of this configuration is attempted using critically-damped current waveforms. With an outer propellant radius of 1cm, the typical waveforms of Fig. 14 provide a maximum magnetic field of approximately 0.4T near the ablating boundary. The MACH2 simulations indicate that the surface temperature does not exceed the effective decomposition temperature for the shorter pulse ("current waveform-1"), but does so for the prolonged pulse ("current waveform-2"). Closer inspection of the temperature profiles in Fig. 14 reveals that the solid responds with an increase in temperature during the latter times of the current decay. Fig. 15 shows the variation of the steady-state surface temperature with magnetic field, as a result of additional simulations carried out in the same geometry (1cm-radius). In the range of 0.2 to 0.5T, the depicted increase in surface temperature with decreasing magnetic field, suggests that the solid is subject to higher net heating from the adjacent plasma. In this range, as the magnetic field is reduced, the magnetic pressure decreases relative to the kinetic pressure and the flow can no longer convect heat away from the propellant surface at a sufficiently high rate. Conversely, as the field is raised to values greater than ~0.5T, the increasing magnetic pressure demands a higher mass flow rate from the propellant, subsequently forcing a rise in the surface temperature despite the modest increase in convective cooling that is provided by the electromagnetic force. Finally, for values less than ~0.2T reduction of the field yields a decrease in propellant temperature because the plasma itself is only moderately heated by the discharge.

CONCLUSIONS

Optimization of the PPT begins with specification of the propellant in terms of its Alfven critical speed and then continues by design of the thruster and propellant size to match the current waveform. The latter match demands consideration of the propellant properties, and may obtain guidance from idealized models but detailed design, requires computational tools, such as MACH2. The insights and methods discussed in the present work expand the opportunities for new PPT systems, in both rectangular and coaxial arrangements.

ACKNOWLEDGEMENTS

The authors acknowledge the support of the NASA Glenn Research Center, the Air Force Office of Scientific Research, and the Ohio Supercomputer Center.

REFERENCES

1. Vondra, R.J., Thomassen, K., and Solbes, A., "Analysis of Solid Teflon Pulsed Plasma Thruster," *Journal of Spacecraft and Rockets*, Vol. 7, No 12, Dec 1970, pp 1402-06.

2. Peterkin, R.E., Jr., and Frese, M.H., "MACH: A Reference Manual - First Edition," Air Force Research Laboratory: Phillips Research Site, July 10, 1998.

3. Mikellides, P.G., and Turchi, P.J., "Modeling of Late-Time Ablation in Pulsed-Plasma Thrusters," AIAA Paper 96-2733, July 1996.

4. Mikellides, P.G., Turchi, P.J., Leiweke, R.J., Schmahl, C.S., and Mikellides, I.G., "Theoretical Studies of a Pulsed-Plasma Microthruster," IEPC Paper 97-037, August 97.

5. Turchi, P.J., and Kamhawi, H., "PPT Thermal Management," AIAA Paper, 25th International Electric Propulsion Conference, Cleveland, OH, 1997.

6. Wentink, T., Jr., "High Temperature Behavior of Teflon," AVCO-EVERETT Research Laboratory, Contarct No. AF 04(647)-278, July 1959.

7. Mikellides, I.G., "Theoretical Modeling and Optimization of Ablation-Fed Pulsed Plasma Thrusters," Ph.D. Dissertation, 1999, The Ohio State University, Columbus, Ohio.

8. Turchi, P.J., "Directions for Improving PPT Performance," *Proceedings of the 25th International Electric Propulsion Conference,* Vol. 1, Electric Rocket Propulsion Society, Worthington, OH, 1998, pp. 251-258.

9. Turchi, P.J., Mikellides I.G., and Kamhawi, H., "Optimization of Pulsed Plasma Thrusters for Microsatellite Propulsion," AIAA Paper 99-2301, June 1999.

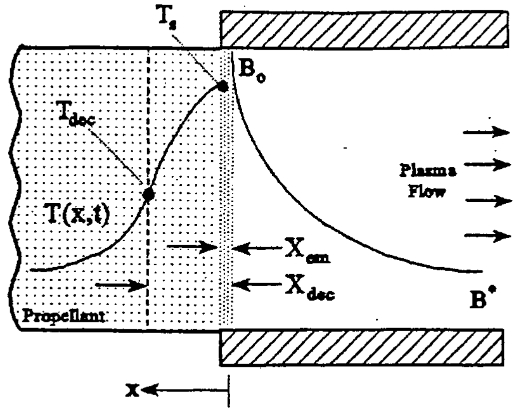

Figure 1. PPT schematic depicting depths for solid decomposition, X_{dec} and electromagnetic acceleration, X_{em}.

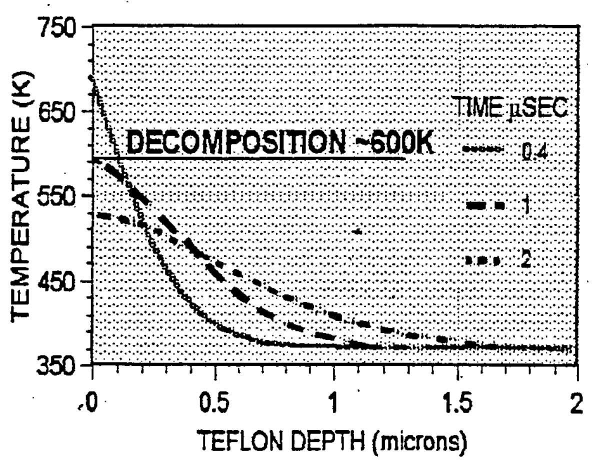

Figure 2. Temperature profiles within the solid propellant, as calculated by MACH2.

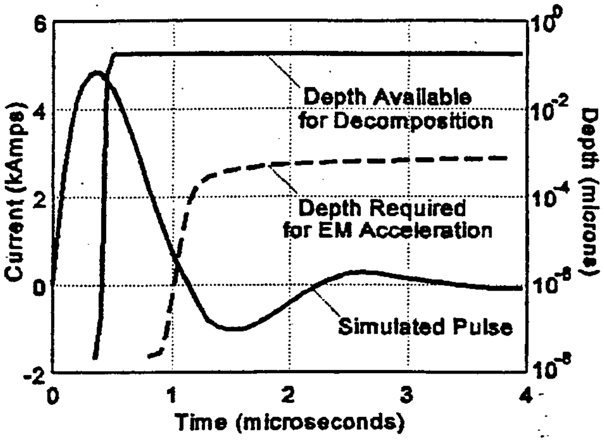

Figure 3. MACH2 calculation of electromagnetic and decomposition depths from the LES-6 simulations (a decomposition temperature of 600 K is assumed).

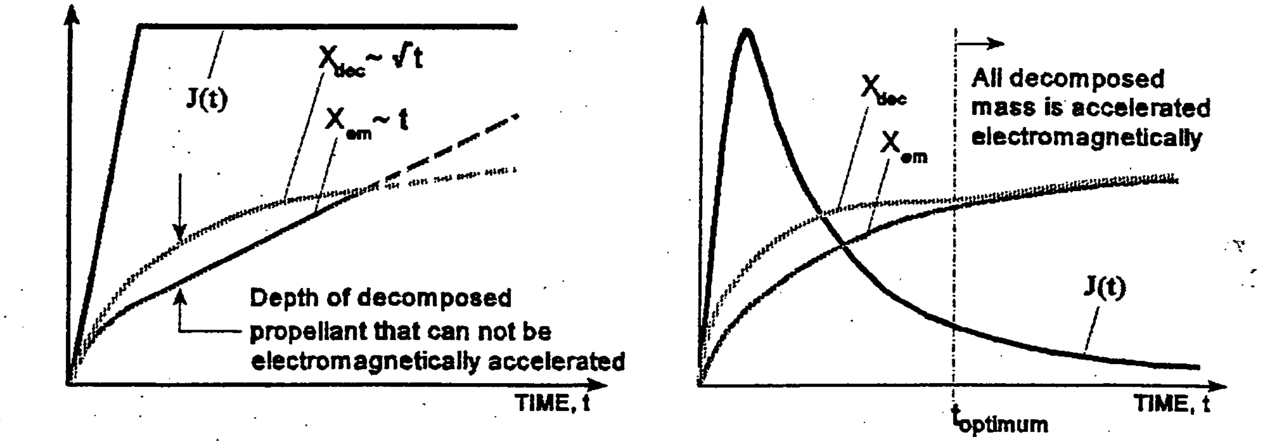

Figure 4. Qualitative evolution of decomposed and electromagnetically accelerated mass for steady-state and quasi-steady current waveforms.

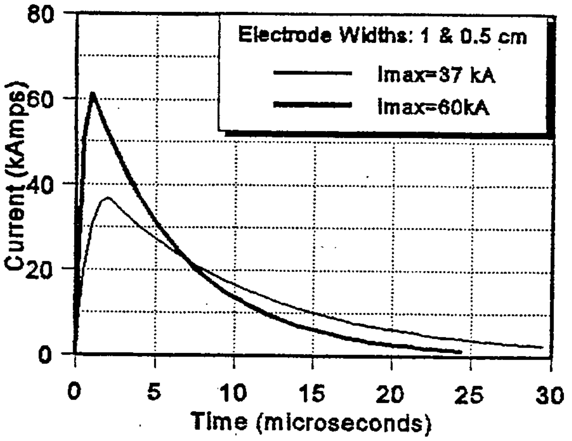

Figure 5. Prescribed, MACH2 waveforms for optimization calculations in rectangular geometry.

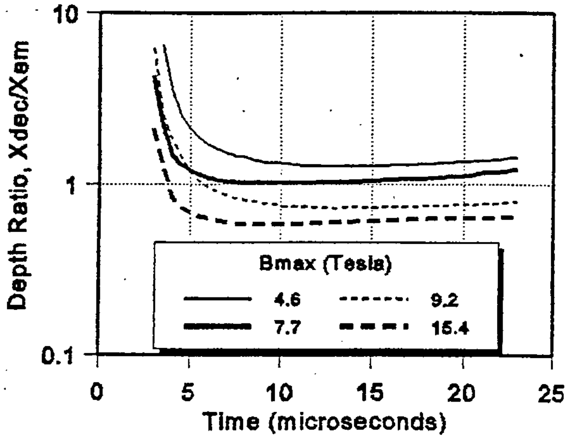

Figure 6. Evolution of X_{dec}/X_{em} at different maximum magnetic field values, $B_{max} = \mu J_{max}$/width (T_{dec}=673K)

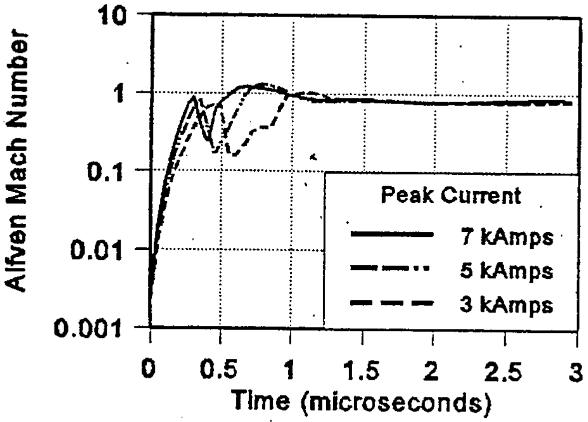

Figure 7. MACH2 evolution of the Alfven Mach number (near the exit) to sonic condition.

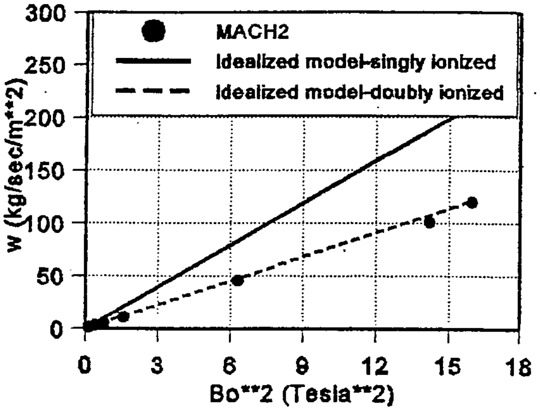

Figure 8. Comparison of the analytical model with MACH2, steady state simulations for the mass flow (per unit area) as a function of the operating magnetic field (squared), B_o^2.

Variable	MACH2	Analytical model ($\Delta h \equiv h_* - h_o = \epsilon_i$)		
		Singly ionized	Doubly ionized	Δh (MACH2)
T_* (°K)	857	886	865	863
u_* (km/s)	36.3	20	34.9	36.8
B_o/B_*	1.8	1.732	1.732	1.732

Table 1. Comparison of analytical model with steady-state, MACH2 simulation for B_o (= $\mu J/d$) = 4T.

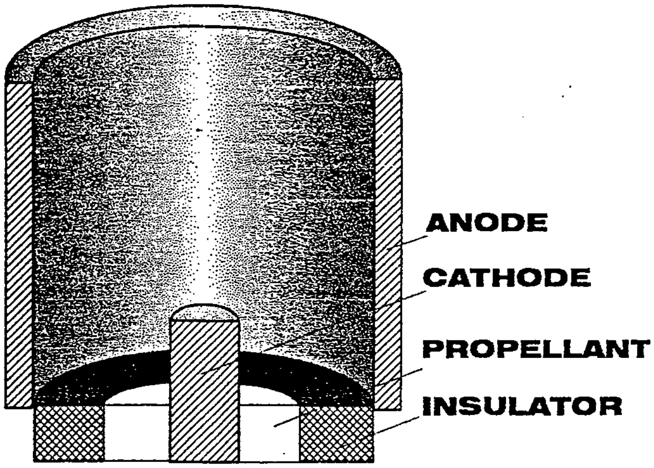

Figure 9. Schematic of the annular PPT configuration used in the MACH2 simulations.

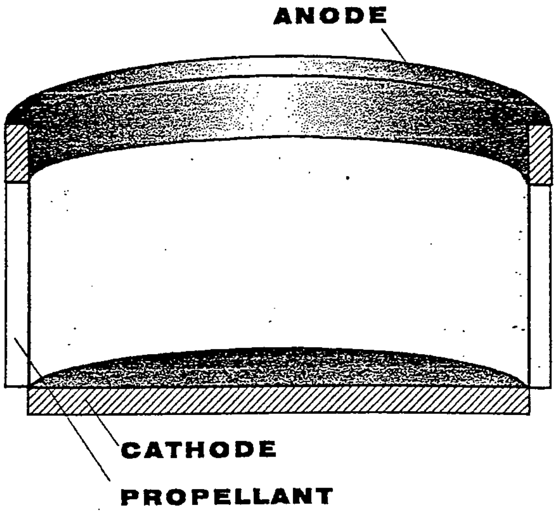

Figur 10. Schematic of the linear pinch PPT configuration used in the MACH2 simulations.

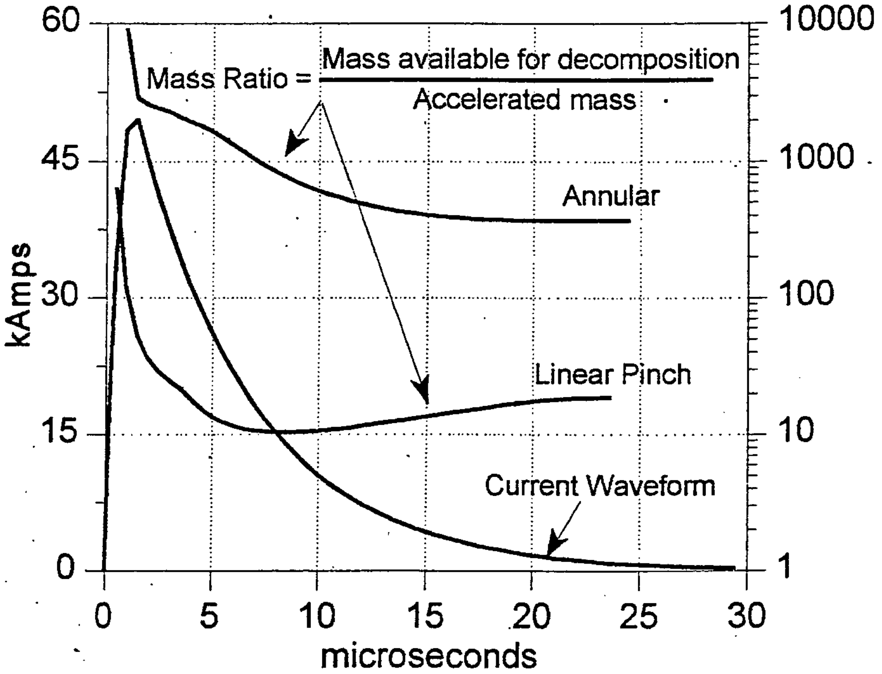

Figure 11. Typical current waveform and mass ratios from the coaxial PPT simulations.

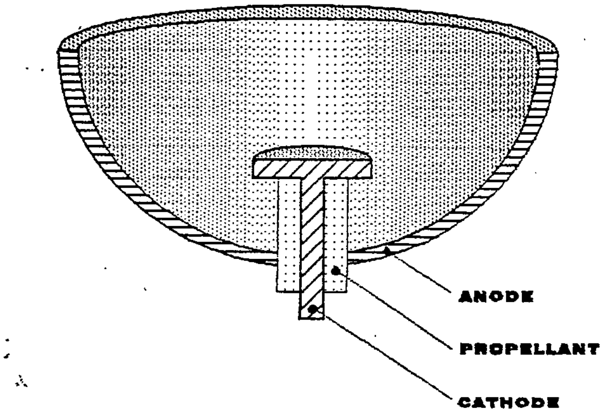

Figure 12. Schematic of the inverse pinch configuration used in the MACH2 simulations.

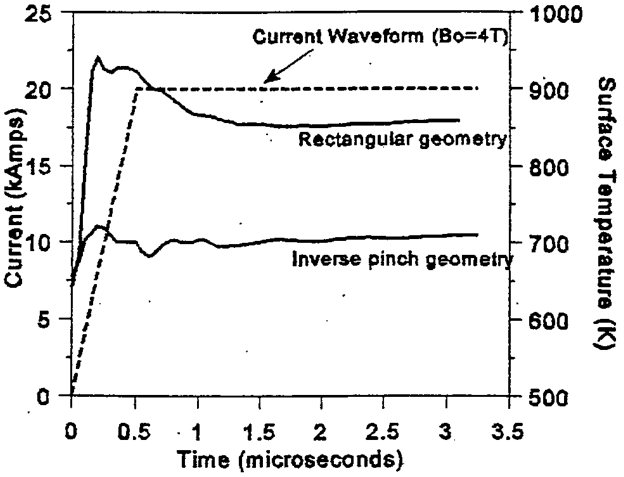

Figure 13. Evolution of the propellant surface temperature in the rectangular and inverse pinch geometries for an idealized current waveform.

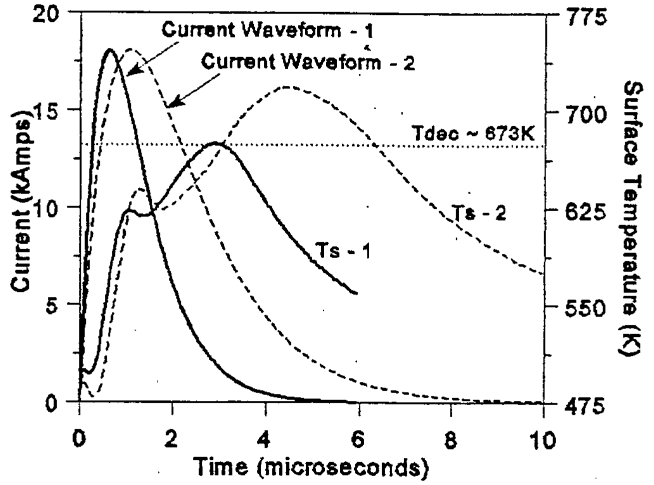

Figure 14. Evolution of the propellant surface temperature, Ts, for two (prescribed) critically-damped current waveforms.

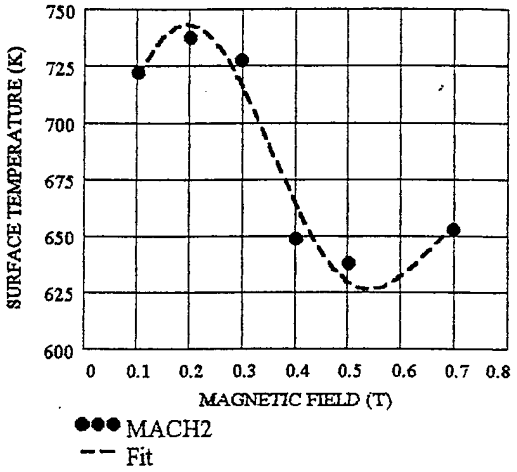

Figure 15. Variation of the propellant surface temperature with magnetic field (in steady state) in the inverse pinch geometry.

Kris Fischer
224 2060
Image Maker
p4:10

IEPC-99-205

Quantitative Radiation Measurements of the Pulsed Plasma Microthruster

T. Umeki and P.J. Turchi
The Ohio State University
Columbus, Ohio, USA

**26th International Electric Propulsion Conference
October 17-21, 1999, Kitakyushu, Japan**

QUANTITATIVE RADIATION MEASUREMENTS OF THE PULSED PLASMA MICROTHRUSTER

Tomokazu Umeki* and Peter J. Turchi†
The Ohio State University
Columbus, Ohio, USA

Abstract

Absolute spectral-radiance of the emission spectra from the exhaust of a Pulsed Plasma Microthruster (PPT) was spectroscopically obtained with an intensified charged-coupled-devise (ICCD) detector, a spectral-radiance calibration lamp and other related optics. The measured values of spectral radiance are used to evaluate the electromagnetic effect of the PPT exhaust to sensitive equipment such as optical sensors carried by a satellite. The benchmark PPT was operated at 10 J energy level for quantitative spectroscopy. Species in the spectra range of 400 to 700 nm were identified followed by measurements of the absolute amount of the spectral radiance for each spectrum. The possible sources of electromagnetic disturbance from the PPT exhaust to the optical sensor were singly and doubly ionized carbon species ranging from 3280 to 520 μW/(sr-mm^2-nm) of spectral radiance.

Introduction

The Pulsed Plasma Microthruster (PPT) has been a very practical device for satellite orbit position control due to its fine thrust-adjust capability as well as structural simplicity and robustness despite of low efficiency. (1) Electromagnetic Interference (EMI) from the PPT exhaust can be significantly adverse to sensitive equipment on-board (e.g optical sensors carried by Space Technology 3 Mission satellites) and must be investigated in advance. The present paper evaluates such possible effects by disclosing the emission sources and their absolute amounts of spectral radiance after conducting quantitative spectroscopic measurements of the electromagnetic radiation from the PPT exhaust.

Experimental Apparatus

The quantitative spectroscopic measurements were performed at The Ohio State University Aeronautical & Astronautical Research Laboratory (OSUAARL) with the following apparatus:

Vacuum Facility

A 1.3 m^3 stainless-steel vacuum tank has a cylinder-shape (0.6m dia x 4.8 m length). Pressure inside the tank was measured with Varian 531 Thermocouple Gauge Tube with 801 Thermocouple Gauge Controller (0.001 to 2 Torr range). It is kept at 3 milliTorr with two vacuum pumps (Welch 1374 DuoSeal Vacuum Pump ; ultimate pressure = 0.1 milliTorr). Each pump is connected to the one end of the tank.

PPT Thruster

The benchmark PPT (2) built at OSUAARL was used for the measurement. It consists of a thrust chamber and an LRC circuitry. The chamber is constructed with two copper electrodes and a Teflon propellant. The width of the electrode and the gap between two electrodes are 2.54 cm. The Teflon was originally positioned 2.54 cm from the tip of the electrodes. The LRC circuitry consists of a 116 nH external inductance, a 16 mΩ external resistance and a 10 μF storage capacitance.

Spectroscopic System

The spectroscopic system, shown in Fig.1 and Fig.2, comprises a condensing lens, a

---

*Graduate Research Assistant
†Professor

spectrometer, a detector, a Geissler tube, a HeNe laser, and a spectral-radiance calibration lamp .

The condensing lens (f/=5, focal length = 25 cm) with an iris images the optical object onto the entrance slit (set to 50 µm) of the spectrometer. For this measurement, all data were obtained in side-on direction 2.54 cm from the electrodes exit plane above the center of the electrodes assuming that the optical sensor is located on one side of the thruster.

The spectrometer (RTS Laboratory) has a focal length 1.2 m with f/=10 and carries a 1200 grooves/mm grating (Bausch & Lomb) yielding the reciprocal linear dispersion of ~0.6 nm/mm (for the first order spectra) at the exit slit. The light dispersed by this grating is focused onto the intensified charged-coupled-device (ICCD) camera detector (Princeton Instruments 576S/RB-E). The ICCD detector has 576 x 384 pixel format (12.7 X 8.5 mm) and 50 ns minimum gating. These features enable to obtain spatially and temporally resolved spectroscopic data. It has also 16 bits dynamic range with variable gain for sensitivities 1 to 100 counts per photoelectron to detect very low-intensity light. Spectral range of the ICCD camera is 180 ~ 800 nm. The spectral resolution for the first order spectra on the ICCD detector is 0.013 nm/pixel changing slightly with the wavelength.

Geissler tubes (Sargent-Welch Scientific Company, Edmund Scientific Company) were used to calculate the wavelengths of observed spectra. These include argon, chlorine gas, helium, mercury vapor, neon, and xenon tubes.

A HeNe laser (Melles Griot, 0.5 mW) was used for obtaining optical alignment by guiding its beam from the spectrometer exit-slit to the entrance slit and thereby locating the position of the optical object.

An absolute spectral-radiance calibration lamp (The Eppley Laboratory) was used to obtain the absolute value of spectral radiance in µW/(sr-mm^2-nm) from the ICCD-detector output in count. This conversion process is explained later. The lamp is calibrated for the range of 225 to 2400 nm and has a tungsten ribbon filament 10 cm behind a fused silica window 3 cm in diameter through which the radiation was measured.

Diagnostics and Results

Current Waveform

PPT was operated for 10 J energy level. The current waveform was computed numerically as shown in Fig.3 by integrating I-dot (current value derivative with respect to time) signal obtained from the Rogowski coil(2).

As seen in the figure, the entire event of thrusting ends in 15 µs. This value was used later to determine the gate width or shutter period of the ICCD detector.

Species Identification

Emission spectra were measured from 400 to 700 nm in this work to disclose the light-source species in the electromagnetic radiation from the PPT exhaust.

The gate or the shutter of the ICCD detector was opened 0.1 µs after triggered by the signal from the Rogowski coil at the PPT ignition. Then the gate was kept opened for 15 µs to capture the whole event of the radiation. The intensifier gain was set to 40. Data acquisition was repeated at least seven times to observe the reasonable repeatability by checking if there is no outstanding output-variation between each time of the acquisition. The typical variation was ± 10 to15 %.

The wavelength of an observed spectrum was calculated by interpolating or extrapolating the known wavelengths(3) of spectra from the Geissler tubes. One example of the observed spectrum from the PPT exhaust is shown in Fig. 4. along with the Geissler-tube spectra used for the wavelength calculation. The Geissler-tube spectra in this figure are argon lines of 425.1185, 425.9362, 426.6286, 427.2169, and 430.010 nm, respectively.(3) Interpolating 426.6286 and 427.2169 nm, the wavelength of the spectrum from the PPT exhaust was obtained. As seen from the figure, the wavelength-range that one data acquisition can cover is about 8nm depending on the wavelength.

This procedure was repeated to cover the range of 400 to 700 nm. The resulted spectra are shown in Fig.5 with the identified species which were determined by the existence of a set of spectral lines of known wavelength(3), (4) of the species. The most of the observed spectra other than singly ionized carbon, doubly ionized carbon and neutral hydrogen in the figure were singly ionized nitrogen and singly ionized oxygen.

Absolute Spectral-radiance Measurement

As the first step to convert the ICCD output in count to the absolute spectral-radiance in μW/(sr-mm^2-nm), the radiation from the spectral-radiance lamp was measured with the ICCD detector. The measurement was performed at each wavelength of the observed species since the ICCD detector sensitivity varies along the wavelength.

The lamp was set to the position where the PPT was located and the tungsten filament was focused onto the entrance slit of the spectrometer with the same condensing lens. The lamp was operated at 35 A since the lamp was calibrated at 35 A to provide the reference spectral-radiance values. The setting of the ICCD detector was exactly same as the case of PPT-exhaust measurements except that the gate of the ICCD detector was opened by the signal from a waveform generator (Wavetek 50MHz Pulse/Function Generator) in stead of the Rogowski signal and the gate opening-width was set to 1 ms in stead of 15 μs. 15 μs of gating did not provide enough exposure to the detector from the lamp and 1 ms of gating yielded the same order of magnitude of the output in count compared to the case of PPT-exhaust measurements. Hence the value of spectral-radiance needs to be multiplied by 1 ms / 15 μs to compensate this difference in exposure time when the detector outputs from the PPT exhaust are compared to those from the lamp.

The correlation between the ICCD output and the spectral-radiance after the time compensation (namely, the spectral-radiance values multiplied by 1 ms / 15 μs) is graphed in Fig. 6. Between data points, values are interpolated. Using this correlation, the conversion factor from the ICCD output to the spectral radiance is obtained along the wavelength of interest by simply dividing the spectral-radiance value by the ICCD-output value of the same wavelength. The resulted conversion-factor values in μW/(sr-mm^2-nm)/count is shown in Fig.7. Based on this conversion factor, the observed spectra in count in Fig.5 can now be expressed in absolute spectral-radiance in μW/(sr-mm^2-nm) as shown in Fig.8.

Conclusions and Discussions

The emission sources from the 10J PPT exhaust and their absolute amounts of spectral radiance were obtained from quantitative spectroscopy to evaluate the electromagnetic disturbance to the optical sensor. In 400 to 700 nm range, the most potential sources of disturbance and their absolute values of spectral radiance are 426.7 nm CII (3280 μW/(sr-mm^2-nm) max), 464.7 nm CIII (1460 μW/(sr-mm^2-nm) max) , 465.0 nm CIII (1120 μW/(sr-mm^2-nm) max) , 657.8 nm CII (920 μW/(sr-mm^2-nm) max) and 658.3 nm CII (520 μW/(sr-mm^2-nm) max).

These results may be dependant on the operating conditions and environment such as energy level, thrust frequency, background pressure and electrode material. Background pressure effects due to contaminants such as hydrogen, nitrogen, and oxygen are isolated as the main factors for such dependancy. UV range spectra normally considered to be strong energy sources were not examined since they can be easily circumvented by proper placement of a protective plate between the thruster and the sensitive equipment. Indeed, during our experiment emission below 350 nm was blocked by the plexiglass optical-window attached to the vacuum tank.

Although singly-ionized-carbon lines of strong intensity were observed, no outstanding singly-ionized-fluorine line was observed. This seems to be due to the very low values of the product of the transition probability and the density of the fluorine emitter in the upper excited state (more precisely it is the integration value of the density across the line of sight). Knowing that some fluorine lines have the transition probabilities of the same order of magnitude as those of observed carbon lines, the emitter density considered to be very low. In fact, some of singly-ionized-carbon lines which have the same order transition-probability were not observed. This should be due to the same reason. On the other hand, neutral-hydrogen lines of high spectral radiance were clearly observed due to the large value of the transition probabilities.

These spectral radiance measurements can be utilized to calculate the amount of electromagnetic radiation from the PPT exhaust. This can be accomplished by obtaining radiance values with respect to spectral width and considering the appropriate solid angle and area, and the emitting time period. This analysis will allow the evaluation of radiative energy losses and thus quantify their contribution to the thruster's efficiency degradation.

Acknowledgments

The authors would like to thank Eric Pencil at NASA Glenn Research Center and Henry Baust at Wright-Patterson Air Force Base for allowing us to use some of their optical equipment. This work was supported by NASA Glenn Research Center under NAG3-843.

References

[1] Myers, R.M., "Electromagnetic Propulsion for Spacecraft", AIAA 93-1086, Feb. 1993

[2] Kamhawi, H., Turchi, P.J., Leiweke, R.J., and Myers, R.M., "Design and Operation of A Laboratory Benchmark PPT", AIAA 96-2732, July 1996.

[3] Weast, R.C., *CRC Handbook of Chemistry and Physics,* CRC Press. Inc., Boca Raton, Florida, 1984.

[4] Wiese, W.L., Smith, M.W., and Glennon, B.M., *Atomic Transition Probabilities,* National Bureau of Standards, May 1966.

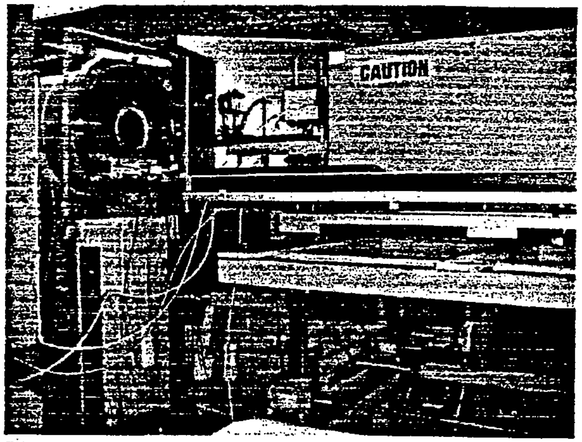

Figure 1. Overview of the spectroscopic system

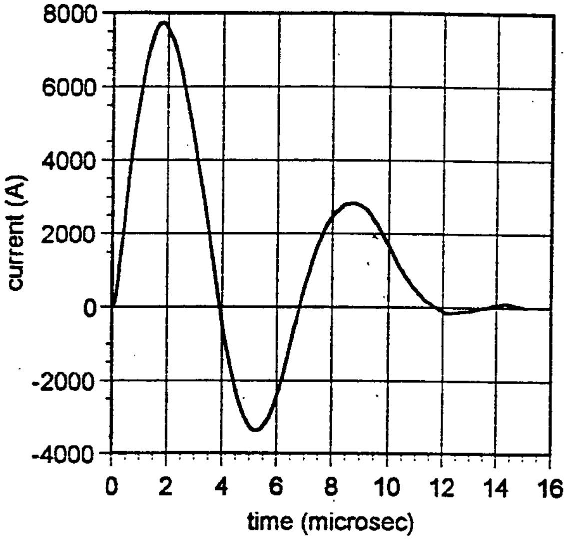

Figure 3. Current waveform

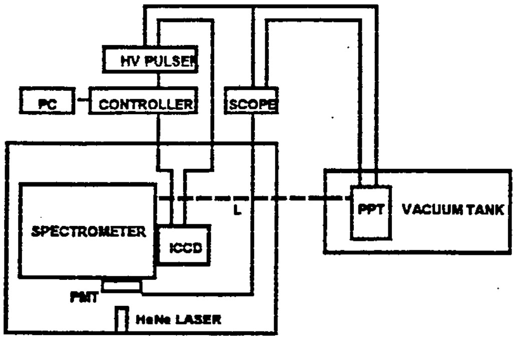

Figure 2. Schematic of the spectroscopic system

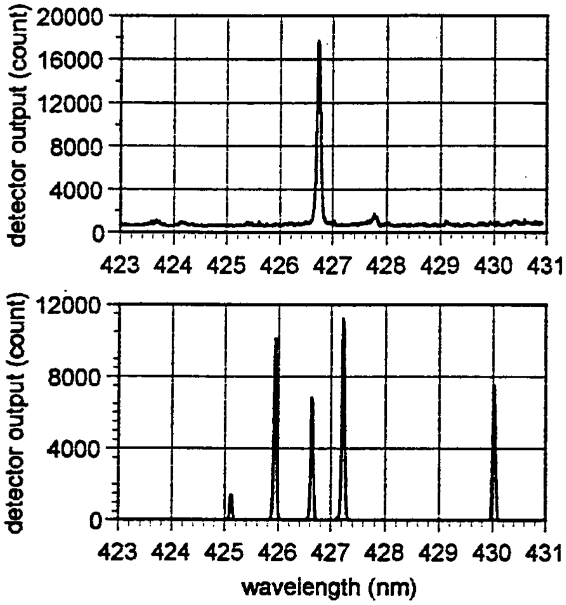

Figure 4. Observed spectrum for the PPT exhaust and Geissler-tube spectra.

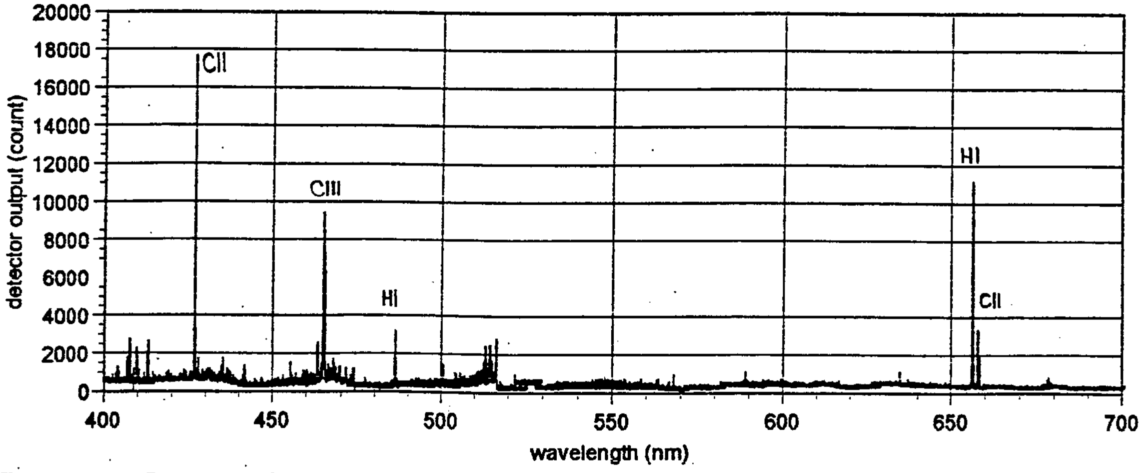

Figure 5. Observed spectra from 400 to 700nm with identified species

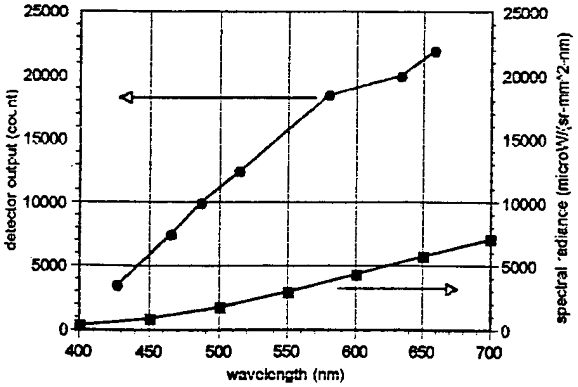

Figure 6. The correlation between the spectral radiance and the detector output.

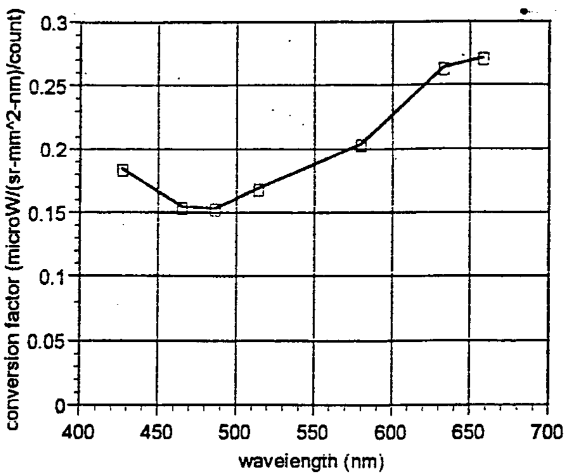

Figure 7. The conversion factor from the detector output to the spctral radiance.

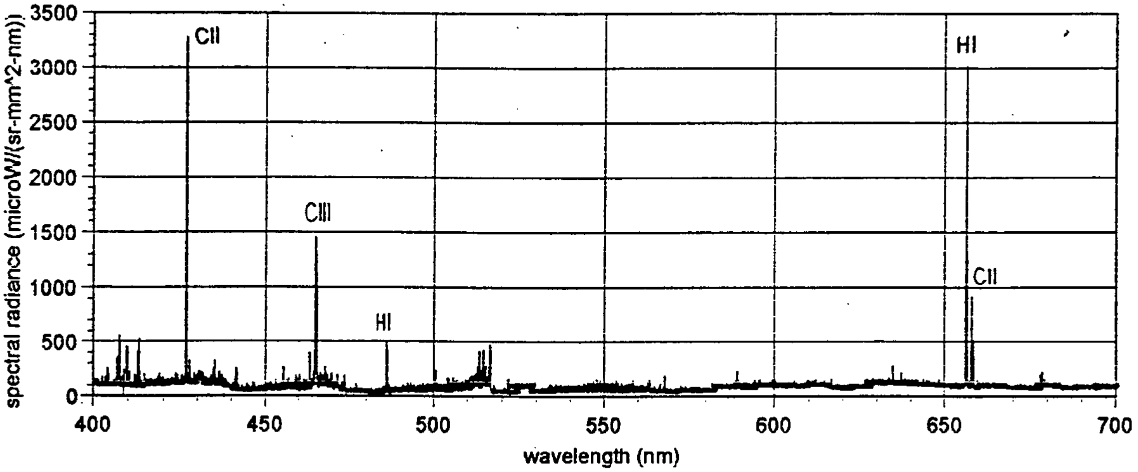

Figure 8. The absolute spectral radiance of the observed spectra.

AIAA-99-2301

Optimization of Pulsed Plasma Thrusters for Microsatellite Propulsion

P.J. Turchi, I.G. Mikellides, P.G. Mikellides and H. Kamhawi
Ohio State University
Columbus, OH

35th AIAA/ASME/SAE/ASEE Joint Propulsion
Conference and Exhibit
20–24 June 1999
Los Angeles, California

OPTIMIZATION OF PULSED PLASMA THRUSTERS FOR MICROSATELLITE PROPULSION

P.J. Turchi, I.G. Mikellides, P.G. Mikellides and H. Kamhawi

The Ohio State University
Columbus, Ohio USA

Abstract

Simplicity, robustness and ability to operate in pulses at low average power have allowed selection of the pulsed plasma microthruster (PPT) for spaceflight application even though its thrust efficiency and mass utilization have historically been very poor. Recent success in modeling PPT behavior has led to new insights that permit optimization of performance for microsatellite needs. In particular, the circuit current must match the propellant dimensions in order to minimize the loss of mass at very low exhaust speed. Ideally, this match occurs when temperatures in the propellant exceed the value for decomposition only for a depth corresponding to the mass accelerated electromagnetically by the plasma discharge. The unsteady nature of heat flow in the PPT requires consideration of both the temporal and spatial distribution of the discharge, in addition to the peak amplitude of the current pulse. The paper presents results of analytical and numerical modeling and discusses optimization of propellant properties for satisfying mission requirements.

Introduction

Pulsed plasma microthrusters (PPTs)[1] have a long history of use for station-keeping on small satellites with limited electrical power. Application of PPTs to microsatellite missions represents a natural evolution in spacecraft propulsion systems. Simplicity, robustness and ability to operate in pulses at low average power establish PPTs as leading candidates for microsatellite missions, even though their thrust efficiency has been very poor.

The PPT, while simple in its embodiment, incorporates considerable complexity, as suggested by the sketch in Figure 1. An arc discharge heats a solid propellant and provides a gradient of magnetic pressure that accelerates the ablated material. The arc current can rise in a fraction of a microsecond and continue for several microseconds in the oscillatory waveform of the traditional LRC-circuit, or for longer durations using inductive energy-storage[2]. Heat diffuses into the propellant slab, causing decomposition of material, only a portion of which accelerates electromagnetically to speeds exceeding 10 km/s; the rest of the decomposed mass leaves at much lower speed (< 1 km/s). Recent modeling of PPT operation using the MACH2 magnetohydrodynamics code[3] has identified and quantified the mechanisms that cause inefficient propellant utilization. Post-pulse evaporation and macroparticle production account for the major portion of the total mass loss. These processes contribute minimally to the thrust because the speed of the expelled mass is based on the temperature of the solid (< 1000 K). An idealized analytic model prescribes the foundations for matching the current pulse and the PPT geometry in order to accelerate all the decomposed propellant electromagnetically, producing useful thrust at high specific impulse. Numerical simulations with the MACH2 code indicate that waveforms from circuits based on inductive-energy storage will optimize thrust efficiency.

Numerical Modeling

The time-dependent, 2½-dimensional, magnetohydrodynamic code, MACH2 has been successfully employed to model PPTs[4,5]. For example, simulation of the LES-6[1] thruster (see Figure 2) captures the experimental magnitude and trends for the impulse-bit. The computed mass of ablated propellant, (all of which participates in electromagnetic acceleration in these calculations), is much less than the experimental value for mass loss per shot (~10 μg at a stored energy of 1.85 J). The discrepancy in mass loss may result from two processes: late-time evaporation and macroparticle production, both of which degrade thrust efficiency. The late-time ablation (between discharge pulses), can be calculated by MACH2, but depends on the base temperature of the Teflon propellant. The average heat flow in the slab at a given repetition rate and capacitor energy determines this base temperature. At a base temperature of 520K, for example, propellant evaporation after the current pulse could account for as much as 55% of the total mass loss per shot.

Is that not depending on the lengths of plates & propellant slap?

2.

In experiments[6] at 40 J/pulse and a repetition rate of 1Hz, thermocouple measurements indicate a base temperature of 370 K. At this lower temperature value, evaporation between pulses contributes a negligible fraction to the total mass loss. Interrogation of the computed temperature profile within the solid Teflon, however, indicates that a significant portion of the propellant has been heated above the temperature for decomposition of the Teflon polymer. Based on a value for the temperature at which Teflon polymer chains break (~600K)[7], the depth of solid propellant above this value implies 116 μg of decomposed Teflon. This amount is more than an order of magnitude larger than the experimentally measured mass loss at this energy level. (This discrepancy would increase if late-time evaporation at elevated base temperatures occurs.) It is possible that a substantial portion of this decomposed material has the opportunity to re-solidify as the surface cools, or that the effective decomposition temperature within PPT operation is higher than the value for polymer breaking (often taken as the sublimation temperature of Teflon). In the latter case, comparison of the experimentally-measured mass loss for LES-6 with the MACH2 simulation suggests an effective decomposition temperature for Teflon (in PPTs) of 673K. The computed decomposition depth based on the sublimation value is 0.18 microns while the depth based on 673K is 0.0155 microns. For purposes of optimization studies, we shall use the higher value of temperature in order to compare directly with the LES-6 performance.

Using other propellants: The higher α the higher the evaporation affect

Idealized Model

A quasi-steady, one-dimensional, idealized model provides key insights into the PPT operation. For a discharge current J, and rectangular channel width w, the magnetic field at the propellant surface is,

$$B_o = \frac{\mu_o J}{w} \qquad (1)$$

(see Figure 1). In the limits of high magnetic Reynolds number and magnetic pressure greatly exceeding the plasma pressure, magnetohydrodynamic flow from the channel into a field-free vacuum implies that there exists a magnetosonic condition in the channel. This condition corresponds to a flow speed equal to the local value of Alfven sound speed:

$$u^* = \frac{B^*}{\sqrt{\mu_o \rho^*}} \qquad (3)$$

where ρ is the mass density and starred quantities refer to (magneto) sonic values. From the derivation in Appendix I, the value of the magnetic field at the magnetosonic point is proportional to the magnetic field at the propellant surface:

$$B^* = \frac{B_o}{\sqrt{3}} \qquad (3)$$

Appendix I also calculates the plasma speed at the magnetosonic point:

$$u^* = 1.468\sqrt{2Q^*} \qquad (4)$$

where Q^* is the change of flow enthalpy per unit mass due to electrical dissipation between the stagnation and magnetosonic points. (If ionization of the plasma dominates this change, u* is about 50% higher than Alfven critical velocity.) At fixed u*, the magnetic pressure difference, $(B_o^2-B^{*2})/2\mu_o$, from the propellant surface to the location of the magnetosonic point defines the mass flow rate per unit area, $\dot{m}/A$, required to maintain the electrical discharge and flow in steady state. The current and channel width thus prescribe the mass flow per unit area at the propellant surface that must be provided by ablation.

Adjacent to the propellant surface, the mass flow rate per unit area is limited by a choking condition, based on the usual (thermal) sound speed. For a calorically perfect flow, with a stagnation pressure proportional to the equilibrium vapor pressure of the propellant, this condition only depends on the surface temperature, T_s. The surface temperature, in turn, scales the temperature profile in the solid propellant. Comparison of this profile with the value for decomposition of the solid propellant indicates the opportunity for mass loss from the propellant slab. Only a portion of this mass, however, may be needed to sustain the steady-state position of the discharge. Indeed, for constant current, the depth of material required by the discharge increases linearly with time, while diffusion theory for the heat pulse suggests that the depth of decomposed mass will increase as the square root of time. The upper sketch in Figure 3 depicts this difference in depths, in the case of constant discharge current, for which the idealized model predicts constant values of surface temperature and ablation rate. If the discharge current ends before the curves intersect, a portion of the decomposed propellant will not be accelerated electromagnetically. Figure 4 displays the depth for decomposition and depth of material required by the discharge for the LES-6 waveform. (A decomposition temperature of 600 K is used here. The higher value of 673 K provides similar behavior, but corresponds to the experimental mass loss in LES-6.) Figure 3 also displays a sketch for a current pulse that is not constant, indicating the opportunity for the depth of material needed by the discharge to merge with that for thermal diffusion. Such merger corresponds to the evolution of a deflagration wave that propagates into the propellant, powered electromagnetically instead of chemically. The model thus suggests directions for improving poor propellant utilization by implying that there exist current pulse times that will utilize the major portion of the decomposed propellant for electromagnetic acceleration.

Confirmation of Idealized Model

By providing a current waveform in MACH2 that rises quickly to a steady value, the principal elements of the idealized model can be checked. Computed evolution of the pertinent variables (see Figure 5) shows that indeed steady-state operation is achieved within three microseconds, (a few times the current risetime used here). Figure 6 indicates that the magnetosonic condition is attained in all three cases of current amplitude, along with the expected thermal sonic condition adjacent to the propellant's surface. The location of the magnetosonic point, just downstream of the first portion of the discharge current, does not vary significantly with interelectrode spacing or electrode length. The mass flow rate per unit area scales as the square of the magnetic field in agreement with the notion of sustaining a magnetic pressure difference established by the discharge, $\dot{m}/A \sim B_o^2$. This scaling is maintained for much higher peak currents than the three test cases (3, 5, and 7 kA) displayed in detail here. The computed magnitude of the mass flow rate is within 15% of the value calculated by the idealized model. The agreement between MACH2 and the idealized model lends credence both to the utility of the analytical model and the accuracy of MACH2.

Optimized Current Waveforms

The qualitative profiles depicted in Figure 3 suggest sufficiently long pulse times will assure that all the available decomposed mass participates in the electromagnetic acceleration process. Numerical estimates, however, indicate that if current levels are held constant, pulse times must exceed a few hundred microseconds to achieve such behavior (at least for surface magnetic fields of less than 5 T). For microspacecraft applications, the available energy per pulse will not permit these times with conventional circuit elements. Use of inductive energy storage can provide discharge durations of 10 to 50 microseconds at initial capacitor energies in the range of 50 J or less. For the PPT, such inductive energy-storage circuitry can be accomplished merely by using the PPT plasma to short the energy storage capacitor soon after maximum energy has been delivered to an inductor in series with the PPT, (i.e., just after voltage zero occurs on the capacitor). Figure 7 displays the arrangement we have developed along with the desired behavior of the current waveform.

For initial optimization surveys, the inductive-circuit waveform has been simulated by a typical LC current rise, followed by an L/R decay, (see Figure 8, top). MACH2 handles the complex interactions of the discharge, plasma flow and ablation process, as we seek to maximize the fraction of propellant accelerated electromagnetically. A combination of two current waveforms and two widths of thruster channel provides four different values of the magnetic field at the surface, B_o. The optimization is displayed in the lower part of Figure 8, in terms of a ratio of depths for the two important processes: electromagnetic acceleration and solid decomposition. This depth ratio indicates the percentage of total decomposed mass compared to that used by the discharge for electromagnetic acceleration. Decrease of this ratio toward unity implies efficient mass utilization. Higher magnetic fields (peak current per width) at the propellant surface provide substantial improvements in propellant utilization because more mass is needed by the discharge. A basic scaling for efficient PPT performance requires matching the circuitry to the width (or circumference) of the thruster in order to exceed minimum values of magnetic field. This matching and the design of the electrical circuit parameters must include the temporal-variation of the current, so that there is sufficient time for the ablation wave to merge with the position of the temperature value in the solid corresponding to propellant decomposition. Simply delivering a high current pulse to narrow electrodes for a short time may not be sufficient to achieve this two-part optimization condition. Empirical exploration of PPT performance can readily miss the conditions for efficient behavior. Furthermore, the selection of propellants influences the matching of current and geometry by providing different values for decomposition temperature, thermal diffusivity and equilibrium vapor pressure (vs surface temperature).

Simulations in Coaxial Geometry

Close comparison of experimental data and theoretical modeling of the PPT in its traditional rectangular configuration is severely hampered by three-dimensional effects. Optical measurements cannot use Abel inversion techniques, and theoretical calculations, even with state-of-the-art computer codes are simply inadequate. This situation has prompted us to focus on PPTs in coaxial geometry.

MACH2 is once again utilized to investigate and improve PPT performance in a variety of axisymmetric configurations, based on insights gained from optimization of the rectangular geometry. Two coaxial PPT configurations are depicted in Figures 9 and 10. Both were simulated by MACH2 using a prescribed current pulse with a maximum magnetic field of about 10T based on a fast rising, slowly decaying waveform that peaked at 50 kAmps. Figure 11 shows the temporal behavior of the current and the ratio of decomposed mass to mass that is electromagnetically accelerated, for a typical case. Pulse decay time, exposed propellant area and peak current were varied during these simulations, in an attempt to quantify their effect on the utilization of mass during the acceleration process.

In the annular configuration of Figure 9 it is found that for a given current waveform, the mass ratio has a minimum for an exposed propellant area that is about a fifth of the interelectrode gap area. Larger exposed areas result in a greater amount of decomposed mass, due to the increased propellant areas at the larger radii. Higher mass ratios are also associated with smaller exposed areas, due to the deeper decomposition depths in the solid as a consequence of an elevated heat flux near the ablating surface. For a fixed propellant area, the minimum ratio of decomposed mass, to mass that has been electromagnetically accelerated, improves with increased pulse duration, due to the prolonged electromagnetic acceleration as the propellant cools. It is evident however that, although improved, the mass ratio is still much higher than desired. At the optimum propellant area and for a pulse time of about 30 μsec, the amount of decomposed mass is approximately two orders of magnitude higher than the amount accelerated. Further optimization is achieved with longer pulses; but in a manner that is inversely proportional to the square root of the pulse decay time. This implies that for the particular arrangement under study, in order to eliminate the potential of any wasteful release of mass due to propellant decomposition, the current waveforms that must be implemented are of much longer duration (~milliseconds) than those attainable by power source requirements typical for microsattellite applications. Note that although millisecond operation of ablation-fed, self-field magnetoplasmadynamic thrusters[8,9] could yield useful performance, the powers and energies of such devices are incompatible with those for microsatellite resources.

annular config.

In contrast to the rectangular PPT, the principal difficulty with a coaxial PPT in this simple annular arrangement is the decrease in magnetic field with radius over the propellant surface. If the necessary magnetic field for efficient propellant utilization is achieved near the center conductor, the propellant at larger radii is not used properly. There will also be a tendency for the propellant surface to recede faster at smaller radii, which means a change in shape over the course of the mission. (Such variation in surface geometry, of course, is not new for solid-propellant rockets.)

In an attempt to eliminate the added complexities of magnetic field variation with radius, a linear pinch geometry (Figure 10) has been pursued, under conditions similar to those implemented in the annular geometry. As illustrated by the typical case in Figure 11, the linear pinch configuration offers considerable improvement over its annular counterpart. The amount of decomposed mass however, is still approximately ten times higher than the amount accelerated electromagnetically. The impediment here is the decrease in area available for current conduction due to a required reduction in radius for microsatellite applications.

linear pinch

The characteristic thickness through which the current conducts at the entrance of a magnetosonic flow is,

$u^* = \frac{B^*}{\sqrt{\mu_0 \rho^*}}$

$$\delta^* = \frac{\eta}{\mu u^*} \qquad \textbf{(6)}$$

where η is the plasma resistivity, μ is the permeability, and u* is the magnetosonic speed attained by the flow after this thickness of current. If the radius of the propellant surface greatly exceeds, δ*, the linear pinch arrangement would resemble a circular array of rectangular PPTs (directed inward), and we would expect the same propellant performance; (we have verified this with MACH2). For propellant radii comparable or less than δ*, however, the discharge and flow conditions change resulting in higher propellant temperatures. Under such conditions, the linear pinch is characterized by a low magnetic Reynolds number, high-beta flow and operates more like an electrothermal thruster. The downstream flow speed scales with the thermal sound speed rather than the Alfven sound speed (as was observed in the rectangular configuration).

$\beta = \frac{P_{thermal}}{P_{mag}}$

2

The consequences of the ensuing onerous heat flux on the propellant are much higher surface temperatures (nearly twice as high as those calculated in the rectangular configuration) and increased depths of propellant available for decomposition. As in the annular configuration, increasing pulse decay times and maximum magnetic field both reduce the mass ratio. An increased propellant length to radius results in a higher mass ratio.

The restrictions associated with the two previous configurations lead to the geometry illustrated in Figure 12. Here, current flow between the electrodes creates an electromagnetic force on the plasma that is directed radially outward in an arrangement known as an inverse pinch. The magnetic field here is uniform along the ablating boundary. The plasma is unconfined (contrary to the linear pinch geometry) as it expands freely to a downstream magnetosonic condition, under the influence of the magnetic pressure gradient. A radially inward force $B^2/\mu r$, the so-called magnetic tension tends to offset the radial expansion.

As a consequence, the mass flow per unit area in the inverse pinch is about two orders of magnitude lower than in the rectangular geometry and the ensuing surface temperature was more than one hundred degrees lower, as illustrated in Figure 13. This suggests that contrary to all previous geometries studied here, only the inverse pinch configuration offers the convenience of axisymmetry for improved correlation between experiment and theory, and the opportunity for operation at relatively high magnetic fields with propellant temperatures below the effective decomposition limit.

Optimizing Specific Impulse

The determination of the optimum value of specific impulse or exhaust speed depends on the mission requirements. If not limited by drag or the so-called power supply penalty, higher exhaust speeds maximize the payload mass delivered to a desired trajectory or orbit. Appendix I suggests that the plasma speed at the magnetosonic location and speeds in the downstream exhaust scale with Alfven critical speed. Choice of propellant for the PPT, therefore, can significantly affect the available value of specific impulse, (in addition to playing a major role in the efficiency of propellant utilization for a given current pulse and thruster size).

For some missions, (e.g., orbit-raising against atmospheric drag), thrust-to-power ratio determines the optimum specific impulse. The thrust-to-power ratio varies inversely with exhaust speed, u_E:

$$\frac{F}{P} = \frac{u_E \Delta m}{u_E^{\,2} \Delta m / 2\eta} = \frac{2\eta}{u_E} \qquad \textbf{(6)}$$

where η is the thrust efficiency. We may write this thrust efficiency as the product of an efficiency of delivering energy to the thruster, η_s, and the fraction of the exhaust energy in the form of directed kinetic energy <u>vs</u> energy lost to internal states (e.g., ionization), W_f:

$$\eta = \eta_s \left[\frac{u_E^2}{u_E^2 + 2W_f} \right] \qquad (7)$$

Thus, the thrust-to-power ratio becomes:

this value is right. The missing 2 in (8) is just a typing error.

$$\frac{F}{P} = \frac{\eta_s u_E \cdot 2}{u_E^2 + 2W_f} \qquad (8)$$

This maximizes for $u_E = \sqrt{(2W_f)}$. The lowest values of energy lost in the exhaust flow provide the highest thrust-to-power ratios. Based only on thrust-to-power ratio, plasma thrusters will always suffer in comparison to devices that do not require ionization of the working fluid, e.g., water resistojets. If ionization dominates W_f, the optimum exhaust speed would equal Alfven critical speed. Thrusters such as the PPT and magnetoplasmadynamic arcjet, thus, will tend to operate with exhaust speeds that exceed the value for maximum thrust-to-power ratio.

Conclusions

The potential of the PPT to satisfy different mission constraints, ranging from high thrust-to-power ratio for action against low-altitude drag to high specific impulse for station-keeping or maneuvering at higher altitudes, could be achieved by matching the propellant to the mission need. Optimization begins with specification of the propellant in terms of its Alfven critical speed and then continues by design of the thruster and propellant size to match the current waveform. The latter match demands consideration of the propellant properties, and may obtain guidance from idealized models. Detailed design, including circuit behavior, requires computational tools, such as MACH2. As usual, optimization must occur within other system constraints, such as propellant handling and concerns for spacecraft contamination. The history of the PPT and electric propulsion indicates that simplicity is often more important than maximum performance in selection of a spacecraft propulsion system. The insights and methods discussed in the present work should, nevertheless, expand the opportunities for new PPT systems.

Acknowledgments

The authors acknowledge the support of the NASA Glenn Research Center, the Air Force Office of Scientific Research, and the Ohio Supercomputer Center.

References

1. Vondra, R.J., Thomassen, K., and Solbes, A., "Analysis of Solid Teflon Pulsed Plasma Thruster," *Journal of Spacecraft and Rockets*, Vol. 7, No 12, Dec 1970, pp 1402-06.

2. Turchi, P.J., "Directions for Improving PPT Performance," *Proceedings of the 25th International Electric Propulsion Conference,* Vol. 1, Electric Rocket Propulsion Society, Worthington, OH, 1998, pp. 251-258.

3. Peterkin, R.E., Jr., and Frese, M.H., "MACH: A Reference Manual - First Edition," Air Force Research Laboratory: Phillips Research Site, July 10, 1998.

4. Mikellides, P.G., and Turchi, P.J., ""Modeling of Late-Time Ablation in Pulsed-

Plasma Thrusters," AIAA Paper 96-2733, July 1996.

5. Mikellides, P.G., Turchi, P.J., Leiweke, R.J., Schmahl, C.S., and Mikellides, I.G., "Theoretical Studies of a Pulsed-Plasma Microthruster," IEPC Paper 97-037, August 97.

6. Turchi, P.J., and Kamhawi, H., "PPT Thermal Management," AIAA Paper, 25th International Electric Propulsion Conference, Cleveland, OH, 1997.

7. Wentink, T., Jr., "High Temperature Behavior of Teflon," AVCO-EVERETT Research Laboratory, Contarct No. AF 04(647)-278, July 1959.

8. Andrenucci, M., Lensi, R., Naso, V., and Melli, R., "Design of Solid-Propellant MPD Thrusters," *Electric Propulsion and its Application to Space Missions,* vol. 79, Progress in Astronautics and Aeronautics, IAA, New York 1980, pp 586-601.

9. Paccani, G., "A Coaxial Non-Steady Solid Propellant MPD Thruster Experimental Analysis," *Journal of the British Interplanetary Society,* Vol. 41, pp 233-240, 1988.

APPENDIX I

Plasma Speed at Magnetosonic Point in Limit of Low Beta and High Magnetic Reynolds Number

For a one-dimensional, steady flow, in the limit of plasma pressure much less than magnetic pressure (low beta) and high magnetic Reynolds number (near the magnetosonic point), the equations of magnetohydrodynamics simplify considerably:

Continuity:

mass flow per unit area

$$\rho u = w = \text{constant} \qquad \textbf{(A1)}$$

Momentum:

$$\rho u \frac{du}{dx} = -\frac{d}{dx}\left(\frac{B^2}{2\mu}\right) \Rightarrow wu + \frac{B^2}{2\mu} = \text{constant} \qquad \textbf{(A2)}$$

Energy:

$$w\frac{d}{dx}\left(h + \frac{u^2}{2}\right) = -\frac{d}{dx}\left(\frac{EB}{\mu}\right) \qquad \textbf{(A3)}$$

where ρ = mass density, u = flow speed, h = specific enthalpy, E = electric field, and B = magnetic (induction) field.

At the magnetosonic point, $u = u^*$, equals the local Alfven sound speed:

$$u^* = \frac{B^*}{\sqrt{\rho^* \mu}} \qquad \textbf{(A4)}$$

Substitution of this into the momentum equation provides the relationship of conditions at the magnetosonic point and the stagnation point (u=0):

$$\frac{B_o^2}{2\mu} = \rho^* u^{*2} + \frac{B^{*2}}{2\mu} \Rightarrow \frac{B_o^2}{2\mu} = \frac{3B^{*2}}{2\mu}$$

$$\text{So,}\quad B^* = \frac{B_o}{\sqrt{3}} \qquad \textbf{(A5)}$$

At the magnetosonic point, the mass density is: follows of (A4)

$$\rho^* = \frac{B^{*2}}{\mu u^{*2}} \qquad \textbf{(A6)}$$

The mass flow per unit area is then:

$$w = \rho^* u^* = \frac{B^{*2}}{\mu u^*} \qquad \textbf{(A7)}$$

The electric field in the steady state, one-dimensional flow is uniform:

$$E = \text{constant} = E^* \qquad \textbf{(A8)}$$

In the limit of high magnetic Reynolds number at the magnetosonic point:

$$E^* = u^* B^* \qquad \textbf{(A9)}$$

The energy equation then becomes:

$$\frac{B^{*2}}{\mu u^*}\left[\frac{u^{*2}}{2}+(h^*-h_o)\right]=\frac{u^* B^*(B_o-B^*)}{\mu} \qquad \textbf{(A10)}$$

where h* is the specific enthalpy at the magnetosonic point. This equation provides the plasma speed in terms of the stagnation value of the magnetic field and the change in specific enthalpy, $Q^* = h^*-h_o$:

$$u^* = \sqrt{\frac{Q^*}{\sqrt{3}-1.5}} = 1.468\sqrt{2Q^*} \qquad \textbf{(A11)}$$

Alfven critical speed, which has a long association with plasma accelerators, is:

$$V_{crit} = \sqrt{2W_i} \qquad \textbf{(A12)}$$

where W_i is the energy per unit mass needed to ionize the flow. Thus, the plasma speed at the magnetosonic point is about 50% higher than Alfven critical speed , if the energy needed for ionization dominates the change in flow enthalpy associated with electrical dissipation. The extent to which this is true depends on many factors within the plasma discharge, including heat transfer and non-thermal distributions.

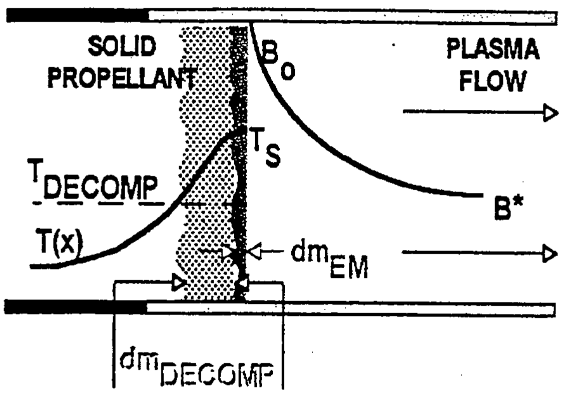

Figure 1. Schematic depicting PPT operation based on the idealized, quasi-steady, one-dimensional model.

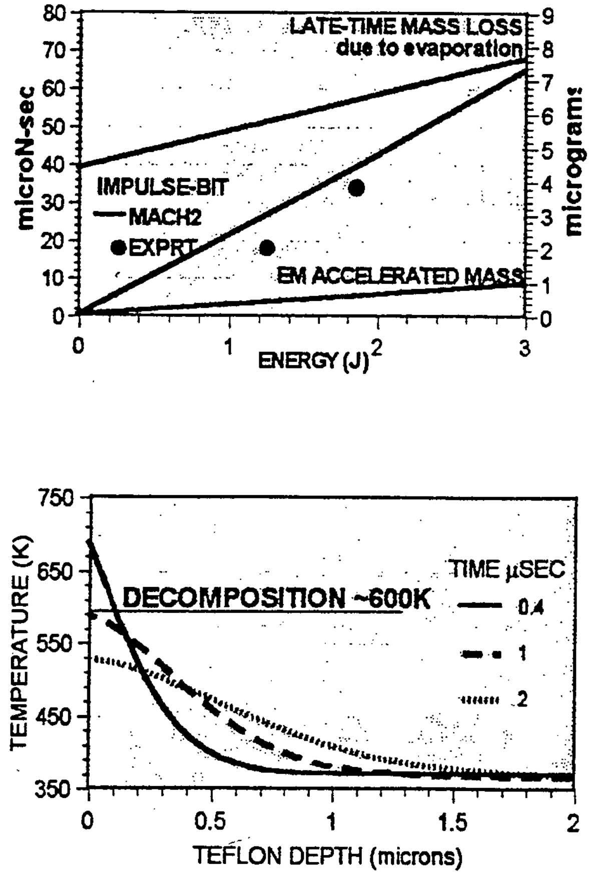

Figure 2. MACH2 simulations of the LES-6 PPT identify and quantify propellant loss mechanisms.

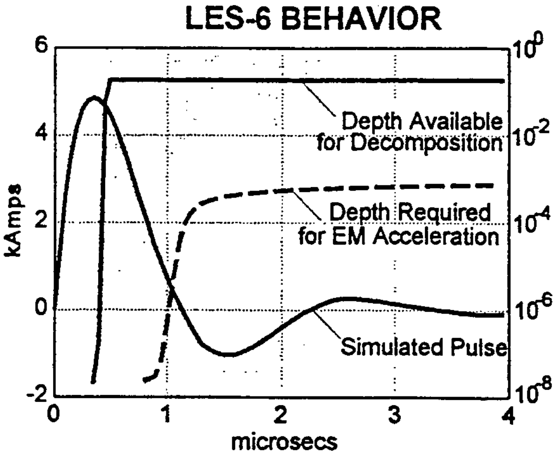

Figure 4. MACH2 calculation of electromagnetic and decomposition depths (based on a decomposition temperature of 600K).

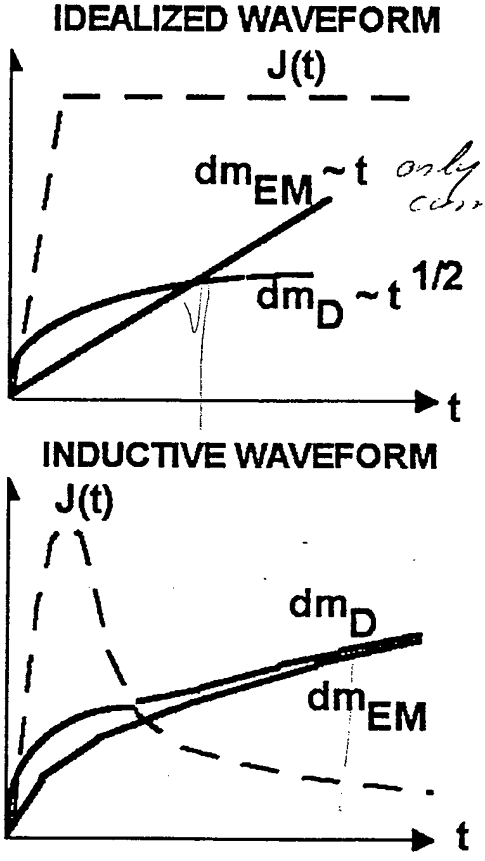

only for const current.

Figure 3. Qualitative evolution of electromagnetically accelerated mass and decomposed mass for idealized and inductive waveforms.

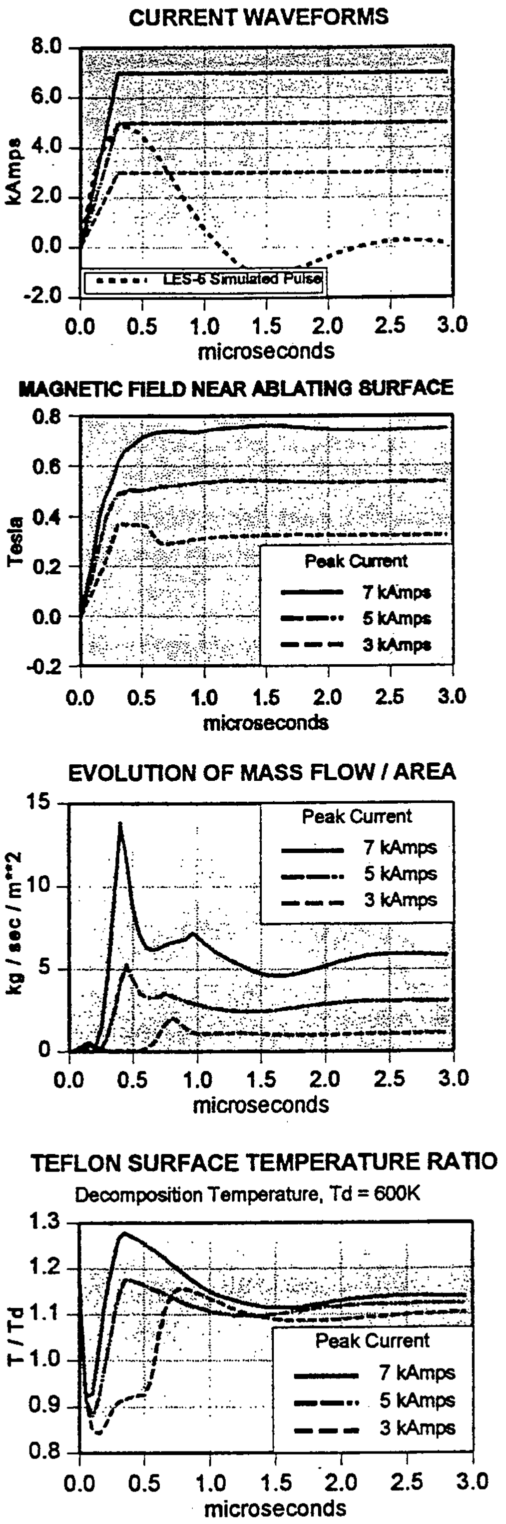
CURRENT WAVEFORMS

MAGNETIC FIELD NEAR ABLATING SURFACE

EVOLUTION OF MASS FLOW / AREA

TEFLON SURFACE TEMPERATURE RATIO

Decomposition Temperature, Td = 600K

Figure 5. MACH2 numerical simulations with idealized current waveforms (top) confirm steady-state operation.

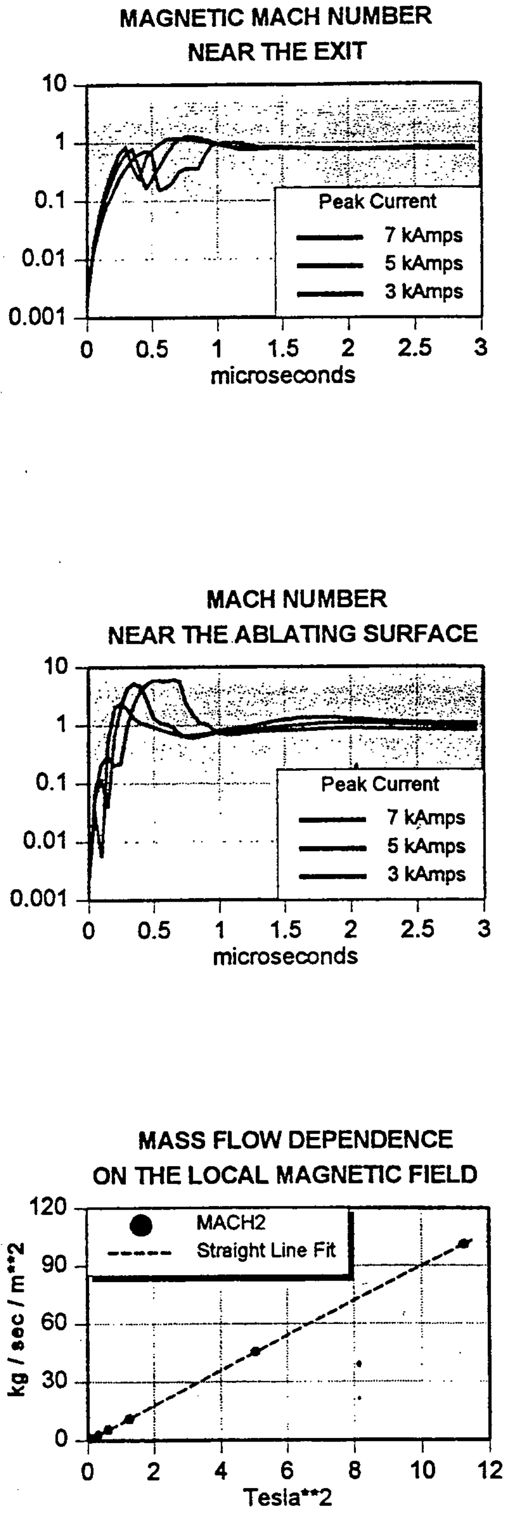
MAGNETIC MACH NUMBER NEAR THE EXIT

MACH NUMBER NEAR THE ABLATING SURFACE

MASS FLOW DEPENDENCE ON THE LOCAL MAGNETIC FIELD

Figure 6. MACH2 evolution of magnetic and thermal Mach numbers to sonic conditions. Scaling of m/A with magnetic field at the propellant's surface.

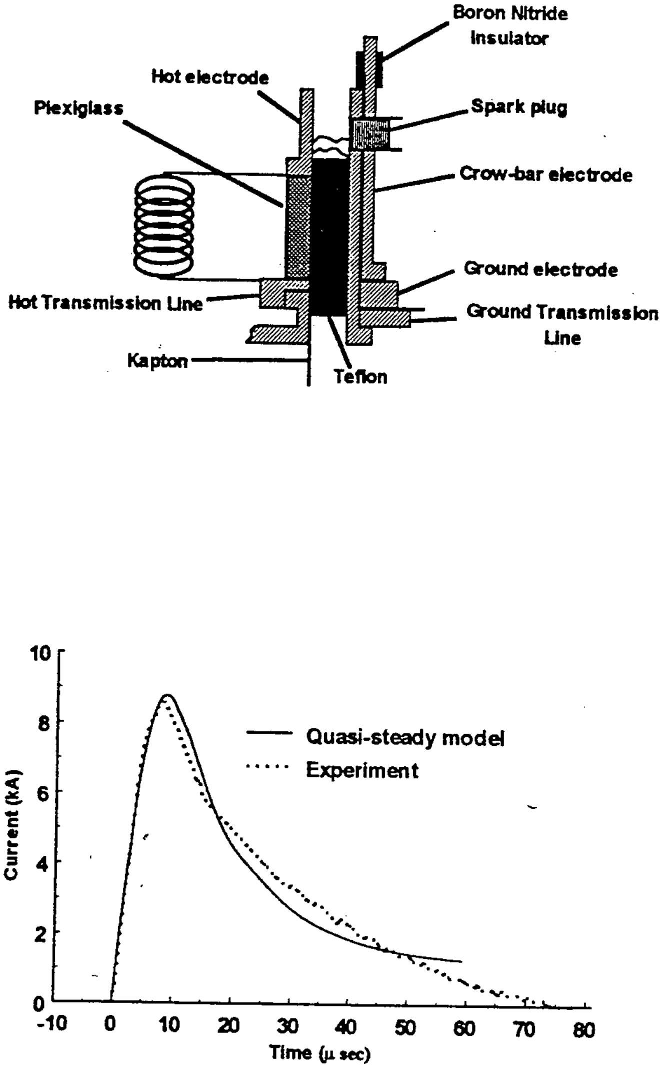

Figure 7. Inductive energy-storage circuit arrangement and resulting current waveform.

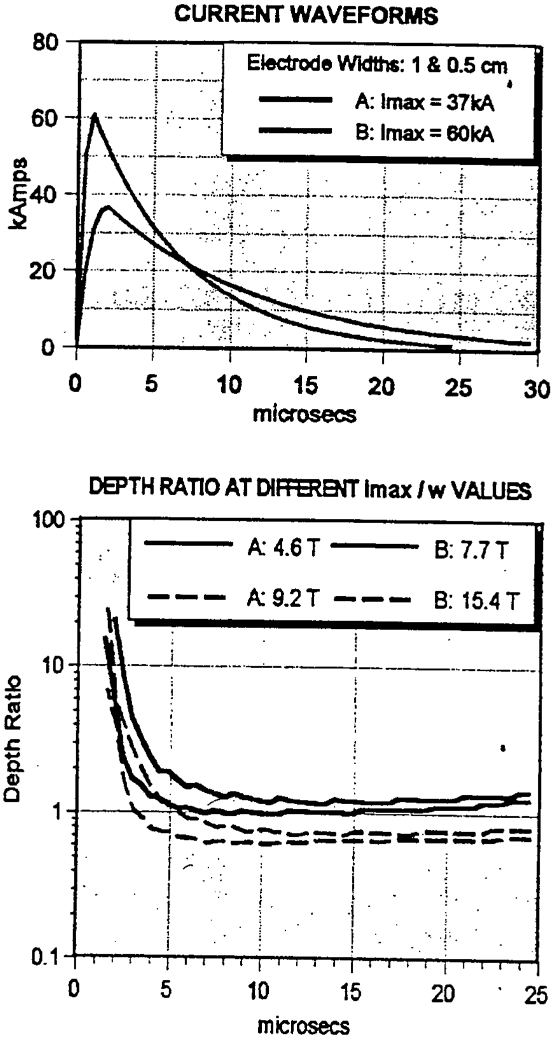

Figure 8. MACH2 input current waveforms (top), and evolution of X_D/X_{EM}.

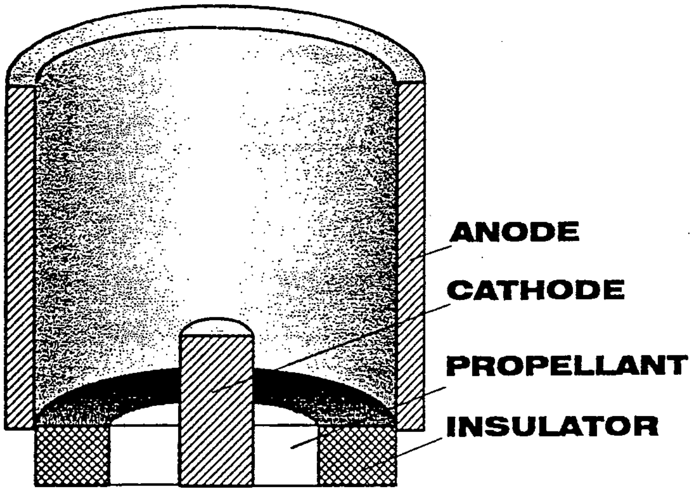

Figure 9. Schematic of the annular PPT configuration used in the MACH2 simulations.

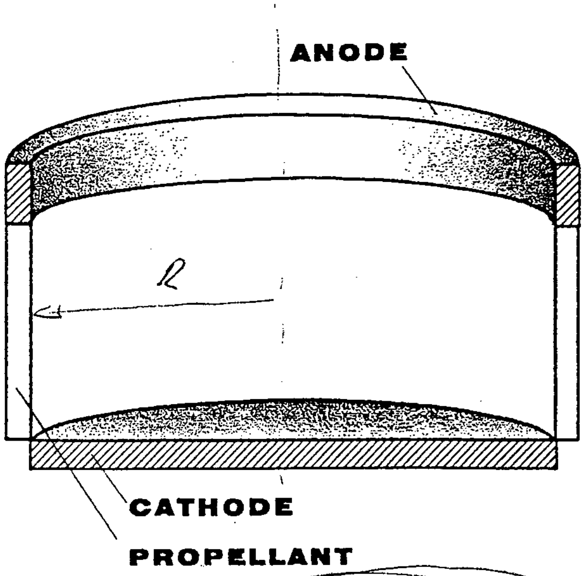

Figure 10. Schematic of the linear pinch PPT configuration used in the MACH2 simulations.

equals melted mass?

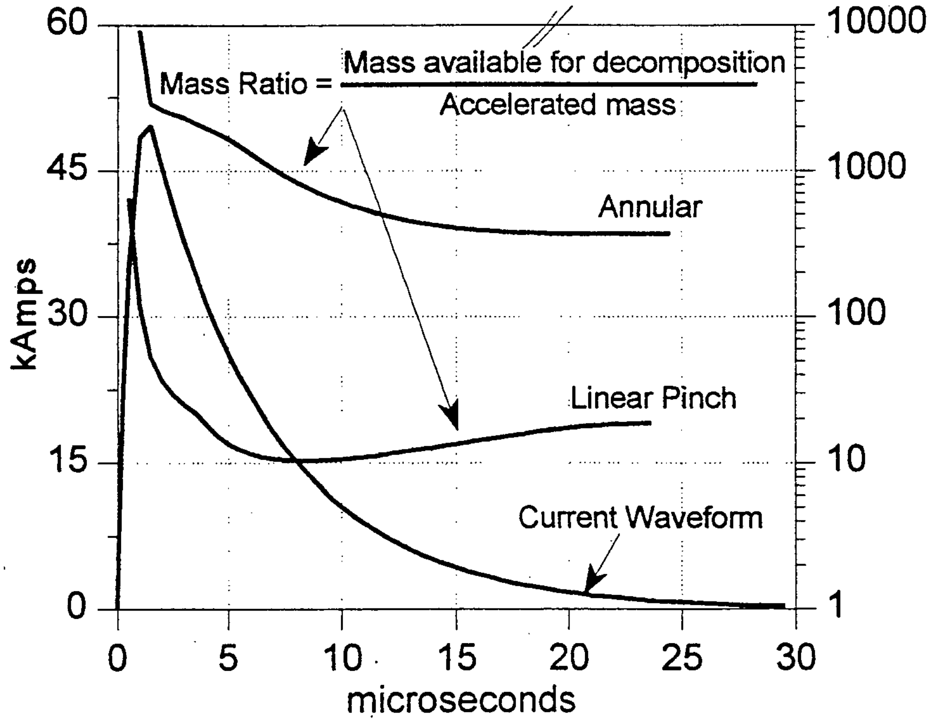

Figure 11. Typical current waveform and mass ratios from the coaxial PPT simulations.

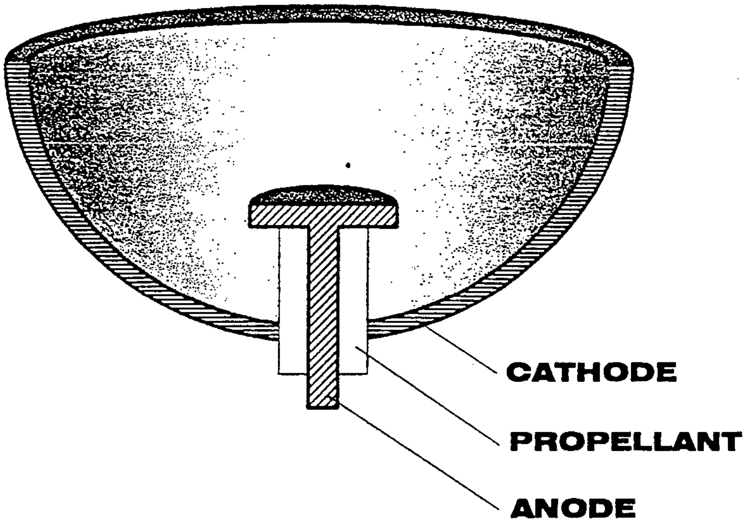

Figure 12. Schematic of the Inverse Pinch configuration used in the MACH2 simulations.

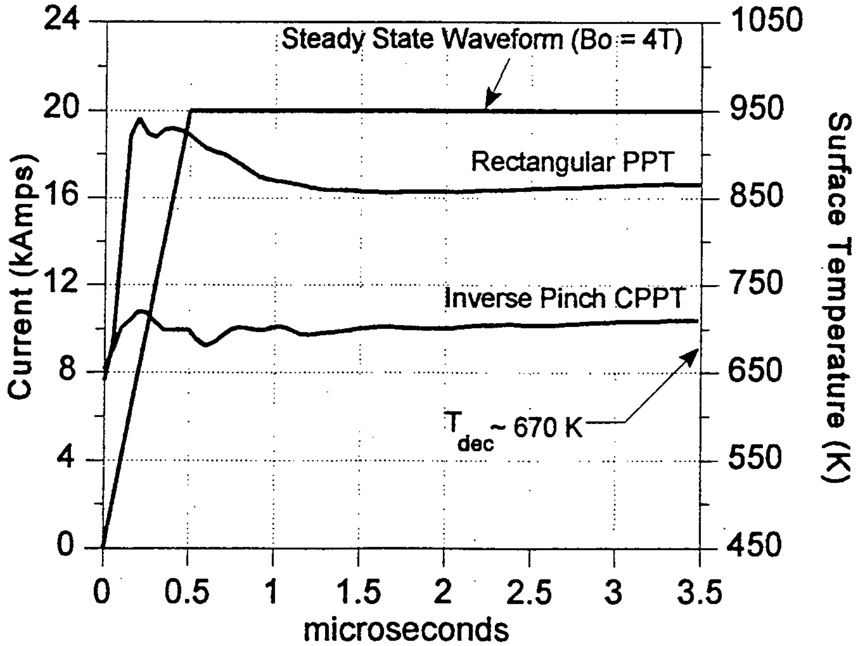

Figure 13 Comparison of the steady state surface temperature between the rectangular and Inverse Pinch PPTs, as determined from the MACH2 simulations.